INFORMATION TO USERS

This manuscript has been reproduced from the microfilm master. UMI films the text directly from the original or copy submitted. Thus, some thesis and dissertation copies are in typewriter face, while others may be from any type of computer printer.

The quality of this reproduction is dependent upon the quality of the copy submitted. Broken or indistinct print, colored or poor quality illustrations and photographs, print bleedthrough, substandard margins, and improper alignment can adversely affect reproduction.

In the unlikely event that the author did not send UMI a complete manuscript and there are missing pages, these will be noted. Also, if unauthorized copyright material had to be removed, a note will indicate the deletion.

Oversize materials (e.g., maps, drawings, charts) are reproduced by sectioning the original, beginning at the upper left-hand corner and continuing from left to right in equal sections with small overlaps.

ProQuest Information and Learning
300 North Zeeb Road, Ann Arbor, MI 48106-1346 USA
800-521-0600

Characteristics of $CuInSe_2$ Homojunction Photodetectors

by

Feng LI

A thesis submitted to the Faculty of Graduate Studies and Research
in partial fulfillment of the requirements for the degree of
Master of Engineering

Department of Electrical Engineering
McGill University
Montreal, Canada

January, 2001

Abstract

Studies have been made on homojunction photodetectors fabricated on Bridgman-grown monocrystalline p-type $CuInSe_2$ substrates by diffusion of indium. The essential steps required to optimize the fabrication conditions were established.

Firstly, parameters such as quantum efficiency, junction depth, surface recombination velocity, and minority carrier diffusion length are analyzed. Secondly, the dark current-voltage characteristics of devices were measured. Some detector dark current is only 80nA at 0.5V reverse bias. It was confirmed that the diffusion current and recombination current are comparable in the dark current transport mechanism of the $CuInSe_2$ homojunctions. Thirdly, the relationships between capacitance-voltage, capacitance-frequency characteristics were also investigated. It was observed that at a given voltage, the capacitance value decreased when the measuring frequency was increased. This result confirmed that deep defects exist in the material. Fourthly, the diffusion length of minority carriers was determined by the photocurrent and capacitance method. The diffusion length is smaller than 1 micron. The quantum efficiency and photoresponse were also measured. The maximum quantum efficiency of the detectors was measured as high as 60%. The photodetector response time range from 14 μs to 21 μs.

Résumé

Des études ont été effectuées sur des détecteurs photoélectriques d'homojonction fabriqués sur les substrats monocristallins Bridgman-croissants du p-type $CuInSe_2$ par diffusion de l'indium. Les étapes essentielles exigées pour optimaliser les conditions de fabrication ont été établies.

Premièrement, des paramètres tels que l'efficacité de tranche de temps, la profondeur de jonction, la vitesse de recombinaison extérieure, et la longueur de diffusion de porteur de minorité sont analysés. Deuxièmement, les caractéristiques courant-tension foncées des dispositifs ont été mesurées. Un certain courant foncé de détecteur est seulement 80nA 0.5V à la polarisation d'inversion. On a confirmé que le courant de diffusion et le courant de recombinaison sont comparables pour le mécanisme de transport de courant foncé $CuInSe_2$ des homojonctions. Troisièmement, les rapports entre la capacité-tension, caractéristiques de capacité-fréquence ont été également étudiés. On a observé qu'à une tension donnée, la valeur de capacité diminuée quand la fréquence de mesure a été augmentée. Ce résultat a confirmé que des défauts profonds existent dans le matériel. Quatrièmement, la longueur de diffusion des porteurs de minorité a été déterminée par la méthode de photocurant et de capacité. La longueur de diffusion est plus petite que 1 micron. L'efficacité et le photoreponse de tranche de temps ont été aussi mesurés. L'efficacité maximum de tranche de temps des détecteurs a été mesurée aussi haut que 60%. L'intervalle de temps de réponse de détecteur photoélectrique de 14 μs à 21 μs.

Acknowledgements

I would like to express my gratitude to my supervisor, Professor I. Shih for his enlightening technical guidance during this study. His continuous criticism and supervision introduces me to the field of photodetector research. He influences me not only by his knowledge but also gentle personality.

I would like to acknowledge all members in the Electronic Devices and Materials group at McGill for their assistance and discussions. Special thanks are also due to Mr. F. Gan, Mrs. H. Wang for their technical assistance and Mrs. Janet Maniate-Morley for translating the abstract into French. Thanks are also due to the staff in the electrical and mechanical workshops in the department for their technical assistance.

Most importantly, I would like to express my special thanks to my parents and family for their unwavering support and love throughout my studies.

Table of Contents

Chapter 1

Introduction

1.1 Motivation

Photodetectors play an important role in optical-fiber communication systems operated in the near-infrared region (0.8 to 1.6 μm). Photodetectors are semiconductor devices that can detect optical signals through the absorption of photons, which changes the electronic properties of the devices. The absorption of photons can lead to the generation of a photocurrent in a photoconductor or a photovoltage in a photovoltaic detector. Copper indium diselenium ($CuInSe_2$) is a direct band-gap ternary semiconductor with a chalcopyrite structure. It is useful for several potential applications such as light-emitting diodes [1.1] and photovoltaic solar cells [1.2-6].

Extensive studies have been made on this material both from the fundamental as well as applications points of view. In the visible range, $CuInSe_2$ has extremely high optical absorption coefficients with the value of about 4×10^5 cm^{-1} [1.7], so that most of the incident light is absorbed within a micrometer or so of the surface. Thus, the amount of material required to fabricate $CuInSe_2$-based cells is small. Junction devices based on $CuInSe_2$ have good stability [1.8]. No evidence for long- or short-term device degradation is observed [1.9] in these devices as has been found in amorphous silicon (α-Si) counterparts [1.10]. In addition, the wavelength of 1.2 μm corresponds to the direct band gap of 1.01 eV [1.11] and is within a spectral region under intense investigation. Ternary chalcopyrite materials have shown considerable technological promise in a variety of optoelectronic device applications, ranging from visible to infrared photodetectors.

$CuInSe_2$ has the chalcopyrite crystal structure as shown in Figure 1.1. The chalcopyrite structure can be viewed as two interpenetrating fcc sub-lattices with an ordered array of I-III atomic positions (cations) on one sub-lattice and the group VI atoms (anions) on the other. Both n-type and p-type crystals can be prepared from melts with stoichiometric starting proportions of the elements. In general, the material crystallizes into n-type semiconductor. With a sufficient excess of selenium or copper, the ingot is p-

type and with an excess of indium the ingot is n-type. Doping can also change the conductivity type of $CuInSe_2$. When a large amount of indium is evaporated onto p-type crystals and annealed, an n^+ layer will result.

Unlike heterojunctions, a homojunction has no lattice matching problem and the interfacial states is minimum. Thus, the leakage current is small. The other advantage of homojunctions is that the fabrication process is simple compared to that of heterojunctions.

Pertinent physical and electrical data on the ternary $CuInSe_2$ are summarized in Table 1.

Table 1. Properties of $CuInSe_2$ material at room temperature.

Material	Eg (eV)	Transition	Dielectric constant	Lattice constants (Å)		Electron affinity (eV)
				a	c	
$CuInSe_2$	1.01-1.04	Direct	10	5.782	11.62	4.58

1.2 Literature survey

The use of $CuInSe_2$ compound semiconductor for tandem solar cell applications has been reported recent by C. H. Champness [1.12]. Both p-type and n-type conducting $CuInSe_2$ single crystals can be grown by a suitable choice of growth conditions.

For PV applications, solar cells of $CuInSe_2$ are based on a heterojunction structure with CdS, CdZnS, or ZnO as window layers. In 1975 a monocrystalline cell in the form $CuInSe_2$ (p)/CdS (n) with an energy conversion efficiency of 12% has been fabricated by Shay et al [1.13]. The lattice mismatch between $CuInSe_2$ and CdS (or (Cd(Zn)S) was found to be small, minimizing interfacial states [1.14]. Epitaxial $CuInSe_2$ films were also reported by Grindle et al. [1.15].

Polycrystalline $CuInSe_2$ -based thin film photovoltaic cells with a conversion efficiency over 14% have been successfully fabricated recently [1.16]. These thin film cells have good stability. Because of these characteristics, $CuInSe_2$ has been considered as one of the most promising candidates for terrestrial solar cell application. Solar cells of $Cu(In,Ga)Se_2$ have achieved the highest efficiencies on the laboratory scale as well as on

the level of large-area modules among the polycrystalline devices. Several technologies for fabrication of high efficiencies $CuInSe_2$ solar cells (>16%) have been realized by different groups [1.17-18], some have achieved a certain degree of maturity. Commercial production of $Cu(In,Ga)Se_2$-based cells is on its way at several places [1.19-20]. Furthermore, $Cu(In,Ga)Se_2$ thin-film modules show excellent outdoor stability [1.8] and radiation hardness [1.21-22].

Apart from $CuInSe_2$ heterojunctions, homojunctions of $CuInSe_2$ were also reported by several workers [1.23-25]. Yu et al. [1.23] reported the formation of a $CuInSe_2$ p-n homojunction by diffusion of cadmium into p-type $CuInSe_2$. The $CuInSe_2$ single crystals used were prepared by a melt-grown method. P-type single crystals with flat as-grown (112) surfaces were chosen for substrates. The substrates were etched with a hot solution of $HCl:HNO_3$ (1:1) before the Cd diffusion. The diffusion was carried out with the substrate placed at one end of an evacuated quartz ampoule and with Cd metal shots placed at the other end. The quartz ampoule was then heated at 400 °C for 6-8 minutes. The substrate was then made into a mesa structure by etching the substrate in a hot solution of $HCl:HNO_3$ (1:1) with the n layer protected by wax. Au was sputtered onto the p side and In-Sn to the n sides to form ohmic contacts with the $CuInSe_2$. A quantum efficiency of 35-40 % in the wavelength region 0.9-1.2 μm was observed in these cells. Yu et al also reported the formation of $CuInSe_2$ junctions by ion implantation [1.24]. A quantum efficiency of 60-70 % in the wavelength region 0.7-1.1 μm was reported.

Tell et al. [1.25] reported the formation p-n homojunctions by annealing Zn-, Cd- and Cu-plated p-type $CuInSe_2$ samples at temperatures from 200-450 °C. A zone-melting technique was used to grow their $CuInSe_2$ single crystals. Some of the as-frown slices were annealed in saturated Se vapor before the junction formation. This procedure resulted in junctions with uniform depth after diffusion. P-type slices up to 1 mm thick were etched in $HCl:HNO_3$ (1:1) solution. Junctions were formed by plating the etched surfaces with Zn or Cd from cyanide solutions or Cu from a Cu_2SO_4+HNO_3 solution and then by annealing and quenching to room temperatures in evacuated quartz ampoules. Junctions were formed with various combinations of annealing times and temperatures. The ohmic contact to the p-$CuInSe_2$ was provided by plating Au; while for the n diffusion

region, it was provided using Zn, Cd, or Cu. A maximum quantum efficiency of less than 48 % at the wavelength 1.1 μm was reported.

1.3 Previous work on monocrystalline $CuInSe_2$ carried out at McGill

In our laboratory, extensive efforts have been made to obtain good quality single crystals in order to study their properties. The samples used in the present work were obtained from ingots grown by Mr. Vahid Shahidi and Dr. Lap Sum Yip (McGill University, Montreal, Canada) using the horizontal Bridgman method.

The $CuInSe_2$ single crystals were prepared from the element materials of Cu (6 9's), In (5 9's), and Se (5 9's) in a high purity pellet form. The Cu pellets were etched with diluted HNO_3 and In with diluted HCl to remove thin oxide layers on the surfaces. These were then rinsed with DI water followed by alcohol. The Se pellets were used either as-received or rinsed with water and alcohol. After this cleaning process, the ampoule which was specially shaped and has been cleaned was quickly charged with the starting materials weighted in stoichiometric proportions. The ampoule was evacuated to a pressure of about 10^{-5} to 10^{-6} torr and sealed. The ampoule was then connected to a quartz rod, which, in turn, was fixed onto a horizontal pulling mechanism for the growth experiment. A schematic diagram of the experimental set-up is shown in figure 1.2. The temperature was initially raised slowly, at a rate of about 20 °C/hr, to allow the exothermic heat of reaction between the elements to dissipate. Following this reaction stage the temperature was raised to 1100 °C and the melt was mixed by rotating the ampoule for several hours. The ampoule was then slowly moved at 1-10 mm/hr through a stable temperature gradient, 10 °C/cm, from temperatures above melting point of $CuInSe_2$ (986 °C) to below the melting point to allow the melt to freeze from one end into a solid form. When the entire ampoule was below 700 °C, it was cooled to room temperature at a rate of 50 °C/hr. Using this procedure, ingots containing large p-type $CuInSe_2$ grains from several millimeters to up 2 centimeters a side were routinely obtained.

In addition to the growth of single crystal $CuInSe_2$, much work has been done on the monocrystalline $CuInSe_2$ in our lab. C. L. Chan studied the Al/p-$CuInSe_2$ tunnel MIS Schottky diodes and surface properties (1989). Dr. L. S. Yip studied the Al-Y_2O_3-$CuInSe_2$ structures (1989). Dr. A. L. Li investigated the deep energy levels in

monocrystalline $CuInSe_2$ (1991). L. Li measured the electron diffusion length in $CdS/CuInSe_2$ solar cells (1993). Dr. C. X. Qiu characterized the $ZnO/CuInSe_2$ heterojunctions and $CuInSe_2$ homojunctions (1985). Most of the above work was on heterojunction devices of $CuInSe_2$. Dr. C. X. Qiu also studied homojunctions in indium-diffused $CuInSe_2$ single crystals (1985). However, the junction depth in her devices was large, and the devices were not suitable for photodetectors applications.

1.4 Thesis contribution and outline

The chalcopyrite $CuInSe_2$ semiconductor with a direct band gap, E_g = 1.0 eV, at room temperature appears to be well suited for optoelectronic devices [1.26] and photovoltaic solar cells [1.27]. In recent years, many papers devoted to the investigation of the p-n homo- and hetero-junctions made with $CuInSe_2$ have been published [1.27-28]. However, little work has been reported on the studies of the $CuInSe_2$ homojunction photodetectors. The main reason for this is the difficulty in getting $CuInSe_2$ single crystals with uniform composition and good quality sallow p-n junctions. The purpose of this work is to study the properties of $CuInSe_2$ p-n homojunction as a photodetectors.

Although quantum efficiencies of $CuInSe_2$ homojunctions have been reported previously, very limited information was given on the bandwidth of the $CuInSe_2$ homojunctions [1.29]. In this work, $CuInSe_2$ homojunctions have been fabricated on monocrystalline substrates and the results obtained are reported.

The remainder of the thesis is organized as follows:

Chapter 2 describes the theory of homojunction photodiode and device fabrication processes. It includes a brief description of photovoltaic effect, photocurrent-voltage characteristics of p-n junctions, quantum efficiency, and the photodiode response time. In the last part of this chapter, sample preparation and device fabrication procedures are discussed in detail. Dark current-voltage characteristics of the devices are described in chapter 3. In chapter 4, results on capacitance-voltage characteristics are presented. Chapter 5 describes the results from minority carrier diffusion length measurements. In chapter 6, measurement results of the quantum efficiency and bandwidth of the photodiodes are presented. Chapter 7 concludes this work and points out possible further work.

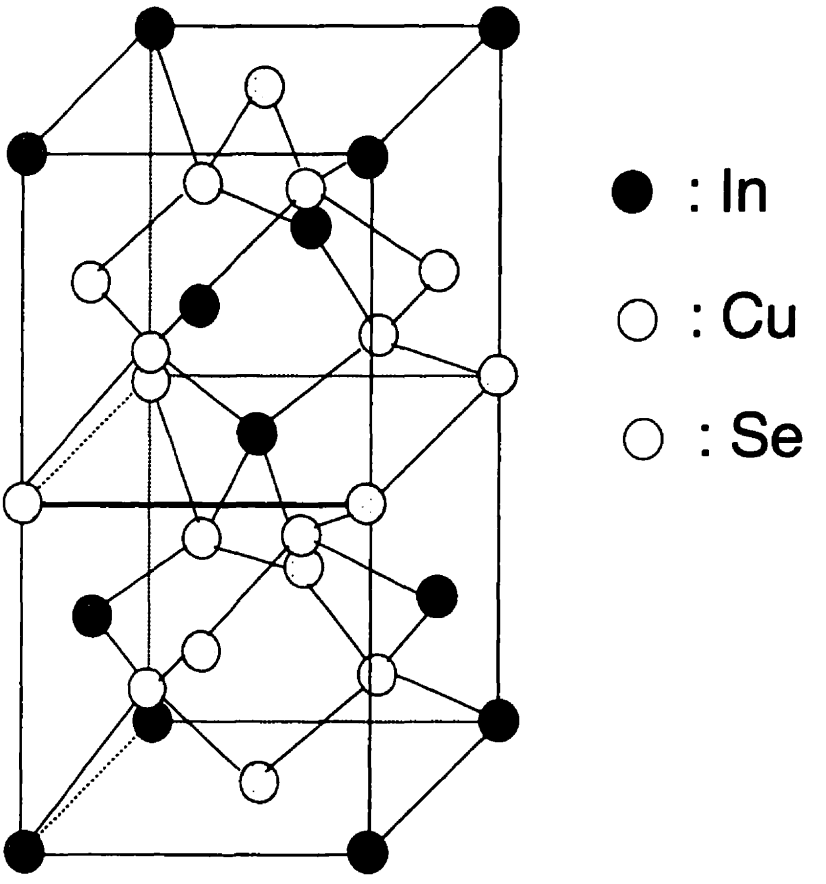

Figure 1.1 The chalcopyrite crystal structure of $CuInSe_2$.

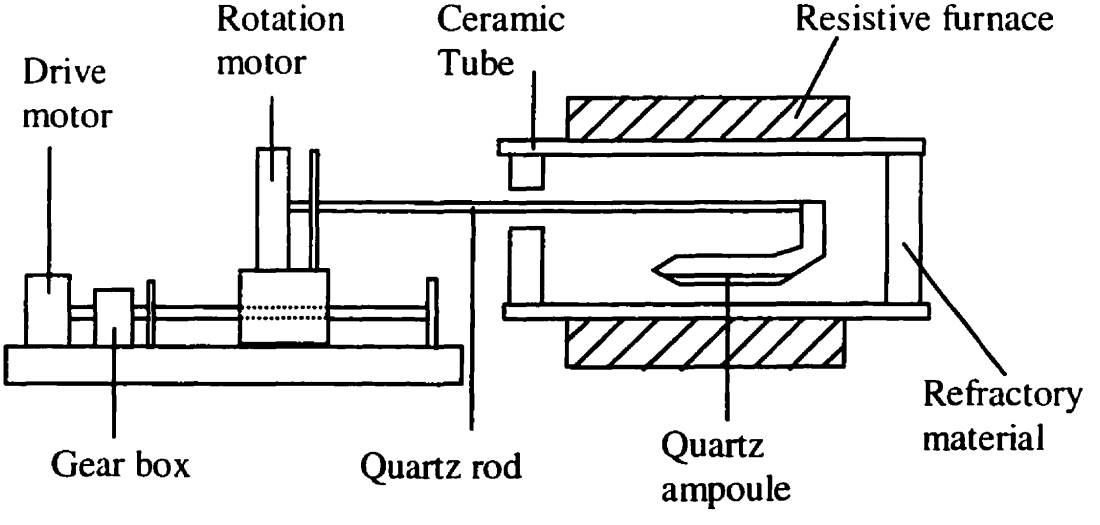

Figure 1.2 A schematic drawing of the crystal growth system.

Chapter 2

Theory and Device Fabrication

Photodetectors are used in equipment ranging from optical fiber communication systems to consumer electronics. The operation of photodetectors is based on the absorption of photons, which changes the electric properties of the electronic system. It includes the generation of a photocurrent in a photoconductor or a photovoltage in a photovoltaic detector. The performance of a photodetector depends on the optical absorption process, the carrier transport, and the interaction with external circuits.

In this chapter, my focus is on the understanding of the physical processes of the carrier generation and transport. The relationships between the optical power and the photocurrent, junction depth and quantum efficiency were derived. Finally, the concept of noise in a photodetector is also discussed.

2.1 Theory of a p-n homojunction photodiode

2.1.1 Photovoltaic effect

In this section a brief review of the photovoltaic effect in semiconductor homojunctions was given. Major processes and mechanisms that control junction currents are also described.

The photovoltaic effect involves the interaction of light with solid state materials. First, we consider optical absorption process in a semiconductor. There are several optical absorption processes: fundamental absorption, free carrier absorption, and impurity level absorption, et al. The amount of optical power absorption is expressed by by Lambert's law [2.1],

$$I = I_0 \exp(-\alpha_{ab} x) \quad (2.1)$$

where I is the light intensity, I_0 is the intensity of the incident beam, x indicates the distance, and α_{ab} is the absorption coefficient (in cm^{-1}). This coefficient varies with the light wavelength. The inverse of the absorption coefficient is called the absorption length

(or the penetration depth). At the absorption length, the light intensity has decreased to $1/e$ of the intensity of the incident light [substituting $x = 1/\alpha_{ab}$ in Eq. (2.1)].

Among the optical absorption processes, the fundamental absorption corresponding to the excitation of electrons from the valence band to the conduction band is dominant. Consequently, when the semiconductor is illuminated, light having an energy greater than the band-gap of the semiconductor is absorbed and that having an energy less than the band-gap will be allowed to pass through the semiconductor without being absorbed. At energies near the absorption edge, the absorption coefficient is expressed as: [2.2]

$$\alpha_{CV} \propto (h\nu - E_g)^{1/2} \quad (2.2)$$

for direct transition, and

$$\alpha_{CVin} \propto (h\nu - E_g \pm E_{phonon})^{1/2} \quad (2.3)$$

for indirect transition. Here $h\nu$ is the energy of the incident photons, E_{phonon} is the phonon energy related to the indirect transition and E_g is the band-gap energy. As seen from Eqs. (2.2) and (2.3), the absorption coefficient near the absorption edge increases more rapidly in direct band-gap semiconductors than in indirect band-gap semiconductors. At the absorption edge, the absorption coefficient is small because the density of states in the conduction band is low. As the photon energy increases, electrons can be excited to a higher energy level in the conduction band, at which the density of states is larger. Thus, the absorption coefficient increases exponentially with the increase of energy and tends to saturate. The transition probability in the optical excitation processes is higher in direct band-gap semiconductors than in indirect ones because indirect transition is impossible without a change in the momentum. In an indirect semiconductor, the transition can be accomplished by means of phonon emission or absorption. Figure 2.1 shows the variation of absorption coefficients of several semiconductor materials with photon energy [2.3]. Both $CuInSe_2$ and CdTe are direct band-gap materials, with abrupt transition of absorption coefficients. On the other hand, monocrystalline Si is an indirect band-gap material with a gradual variation of absorption coefficient.

Absorption due to impurity levels also occurs in semiconductors. This includes conduction band to acceptor level, donor level to valence band, and impurity level to impurity level transitions. In additions, absorption due to free carriers may occur.

The total absorption coefficient is the sum of the coefficient components arising from the above-described different absorption processes:

$$\alpha_{ab} = \alpha_{CV} + \alpha_{il} + \alpha_{fc} \quad (2.4)$$

where α_{CV}, α_{il}, and α_{fc} are respectively the coefficients of absorption related to valence band to conduction band absorption, impurity level absorption, free carrier absorption.

The photovoltaic effect in semiconductors requires the presence of an internal junction electric field. Hence, it is most often associated with junctions in the semiconductor materials, which act to separate carriers generated by absorption of light. The separation of charges converts the optical power into electric power. When light is incident on a p-n junction, the photo-generated electrons and the holes are separated by the electrical field at the p-n junction, without any external electric bias, to generate an electromotive force between the p- and n-sides. In term of the photovoltaic effect, there is no basic difference between a p-n homojunction and a p-n heterojunction.

As stated before, a homojunction is a junction formed between two portions of the same semiconductor material. An energy band diagram of homojunction is given in Figure 2.2, where the vacuum level has been included for reference. The electron affinity, χ_s, and the band gap, E_G, are the same on both sides of the junction. The diffusion voltage, V_D, also called the built-in voltage, is resulted from the transfer of charges between n- and p-type portions in order to maintain constant Fermi level across the junction. The diffusion voltage is thus given by the difference between the Fermi energies in the n- and p-type portions far from the junction.

Electron-hole pairs in photodiodes or photovoltaic devices produced by the incident light are driven to drift separated in opposite directions at the p-n junction to result in a photocurrent, which is an electrical output.

2.1.2 Quantum efficiency

To realize the optimum performance of a device, we must take into account the actual transport mechanisms of carriers at the junction, the presence of surface

recombination, the effect of drift fields and the contribution to the current from regions with different properties. The quantum efficiency, η_{ph}, is one of the important parameters for a photodetector. We describe factors which affect the quantum efficiency of a photodiode. For simplicity, we will consider the case of a one-dimensional abrupt junction using classical approximations but not to compute the exact quantum efficiency for a particular structure.

The quantum efficiency, η_{ph}, of a photodiode is defined as:

$$\eta_{ph} = \frac{number\ \ of\ \ electron-hole\ \ pairs\ \ contributing\ \ to\ \ photo-induced\ \ current}{number\ \ of\ \ incident\ \ photons}$$

so

$$\eta_{ph} = \frac{J_{ph}/q}{P_{inc}/hv} \qquad (2.5)$$

where the I_{ph} and the P_{inc} are the photo-induced current and the incident optical power. [2.4]

The one-dimensional photodiode model is shown in Figure 2.3 for with an abrupt junction where the space charge of width w around the metallographic junction boundary at $x = t$. Hence, the two quasineutral regions (0, x_n) and (x_n+w, t+d) are homogeneously doped. The photocurrent comprises the drift current originated from the photo-induced carriers within the depletion region and the diffusion current due to the minority carriers generated within their diffusion lengths from the edge of the depletion region. When light of wavelength λ is incident on the surface of a semiconductor, the generation rate of electron-hole pairs as a function of distance x from the surface is [2.5]

$$G(\lambda) = \alpha(\lambda)\phi(\lambda)[1 - R(\lambda)]\exp[-\alpha(\lambda)x] \qquad (2.6)$$

where λ is the wavelength of the incident light, $\phi(\lambda)$ is the number of incident photons per square centimeter per second per unit bandwidth, and R is the number of photons reflected from the surface. The photocurrent produced by these carriers and the spectral response can be determined for low-injection levels by using the minority carrier continuity equations and appropriate boundary conditions.

The minority carrier continuity equations are

$$\frac{1}{q}\frac{dJ_p}{dx} - G_p + \frac{p_n - p_{n0}}{\tau_p} = 0 \qquad (2.7)$$

for holes in the n-type materials, and

$$\frac{1}{q}\frac{dJ_n}{dx} - G_n + \frac{n_p - n_{p0}}{\tau_n} = 0 \qquad (2.8)$$

for electrons in the p-type materials. The hole and electron currents are

$$J_p = q\mu_p p_n E - qD_p \frac{dp_n}{dx} \qquad (2.9)$$

$$J_n = q\mu_n n_p E + qD_n \frac{dn_p}{dx} \qquad (2.10)$$

respectively, where E is the electric field, p_n and n_p are the photogenerated minority carrier densities, p_{n0} and n_{p0} are the minority carrier densities in equilibrium in the dark. L_n and L_h are the electron and hole diffusion length, respectively; D_n and D_h are the electron and hole diffusion coefficient, respectively.

In our one dimensional model, the two sides of the junction are uniformly doped, so that no electric fields exist outside the depletion region. For the hole equations (2.6) and (2.8), there are two boundary conditions; at the surface where recombination occurs:

$$D_p \frac{d(p_n - p_{n0})}{dx} = S_p(p_n - p_{n0}) \qquad \text{at } x = 0$$

$$p_n - p_{n0} = 0 \qquad \text{at } x = x_n .$$

Considering a uniformly doped p-n junction, the hole photocurrent density per unit bandwidth collected at the junction edge $(x = x_n)$ from the top layer for a given wavelength is

$$J_p = \left[\frac{q\phi(1-R)\alpha L_p}{\alpha^2 L_p^2 - 1}\right] \times \left[\frac{\left[(S_p L_p / D_p) + \alpha L_p\right] - \exp(-\alpha x_n)\left[(S_p L_p / D_p)\cosh(x_n / L_p) + \sinh(x_n / L_p)\right]}{(S_p L_p / D_p)\sinh(x_n / L_p) + \cosh(x_n / L_p)} - \alpha L_p \exp(-\alpha x_n)\right] \qquad (2.11)$$

It should be noted that the effect of surface recombination has been included in the above expression through the surface recombination velocity term S_p.

The boundary conditions for the electron current are

$$n_p - n_{p0} = 0 \qquad \text{at } x = x_n + W$$

$$D_n \frac{d(n_p - n_{p0})}{dx} = -S_n(n_p - n_{p0}) \qquad \text{at } x = t + d$$

The electron photocurrent density at the junction edge from the base layer of the cell is

$$J_n = \frac{q\phi(1-R)\alpha L_n}{\alpha^2 L_n^2 - 1}\exp[-\alpha(x_n + W)]$$
$$\times\left\{\alpha L_n - \frac{(S_n L_n / D_n)[\cosh[(t+d-x_n-W)/L_n] - \exp[-\alpha(t+d-x_n-W)]}{(S_n L_n / D_n)\sinh[(t+d-x_n-W)/L_n] + \cosh[(t+d-x_n-W)/L_n]}\right. \qquad (2.12)$$
$$\left. + \frac{\sinh[(t+d-x_n-W)/L_n] + \alpha L_n \exp[-\alpha(t+d-x_n-W)]}{(S_n L_n / D_n)\sinh[(t+d-x_n-W)/L_n] + \cosh[(t+d-x_n-W)/L_n]}\right\}$$

where S_n is the surface recombination velocity on the back side of the photodetector. The photocurrent collected from the depletion region is given by

$$J_{dr} = q\phi(1-R)\exp(-\alpha x_n)[1 - \exp(-\alpha W)] \qquad (2.13)$$

It is assumed that the electric field in the depletion region is high enough so that the photogenerated carriers are accelerated out of the region before recombination occurs. The total short-circuit photocurrent density at a wavelength λ is then

$$J = J_n + J_p + J_{dr} \qquad (2.14)$$

Next, the conditions under which the maximum quantum efficiency is achieved in homojunction photodiodes and the corresponding junction depth are determined.

Three regions contribute to the photodiode quantum efficiency: two neutral regions of different conduction types and the space charge region. Substituting Eq. (2.5) into Eqs. (2.11), (2.12), and (2.13), thus:

$$\eta = \eta_n + \eta_{DR} + \eta_p \qquad (2.15)$$

$$\eta_n = \frac{(1-R)\alpha L_h}{\alpha^2 L_h^2 - 1}\left\{\frac{\alpha L_h + \gamma_1 - \exp(-\alpha x_n)[\gamma_1 ch(x_n / L_h) + sh(x_n / L_h)]}{\gamma_1 sh(x_n / L_h) + ch(x_n / L_h)} - \alpha L_h \exp(-\alpha x_n)\right\}$$

(2.16)

$$\eta_p = \frac{(1-R)\alpha L_h \exp[-\alpha(x_n + w)]}{\alpha^2 L_h^2 - 1}$$

$$\left\{ \frac{(\gamma_2 - \alpha L_e)e^{-\alpha(t+d-x_n-w)} - sh\dfrac{t+d-x_n-w}{L_e} - \gamma_2 ch\dfrac{t+d-x_n-w}{L_e}}{\gamma_2 sh[(t+d-x_n-w)/L_h] + ch[(t+d-x_n-w)/L_h]} + \alpha L_e \right\} \quad (2.17)$$

$$\eta_{DR} = (1-R)\{\exp(-\alpha x_n) - \exp[-\alpha(x_n + w)]\} \quad (2.18)$$

where $\gamma_1 = S_h L_h / D_h$, $\gamma_2 = S_n L_n / D_n$.

In the following, we shall consider the internal quantum efficiency neglecting the losses due to reflection of the radiation from the illuminated photodiode surface.

To obtain a high photodiode quantum efficiency, it is required to have a thin illuminated region so that the generated carriers may reach the junction potential barrier by diffusion. We shall estimate the junction depth vs. quantum efficiency. Let us consider two cases: (1) the surface recombination velocity is zero (s_1=0) and (2) the surface recombination velocity is high (s_1 = 10 m/sec), and (s_1 = 100 m/sec). The calculation will be based on equations (2.15) to (2.18) for a typical absorption coefficient of 2×10^6 m^{-1}. Let us further assume the doping of both sides of the junction to be equal, μ = 30 cm^2/V-sec, and the diffusion length $L_n = L_h$ = 1 μm. The width of the abrupt junction depletion width is assumed to be w = 0.5 μm.

In Figure 2.4, the variation of quantum efficiency of the $CuInSe_2$ photodiode with the normalized thickness of the illuminated junction region t/L_h of the p-type region is given. From Figure 2.4 we can see that the total quantum efficiency attains its maximum at $t \approx 0.3\ L_h$ for $s_1 = 0$. That maximum shifts towards smaller t values as the surface recombination velocity s_1 is increased. All the above considerations relate to a classical photodiode with a thick p-type region ($d = \infty$).

The optimum junction depth at which the greatest photodiode sensitivity obtained is also depended on the surface recombination velocity. For $s_1 = 0$ the depth of the junction must be very small. When s_1 increases, the optimum junction depth also increases.

It remains to be determined if the conclusions on the symmetric junctions with thick quasineutral p-type region hold for non-symmetric p^+-n (n^+-p) type junctions, for

which greater quantum efficiency values can be obtained. It can be seen that they hold indeed. In p^+-n (n^+-p) structures, the concentrations of impurities on the $p^+(n^+)$ type side are high ($>10^{25}$ m^{-3}). This indicates that illumination of the p^+-n (n^+-p) junction from the $p^+(n^+)$ side, the thickness of the illuminated junction region must be small to eliminate absorption of radiation by free carriers.

2.1.3 Photodiode response time

Photodiodes are often used in optical fiber communication systems and data links. In such applications, the important characteristics other than high quantum efficiency are frequency response.

Let us first consider the equivalent circuit of the p-n junction as shown in Figure 2.5, where the light-generated current I_{ph} is represented by a constant current source. It consists of a junction capacitance C, a shunt resistance R_{sh}, and a series resistance R_s. R_L is a load resistance [2.6-2.8].

The frequency response of a photodiode is mainly limited by the time needed for the photo-induced carriers to cross the depletion region (transit time) and by the RC-time constant, which is the product of capacitance and resistance in the bias circuit.

RC-time constant

The limitation of frequency response due to the RC-time constant is a common problem in photodiodes. The depletion layer acts as a capacitor (junction capacitance). Under reverse bias, the junction capacitance, C_j, can be expressed as

$$C_j = \varepsilon_s \varepsilon_0 / W_i \qquad (2.19)$$

where W_i is the thickness of the depletion layer.

For input light modulated in a rectangular fashion is allowed to incident, both current pulses and voltage pulses are generated at the load resistance, R_L. The rise time and fall time are determined by the time constant, C_j (R_s + R_L). For a high frequency photodiode, the series resistance must be as small as possible (usually less than 10 Ω).

Transit time within the depletion layer

The transit time, which is the time required for photo-induced carriers to cross the depletion region, is determined by drift velocity of the photo-induced carriers and the width of depletion layer. The drift velocity is proportional to the mobility of the carriers and the magnitude of the electrical field. In sufficiently high fields at high reverse voltages, the drift velocity of electrons and holes approached a scattering-limited value and becomes constant. The constant drift velocity is called the saturation velocity, v_{ds}. The transit time t_{tr} is equal to W_i/v_{ds}. Thus, the frequency corresponds to the conditions when the magnitude decreases by $2^{-1/2}$ defines the cutoff frequency, $f_{c\text{-}tr}$, which is given as

$$f_{c-tr} \approx 2.8/2\pi t_{tr} \approx 0.4/t_{tr} \quad (2.20)$$

It is noted that the cutoff frequency determined by the *RC* time constant is often lower than the transit time.

2.1.4 Noise mechanisms in photodiodes and receiver sensitivity

Quantum noise and thermal noise

Noise is an important factor when photodiodes are used as receivers in equipment such as optical fiber communication systems and data links. The noise in photodiodes consists of quantum noise (or shot noise) and thermal noise (or Johnson noise or Nyquist noise) and often limits the performance of the equipment and systems. The shot noise is the main noise in photodiodes and is induced the photo-induced carriers and incident photons as particles. The thermal noise is generated in the resistor connected to the photodiode and is caused by the random thermal motion of carriers.

The photodiode generates a photocurrent when incident photons are absorbed. The motion of the generated carriers is also relatively random and these contribute to the photocurrent. Consequently, a fluctuation due to the random motion and independent generation of the carriers is created. The mean-square shot noise current in the frequency range between f and $(f + \Delta f)$ is given by the following equation: [2.9-10]

$$\overline{i_{sn}^2} = 2q\bar{I}\Delta f \quad (2.21)$$

where $\bar{I}$ is the total current. The shot noise is almost independent of frequency (white noise).

The Johnson noise originates from the random motion of carriers with average thermal energy $(3/2)k_BT$ in a resistor at temperature T. This random motion produces a noise current in the load resistance, and the corresponding noise voltage across the load resistance introduces a noise current to the photodiode biasing circuit. The mean-square Johnson noise current within the bandwidth, B_{bw} (= Δf), is given by the following equation:

$$\overline{i_{sn}^2} = 4k_BTB_{bw} / R_{eq} \quad (2.22)$$

where R_{eq} is the total equivalent resistance. The mean-square Johnson noise current, inversely proportional to the resistance, is also a white noise.

Both the shot noise and Johnson noise are white noises and are independent of the frequency. At frequencies lower than 1 kHz, $1/f$ noise (or flicker noise) increases and becomes dominant as frequency decreases further.

Signal-to-noise (power) ratio and receiver sensitivity

The signal-to noise power ratio (SNR) is an important characteristic in photodetectors. If the total signal power is given by $R_{eq}\overline{i_{ph-sig}^2}$ and the total noise power is $R_{eq}(\overline{i_{sn}^2} + \overline{i_{sn}^2})$, the signal-to-noise power ratio is given by

$$S_{rms} / N_{rms} = \overline{i_{ph-sig}^2}/(\overline{i_{sn}^2} + \overline{i_{Jn}^2}) = \frac{\overline{i_{ph-sig}^2}}{2q\bar{I}B_{bw} + 4k_BTB_{bw} / R_{eq}} \quad (2.23)$$

where the subscript, rms, denotes root mean square. The signal-to-noise ratio (SNR) is related to sensitivity. The sensitivity of a photodetector is often expressed as noise equivalent power (NEP). The NEP is the input rms optical power per unit bandwidth at which the photocurrent is equal to the noise current and corresponds to the minimum input optical power detectable at $(S/N)_{rms}=1$. The performance of the photodiode is inversely related to the NEP. NEP depends on bandwidth. For an entire measurement bandwidth, the optical power required to produce a SNR of unity is [2.10],

$$P_t = NEP\sqrt{B_{bw}} \quad (2.24)$$

We often use another figure of merit, detectivity D^*, to determine the ultimate detection limit. D^* is given by

$$D^* = \frac{\sqrt{AB_{bw}}}{NEP}(cm \cdot Hz^{1/2} \cdot W^{-1}) \quad (2.25)$$

where A is the area of the photodetector on which light is incident. Reducing the photodetector dark current is important as NEP and D^* also decrease.

2.2 Sample preparation and device fabrication

In the present work, Bridgman grown p-type $CuInSe_2$ single crystals were used as the substrates to fabricate photodetectors. The $CuInSe_2$ photodetectors have a n^+-p structure, where the n^+-type layer was formed by indium diffusion. The fabrication processes employed during this work are illustrated in Figure 2.6 in a block diagram form.

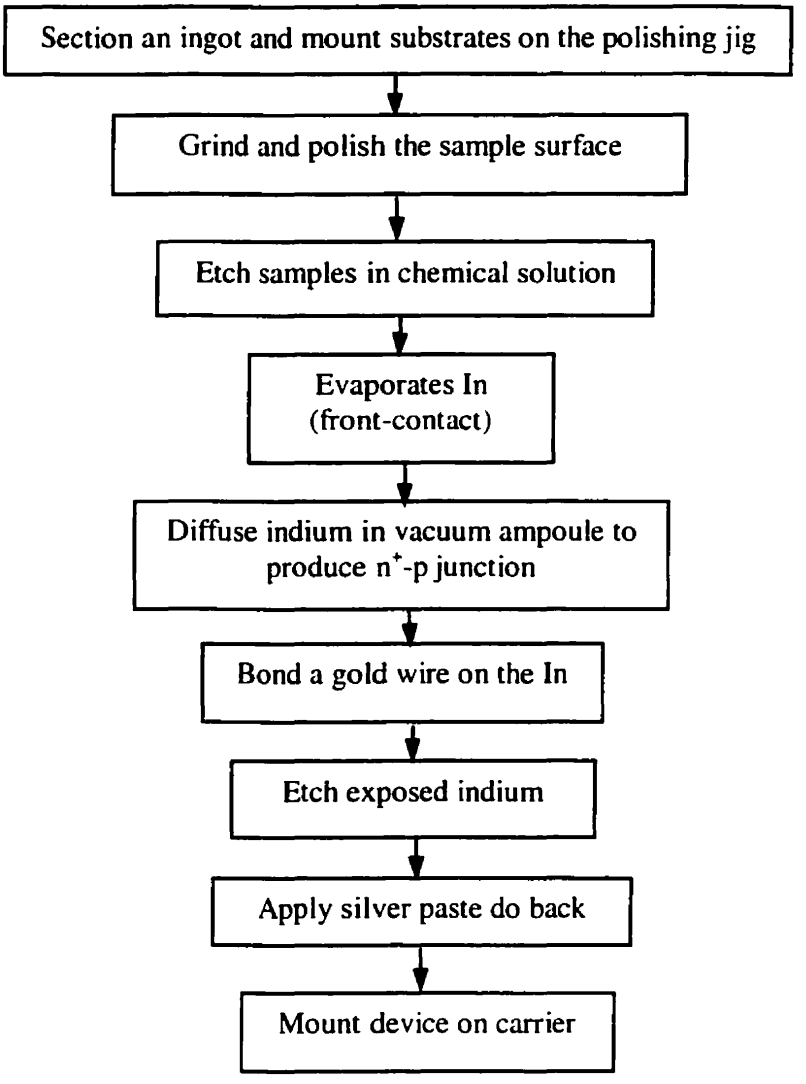

Figure 2.6 Basic fabrication steps for In-diffused $CuInSe_2$ homojunction photodetectors.

The fabrication steps and conditions are described below.

2.2.1 Preparation of substrates

The main steps to polish the substrate are described as follows:

- Cleave the sample to get specimens.
- Attach the specimens on a plexi-glass holder (see Figure 2.7). Grind the specimens with a 600-grit silicon carbide paper, mounted on a rotating polishing wheel, until the

sample and the holder are at the same level. Dimensions of particles of the 600-grit silicon carbide are about 15 microns. Rinse the specimen and holder with DI water and dry them.

- Do coarse polishing of the specimen surface with an abrasive of 6 μm diameter diamond powder. Figure 2.8 shows a schematic diagram of the polishing machine and polishing holder. Apply Kerosene (about 1.5~2 cm^3 liquid) as lubricant for the diamond abrasive. Perform the polishing in the two cross directions, each direction for a period of 3-5 minutes. Before changing the polishing direction, check the sample surface and make sure no cross scratches on it. After changing the polishing direction several times, rotate the sample in a circular manner with the sample still on the polishing cloth for 3-5 minutes. The total polishing time required is decided by the polishing wheel speed, applied force, and the amount of polishing powder. Typical polishing time used in this work ranges from 20 to 30 minutes. Note that it is important to ensure no clear scratch trace on the specimen surface. Wash the specimen and holder with DI water and wind dry.
- Continue the polishing using 1 μm diameter diamond abrasive, again in the two cross directions. Each direction for a period of 3-5 minutes and check the polishing surface, then change the polishing direction. After changing the polishing directions several times, rotate the sample in a circular manner on the polishing cloth for 3-5 minutes. The polishing time using 1 μm diameter diamond abrasive is also decided by the polishing wheel speed, add force, the amount of polishing powder. When no clear scratch trace on the sample surface is visible, we can stop this step. After this, wash the specimen and holder and dry them.
- Polish on a felt polishing cloth with 0.05 μm diameter alumina powder for another 20 minutes. Polish in the two cross directions. Each direction for a period of 5 minutes. Rotate the sample in a circular manner on the polishing cloth for 5 minutes. Make sure no clear scratch trace on the sample surface. After the polishing, the surface should be mirror-like with no visible scratches. Rinse the sample with DI water.

The purpose of the above-described polishing is to provide a smooth, spectacular surface on which device features can be photoengraved. To insure achievement of such surfaces,

one must have a clear understanding of each specific stage. In the following, I will explain the above steps in detail.

While slicing, grinding, coarse polishing, and fine polishing procedures are rather standardized in industrial polishing, the polishing procedures and conditions may vary considerably from lab to lab. Slicing is particularly important because it determines the specimens surface orientation and thickness.

To prepare substrates in the present work, the ingot grown by the horizontal Bridgman method is cut into 1 mm thick pieces, without specific orientation control. The other method used is to break the ingot and get some cleavage surface of single crystal. Then the back surface parallel to the cleaved surface is polished. These two methods never select specific crystal orientation. The ingot grown by the Bridgman method contains single crystal grains, with a length of about 5 cm and a diameter of 1.5 cm. Some large single crystal grains are present at the leading portion of the ingot, sometimes in the middle portion. The occurrence of single crystal cleavage surface is random but not always perpendicular to the ingot axis. Due to the lengthy crystal growth process, limited number of single crystal substrates was available. The selection of substrates with designated orientations appeared to be difficult. Therefore, substrates with random orientations were used in this work. Previous results from our laboratory on single crystal photodetectors suggested that the effect of orientation on device performance was not obvious [2.11-2.12]. Between these two methods, the last one was observed to yield cleavage surfaces for the fabrication of detectors. A pair of tweezers was used to induce shock to the ingot to obtain cleavage pieces. When the cutting method was used the yield of obtaining samples with large grains is low.

Grinding

The grinding produces a flat surface, which is required for the subsequent polishing. Employing polishing particles with a large diameter can shorten the polishing time but create deep scratches. As $CuInSe_2$ material is quite brittle, silicon carbide powder with a size of 600-grit was used for the grinding.

Polishing

Polishing is one of the important steps in the preparation of specimens for device fabrication. It consists of covering a polishing wheel with a suitable cloth, applying an appropriate polishing media and lubricant, and polishing until all traces of the prior surface finish are removed. The purpose of the polishing is to remove the grinding scratches and the heavily deformed layer brought about by the grinding procedures. The polishing includes a coarse polishing step and a final polishing step.

Coarse polishing

This stage may be considered the most important in the entire preparation procedure. The nature of the abrasive type employed is important. In our lab oratory, we employ 6 μm and 1 μm diamond powder to perform the coarse polishing.

Abrasives

A sufficiently coarse abrasive should be used in order to complete this stage in a minimum time. However, the selection of abrasive is greatly dependent upon the particle sizes and material types to be used in subsequent operations.

Diamond abrasives have the properties of high hardness, inertness and low coefficient of friction. Diamond particles retain their shapes and size during polishing and produce a uniform and high material removal rate with minimal surface damage.
Diameters of particles in general use are in the range of 0-10 microns. The 6 micrometers classification will produce a high removal rate for most materials. A sharp decrease in removal rates under similar conditions is expected when diamond powder with smaller size is used.

Suspension medium

The suspension medium for diamond powders is also important as it provides particle suspension, contributes to lubrication, and removal rate. Some adjustments in viscosity of the medium must be made for various particle sizes to compensate for possible drastic charges in heat generation.

Kerosene provides superior lubrication and removal rates in comparison to slurry suspensions. The reason is due to the fact that the particles are uniformly dispersed and held in a definite suspension. The paste-like material facilitates convenient charging of the polishing cloth surface and the addition of an extender contributes to even particle distribution.

Polishing cloths

Red felt cloth was used during the coarse polishing. Red felt can be used in many applications. It is best suited when used with an intermediate diamond compound (6 μm and 1 μm diameter). It is hard, durable and can be used on a wide variety of materials. Lecloth cloth was used to do the final polishing. The Lecloth one is the most versatile polishing cloth. It has a medium nap that is excellent for final polishing.

When using diamond abrasives, improved removal rates are encouraged by low viscosity oil extenders. The cloth should always show a slight excess of vehicle to insure good lubricity and swarf removal. The removal rates are decided by the speed of polishing plate, particle size, and add pressure.

Final polishing

Alumina exists in two allotropic forms: (1) alpha, which has a hexagonal crystal structure, and (2) gamma, which has a cubic crystal structure. The polishing characteristics of each differ in that alpha alumina removes metal faster and is more suitable for rough polishing. The gamma alumina has slower metal removal rates but produces a better finish and is usually reserved for the final polish. Alumina is available in three types of dispersion: (1) in a dry powder form, (2) in a suspension form, and (3) in an atomized container. Any of the three perform equally, but the dry alumina is least expensive. Whichever is used, the polishing cloth is wetted first before adding the aluimna. If dry alumina is used, a slurry is applied on the polishing wheel by mixing water and alumina. In this work, a suspension form is found to be better.

As previously stated, the final polishing stage serves to remove any deformation zone resulted from coarse polishing. Here, a uniformly polished and scratch-free surface must be produced by controlling the polishing plate speed, particle size, and add pressure.

Polishing time

In a previous work [2.12], about 30 to 45 minutes of polishing was needed for each step and only one substrate was mounted in a sample holder for each polishing run. Later Dr. Lam [2.13] found that up to six $CuInSe_2$ substrates could be mounted onto the same sample holder and polished at the same time. Furthermore, the polishing time was reduced from 30 minutes to 15 minutes for each polishing step. In this work, it was discovered that polishing time is mainly decided by the speed of polishing plate, particle size, and the applied pressure.

As our polishing is achieved manually, the applied pressure is not controlled precisely. By examining the polishing surface, one can determine the required time to obtain flat surfaces.

Ultrasonic cleaning for $CuInSe_2$ substrates

Like in the cleaning process for Si, some workers use ultrasonic cleaning to clean samples in trichloroethylene (>2 minutes) and in acetone (>2 minutes). The ultrasonic cleaning was performed on the $CuInSe_2$ samples, but it was observed that the cleaning often led to damage of the surfaces. Using ultrasonic cleaning for a period of 2 minutes, the surface damages are observable. Because $CuInSe_2$ cleave easily, it can be damaged when using ultrasonic vibration.

Etching in Br-methanol solution

Following the polishing, the substrates were rinsed using trichlorethylene (TCE), acetone (ACE) and then deionized (D.I.) water to remove contaminations resulting from the polishing. The substrates were then etched in a Br-methanol solution (0.5% Br by volume). The etching time was kept to be about 15 seconds. For a period longer than one minute, or etching in solutions of higher Br concentration must be avoided to prevent excessive etching. Excessive etching results in non-stoichiometric surface atomic concentrations and even etch pits. Comparison of the sample surface before and after the process showed that strict control the etching time and solution concentration is important. A appropriate etching time can eliminate the shallow polishing scratches, make the sample surface like mirror. A longer etching time will cause triangular etch pits. If $CuInSe_2$ is

etched for longer than 30 seconds, the density of etching pits will be too high to fabricate p-n junctions. Following the etching process, the sample is rinsed thoroughly with DI water and dried.

2.2.2 Evaporation of indium

After the drying, the sample was loaded immediately into the chamber of a vacuum system for indium evaporation. High purity indium was evaporated on the substrate through a metal mask, having circular windows with an area of 0.785 mm^2. The aluminum mask was placed in front of the samples during the evaporation. This mask was designed so that on each sample, there were 3 to 6 indium regions, to form 3 to 6 homojunction devices. The distance between the substrates and the boat for In during the evaporation process was about 12 cm. An aluminum shutter was provided to control the evaporation time and the thickness of the films. A schematic diagram of the evaporation system for the deposition of indium contacts is shown in Figure 2.9.

After evaporating of indium, the I-V properties of indium-$CuInSe_2$ junctions were studied. As indium is very soft material, figure 2.10 shows an extension probe using a thin copper wire for the measurements. We found some samples have large leakage currents. But after a diffusion process, I-V characteristics generally improved as the junction depth is deeper.

The thickness of the evaporated In layer was important for obtaining a reliable bonding of a conducting wire. Typical In thickness required for bonding is about 2 μm.

2.2.3 Diffusion of indium

We firstly prepare the ampoule. A schematic diagram of the ampoule used in the present study is shown in Figure 2.11. The outer diameter (OD) and inner diameter (ID) of the glass tubes were 1.6 cm and 1.2 cm, respectively. Before forming the ampoule, one end of the glass tube was sealed by a C_2H_2/O_2 torch. The glass tube (with one end sealed) was first cleaned with trichlorethylene (TCE), acetone (ACE) and then rinsed with deionized (D. I.) water. Following the cleaning process, the glass tube was put in an oven set at 200 °C to dry. The glass tube was then narrowed to half of the diameter at about 8-10 cm from the sealed end. This narrowing process was important because it helped to

seal off the ampoule at this narrowed region more easily. After the narrowing process, the ampoule was flame-polished first in air for about ten minutes and cooled down. Then the sample was put into the tube. The other end of the tube was connected to a vacuum system and allowed to pump down to 5×10^{-6} torr and then sealed by the C_2H_2/O_2 torch.

After the ampoule was made, it was introduced into an oven set at a temperature 200 °C to diffuse indium for various times. After each diffusion period, the ampoule was cooled to room temperature.

2.2.4 Bonding a wire

The wire bonding was done using Wood's alloy which has a low melting point. To avoid excessive heating, a low temperature (~100 °C) soldering iron was used.

After the diffusion, the ohmic contact was made directly on the indium surface by soldering a metal wire using the Wood's alloy (50% Bi, 25% Sn and 12.5% Cd, m.p. 71°C).

Initially, bonding of copper wire (diameter about 70 microns) was tried but the results were not satisfactory due to the stresses induced. Thin gold wire (diameter = 36 μm) was then tried. Before bonding, a layer of Wood's alloy was applied to one end of the gold wire. Then the gold wire was heated by the low temperature soldering iron with a sharp tip. The soldering iron was only allowed to touch the In layer on the sample surface very briefly to complete the wire bonding. This process was done under an optical microscope.

2.2.5 Etching of indium

After bonding the wire, it is required to etch the indium layer not covered by the Wood's alloy using a diluted HCl solution (10% by volume). This was done in order to ensure that the incident light can reach the junction during characterization. It is noted that the etching time for the exposed indium is quite critical to obtain a good device. After this, a layer of Ag conductive paste was applied to the polished back surface of the sample to form a ohmic contact. Figure 2.12 shows the cross-sections of samples at different process steps of the fabrication.

It is thus clear that there were three difficulties needed to be overcome in the fabrication of indium diffusion $CuInSe_2$ homojunction detectors.

Firstly, a very shallow p-n junction is needed.

Secondly, bonding a conducting wire is a critical.

Thirdly, etching the exposed indium is difficult to control.

After each fabrication step, the measured I-V and C-V characteristics were obtained and the results will be shown in the later chapters.

Figure 2.12 gives block diagrams of the five main fabrication steps. After each step, the sample surface was examined under microscope. From step 2 to step 5, the electrical properties of the sample were also measured. At the beginning of this work, many processes and runs were tried in order to find a solution to overcome the difficulties. Table 2.4 summarizes all of the samples fabricated in this work. From these experiments, the optimized conditions to do indium diffusion for the formation of p-n homojunction $CuInSe_2$ detectors were obtained. Successful measurements carried out on the working samples are summarized in Table 2.3.

2.3 Electrical measurements

Electrical properties of samples taken from different ingots were measured. A hot point probe was first used to determine the conduction type. The van der Pauw method was then employed for Hall effect measurements to obtain the mobility, resistivity, and carrier concentration of the samples. Results of the measurements for five samples used in this work are summarized in Table 2.2.

The samples listed in Table 2.3 were specifically characterized in this study.

2.4 Conclusions

In this section, basic operation principles of photodiodes were first introduced. Following this, design and device parameters required were discussed briefly based on a simplified analysis of receiver sensitivity and response speed.

The basic requirements of high-performance photodiodes can be summarized as follows:

1. The diode dark current needs to be as low as possible. The current dependence of the sensitivity is greater at lower signal bit rates.
2. A high-quantum efficiency is needed. The minimum detectable signal level is inversely proportional to the quantum efficiency.
3. A low diode capacitance is required. The diode capacitance should be low so that the diode can operate at a high speed. This will also allow sensitivity to be high because it enables one to use a large load resistance.

Table 2.1 Fabrication conditions for the $CuInSe_2$ homojunctins

Sample No.	Doping source	Diffusion time (minutes) 200°C	Treating time (minutes) 100°C
LS25	In	7	10
3CIS90051A	In	15	10
3CIS90051B	In	12	27
LS1A	In	5	10
LS1D	In	3	10
LS1E	In	1.5	10
LS35A	In	7	10
84HSF65	In	4	10

Table 2.2 Results of hot point probe and Hall effect measurements

Sample No.	Conduction type	Mobility (cm^2/V-s)	Resistivity (ohm-cm)	Carrier Concentration (cm^{-3})
LS1	P	35	1.3	1.1×10^{16}
LS25	P	45	1.7	4.3×10^{17}
LS35	P	41	0.9	5.1×10^{16}
3CIS90051	P	30	2.1	3.1×10^{17}
84HSF64	P	25	1.8	1.7×10^{17}

Table 2.3 A summary of measurements carried out on the samples

Sample	I-V	C-V	Quantum efficiency	Bandwidth
LS25	x	X	x	
3CIS90051 A	x	X	x	
3CIS90051 B	x	x	x	
LS1A	x	x	x	x
LS1D	x	x	x	x
LS1E	x	x	x	
LS35	x	x	x	
84HSF65	x	x	x	x

Table 2.4 A summary of samples prepared during the present work (× represents fail step; ∨ represents successful step)

Sample No.	Step 1 Substrate preparation	Step 2 Indium evaporation	Step 3 Indium diffusion	Step 4 Wire bonding	Step 5 Exposed In etching
$CuInSe_2$ 40	$\times^{(1)}$				
$CuInSe_2$ 13	$\times^{(1)}$				
$CuInSe_2$ 38	$\times^{(1)}$				
$CuInSe_2$ 46-a	$\times^{(1)}$				
$CuInSe_2$ 46-b	∨	$\times^{(2)}$			
LS32-a	∨	$\times^{(2)}$			
LS32-b	∨	$\times^{(3)}$			
$CuInSe_2$ 35	∨	$\times^{(3)}$			
$CuInSe_2$ 31	∨	$\times^{(4)}$			
$CuInSe_2$ 44	∨	$\times^{(4)}$			

LS28-a	v	v	x[5]		
LS28-b	v	v	x[5]		
LS 28-c	v	v	x[5]		
LS47-a	v	v	v	x[6]	
LS47-b	v	v	v	x[6]	
LS47-c	v	v	v	x[6]	
LS25-a	v	v	v	v	x[7]
LS25-b	v	v	v	v	x[7]
LS25-c	v	v	v	x[8]	
CIS8808026a	v	v	v	x[8]	
CIS8808026b	v	v	v	x[8]	
LS10-a	v	v	v	v	x[9]
LS10-b	v	v	v	v	x[9]
84HSF65-a	v	v	v	v	x[9]
LS1-c	v	v	v	v	x[9]
LS25	v	v	v	v	v
3CIS90051A	v	v	v	v	v
3CIS90051B	v	v	v	v	v
LS1A	v	v	v	v	v
LS1D	v	v	v	v	v
LS1E	v	v	v	v	v
LS35	v	v	v	v	v
84HSF65	v	v	v	v	v

Notation:

(1) surface has scratches, pits, or wavy patterns;

(2) Poor contact between sample and mask;

(3) Sample damaged during *I-V* measurements;

(4) Thickness of In too small;

(5) Diffusion time too long;

(6) Unable to bond a copper wire;

(7) After bonding and etching the exposed indium, the copper wire detached;

(8) Unable to bond a gold wire;

(9) Gold wire detached during etching of the exposed indium.

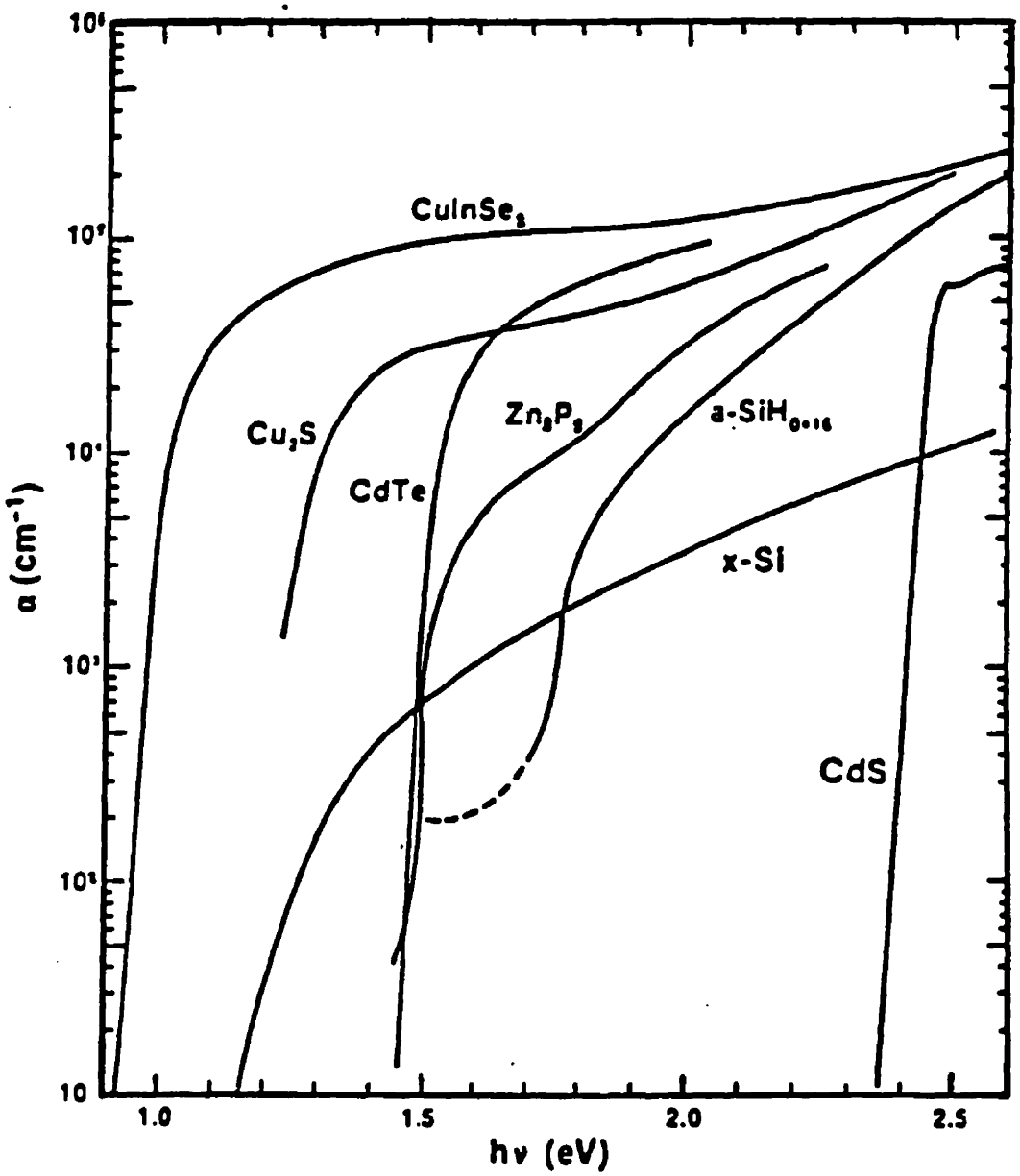

Figure 2.1 Absorption coefficients of some semiconductor materials [2.1].

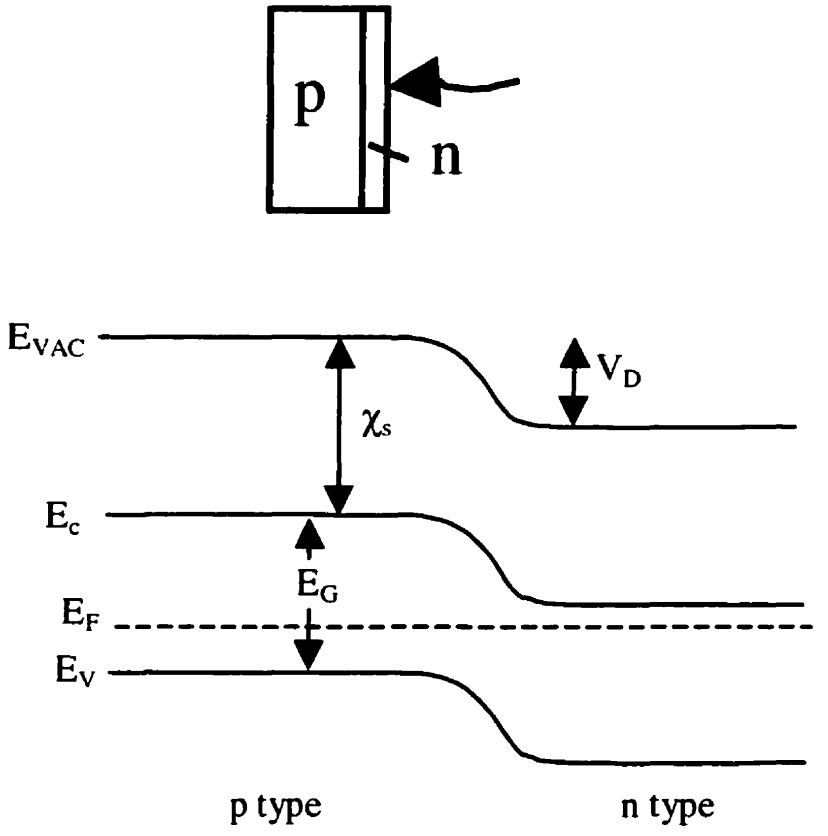

Figure 2.2. Energy band diagram for a p-n homojunction in a semiconductor.

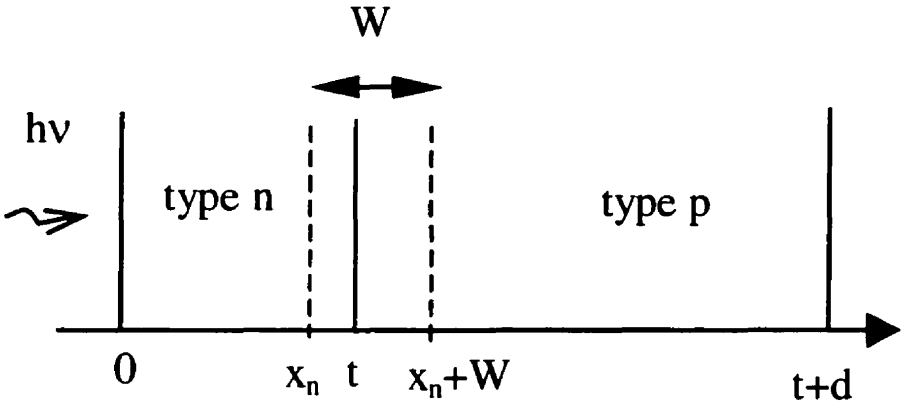

Figure 2.3. A one-dimensional photodiode model.

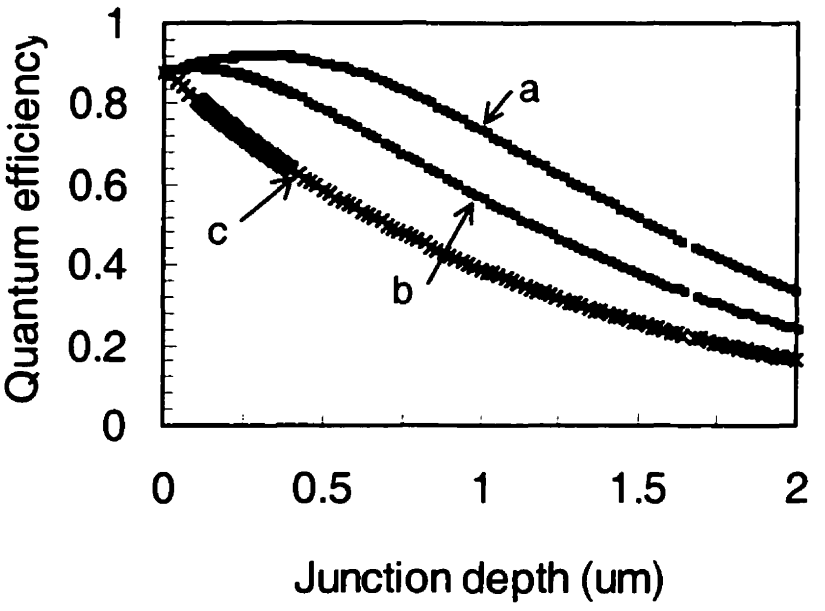

Figure 2.4 Dependence of the quantum efficiency on the normalized thickness of the junction illuminated region at (a) S_l=0 (γ_l=0), (b) S_l=10 m/sec (γ_l=1.287), and (c) S_l=100 m/sec (γ_l=128.7). In the calculation it was assumed d=∞, L_n=L_h=1μm, W=0.5μm and α=2×10^6 m^{-1}. x_n= t. The calculation was based on the Eq. (2.15)-(2.18).

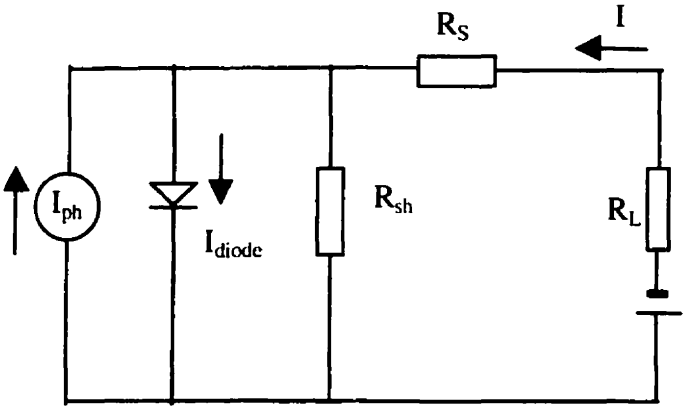

Fig. 2.5 An equivalent circuit of the practical photodetector under reverse bias.

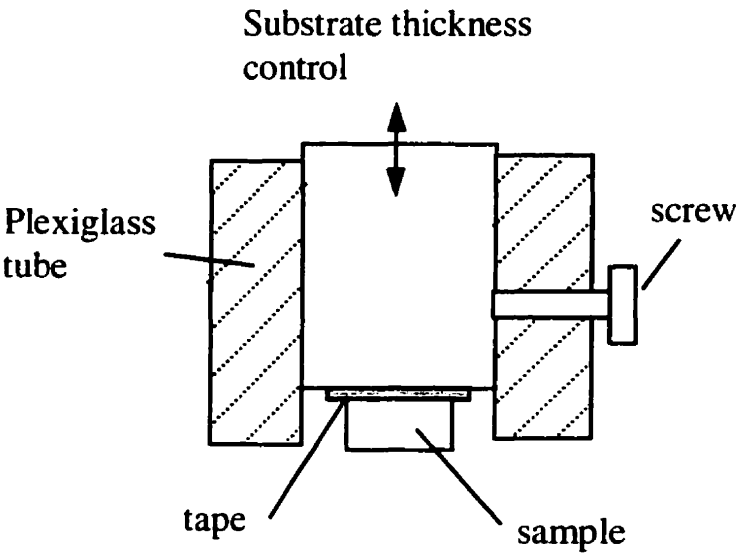

Figure 2.7 A schematic diagram of the polishing jig.

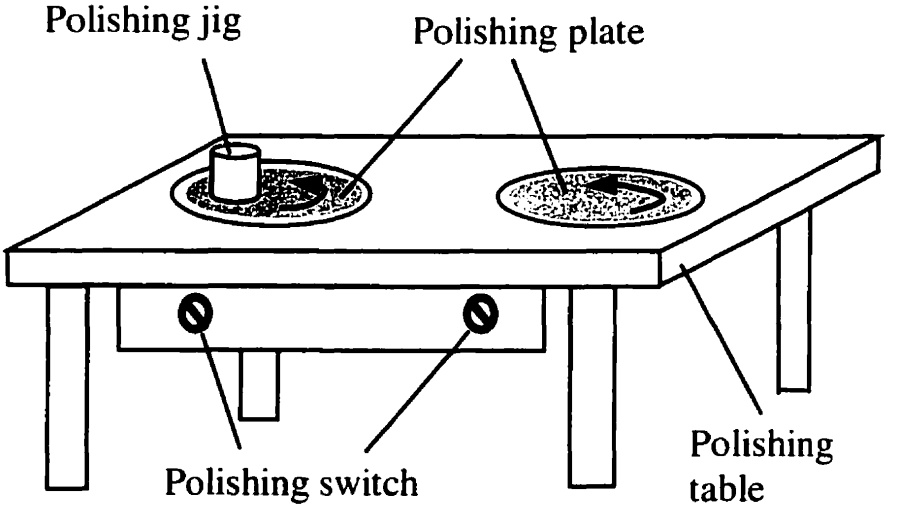

Figure 2.8 A polishing machine and the polishing jig.

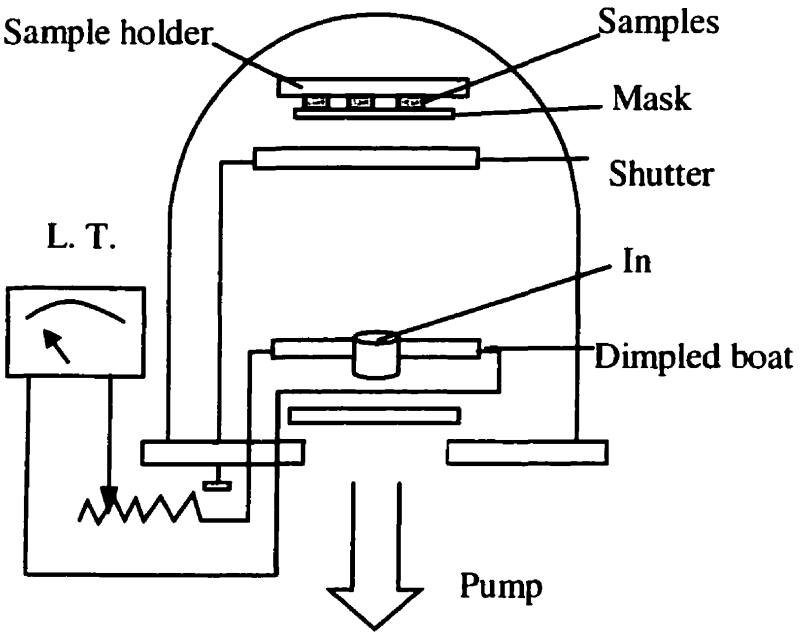

Figure 2.9 A schematic diagram of the vacuum system for the evaporation of indium.

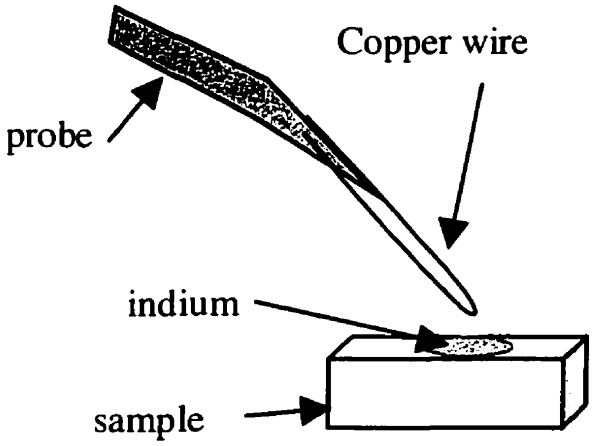

Figure 2.10 An extension probe using a thin copper wire for the measurements.

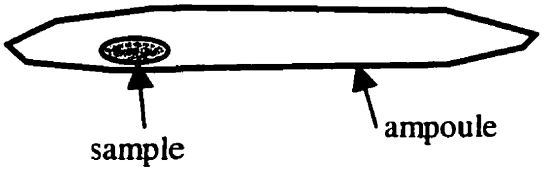

Figure 2.11 A schematic diagram of a glass ampoule.

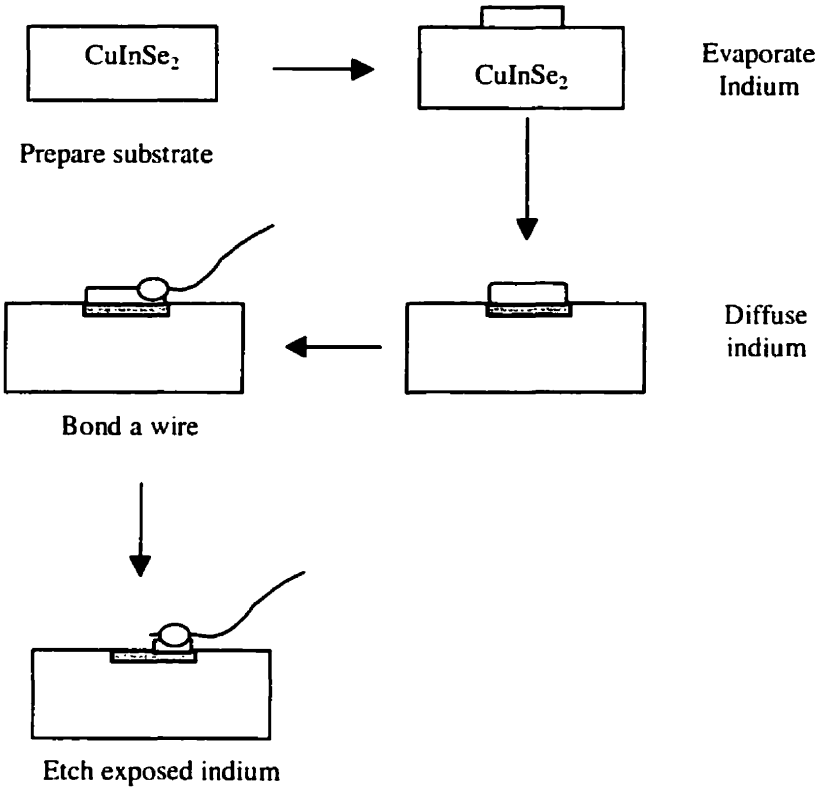

Figure 2.12 Cross-sections of samples at different fabrication steps.

Chapter 3

Dark Current-Voltage Characterization

In this chapter, dark current-voltage characterization of the fabricated devices will be described. As most of the photodiodes are operated under reverse bias, their dark currents will influence the signal/noise ratio. Therefore, it is important to understand the dark current mechanism in the fabricated photodiodes.

3.1 Dark current-voltage characteristics in a homojunction

For an ideal diode under forward bias in the dark, electrons are injected into the p-type region from the n-type region; they pass from the n-type region where they are majority carriers, through the depletion region, and into the p-type quasi-neutral region where they are minority carriers. In the p-type region they recombine with majority carrier holes, and the current flow is completed by a current of holes from the p-type ohmic contact supplied through the external circuit. Similar statements could be made about the current due to holes. The current density due to diffusion is given by [3.1],

$$J_{dif} = qn_i^2\left[\frac{(D_n/\tau_n)^{1/2}}{N_A}+\frac{(D_p/\tau_p)^{1/2}}{N_D}\right]\left[\exp(qV/kT)-1\right] \quad (3.1)$$

where n_i is the intrinsic carrier density, N_A is the density of acceptors in the p-type region, and N_D is the density of donors in the n-type region.

The diode saturation current is

$$I_0 = qn_i^2 A\left[\frac{(D_n/\tau_n)^{1/2}}{N_A}+\frac{(D_p/\tau_p)^{1/2}}{N_D}\right] \quad (3.2)$$

Here, A is the diode junction area.

The diode current-voltage relation can be expressed as

$$I = I_0\left[\exp(qV/nkT)-1\right] \quad (3.3)$$

Here $n = 1$ for the ideal diode. Dark *I-V* characteristics of the ideal diode are shown in Fig. 3.1. The series resistance is zero, and the shunt resistance is infinite.

In a practical device, the n value may lie between one and two. The departures from the ideal diode are mainly due to: (1) the surface effect, (2) the generation and recombination of carriers in the depletion layer, (3) the tunneling of carriers between states in the bandgap, (4) the high-injection condition that may occur even at relatively small forward bias, and (5) the series resistance effect.

For a practical diode, there exist a series resistance R_s and a shunt resistance R_{sh}. The series resistance comes from the ohmic contact in the front surface, the substrate in the back side, and the resistance from the measurement circuits. While the shunt resistance comes from the defects of the surface and the traps in the depletion layer. All of the above produce a leakage current different from the ideal device. This can be observed in *I-V* characteristics at the reverse bias because the shunt resistance is dominant under small forward bias and reverse bias. The equivalent circuit of a practical diode is shown in Fig. 3.2, and the *I-V* characteristics are given by [3.4]:

$$I = I_0 \exp\left[\frac{q(V - IR_S)}{nkT} - 1\right] + \frac{V - IR_S}{R_{sh}} \qquad (3.4)$$

where n is the ideality factor. Equation (3.4) is now plotted in Figure 3.3. it is seen that the *I-V* curve deviates from linearity at high currents due to the series resistance.

From *I-V* properties of the diode, the diode ideal factor n, the series resistance R_s, and the shunt resistance R_{sh} can be deduced using the following method.

In a log(I) versus V plot, the slope of linear region is given by

$$S = \frac{d\log(I)}{dV} \qquad (3.5)$$

Knowledge the slope and the sample temperature allows the ideality factor to be determined using the relationship

$$n = \frac{1}{\ln(10)SkT/q} = \frac{1}{2.3SkT/q} \qquad (3.6)$$

The deviation of the log (I)-V curve from linearity is $\Delta V = IR_s$, here R_s is series resistance and is given by

$$R_s = \frac{\Delta V}{I} \quad (3.7)$$

The shunt resistance R_{sh} can be determined by the Eq. (3.4) curve-fitting approach. Another method is through measurement of the open-circuit voltage V_{oc} and the short-circuit current I_{sc} under illumination. From the results, the shunt resistance R_{sh} can be simply expressed as [3.4]

$$R_{sh} \approx \frac{V_{oc}}{I_{sc}} \quad (3.8)$$

The I_{sc}-V_{oc} plot has a linear region with a slope of $1/R_{sh}$. The curve becomes nonlinear under high illumination intensities, and Eq. (3.8) becomes invalid.

If the series resistance R_s is large, the photodiode RC time constant is large and most current will be loaded on the series resistance. The performance of the photodetector will degrade. For good quality photodetectors, the series resistance usually is less than 10 Ω.

3.2 Experimental set-up and results

The dark d.c. current was measured by an HP-4145A semiconductor parameter analyzer. The HP-4145A analyzer is a 16-bit multi-microprocessor-based test instrument for measuring, analyzing and graphically displaying the d.c. characteristics of common semiconductor devices and ICs. For the present study, the bias voltage typically ranges from -0.5 to +0.5 V with steps of 0.05 V at room temperature.

Table 3.1 summarizes the current-voltages parameters of the $CuInSe_2$ photodetectors studied. These results were obtained from the final devices. In the fabrication, some current-voltage characteristics for various devices were also obtained and the results are shown in Figure 3.4 to Figure 3.17.

Figure 3.4 and Figure 3.5 show the influence of different treating times on the photodetector LS1A-a. Each treatment experiment took a period of about 5 minutes. At a treatment temperature of 100 °C, the best *I-V* results were obtained after being treated for 10 minutes. (The forward-to-reverse current ratio at about 0.5 V is the largest). Results similar to the above were also observed on several other samples. For subsequent experiments, the total treating time was set for 10 minutes.

After the best treating time has been obtained, ammonia was also adopted to rinse the surfaces of the photodetectors. During the last fabrication step, HCl was used to etch the exposed indium. In this etching process, some chlorine ions remained on n^+-p junction surfaces. Ammonia was used to remove the chlorine ions.

As stated before, for an ideal diode, the ideality factor is equal to 1 because diffusion current is dominant. If the recombination current is dominant, then $n = 2$. When both currents contribute to the total current, n has a value between 1 and 2. For our devices, The smallest n factor observed on the sample No.84HSF65-g is 1.5, which is larger than 1. This implies that a significant recombination process is present in the device. From Fig. 3.5, we can see that the leakage current is about 100 nA. This large leakage current implies the existence of the interface states as well as the deep levels in the device.

The series resistance for all of the samples ranges from 150 to 210 ohms. It is noted that the series resistance is dependent on the junction depth, the impurity concentration of the p-type and n-type regions, and properties of the back surface ohmic contacts.

Variations between the characteristics of photodetectors from the same crystal substrate were observed to be large. The variations were even greater between the different crystals. In Figures 3.4-3.17, these variations in characteristics are shown.

This is not surprising since many of the factors that can influence the I-V characteristics were not controlled, partly because of the limited amount of samples that were available but primarily due to the difficulty in doing so. The net substrate acceptor concentration as determined by C-V measurements varied from 10^{16} cm^{-3} to 10^{17} cm^{-3} with the higher values being more common. Furthermore, the abrasive substrate polishing was performed manually which resulted in poor control over the applied pressure which can lead to variations from one sample to another. Despite the above variations, differences between the set of heat treated and non-heat treated crystals were clearly apparent.

As illustrated in Figure 3.12, the two quasi-linear regions can be fitted by an expression of the form

$$J = J_s \exp(\frac{qV}{nKT}) \text{ for } qV >> kT \qquad (3.9)$$

At higher forward bias > 0.5 volt, the effects of the series resistance R_s became apparent. Values of the series resistance were estimated by examining the differential resistance of the *I-V* curves at a large forward bias.

The values of series resistance obtained were from about 100 ohms to 250 ohms. The series resistance values were depended on the junction depth, the impurity concentration of the p-type and n-type region, and properties of the front surface ohmic contacts.

3.3 Dark current mechanisms

For a practical diode, several current components flow through the p-n junction, both in the forward and reverse except the diffusion current. Although the exact causes of the current may be difficult to know, the main components are believed to be generation-recombination, surface leakage, and tunneling.

Generation-recombination current

Generation-recombination of carriers in the depletion region contributes to a significant part of the total current. Under forward bias it is mainly due to the recombination of injected carriers, whereas under reverse bias in which no carriers are injected it is due to the generation process. The recombination current caused by deep levels in the depletion layer is expressed as

$$J_{re} = (qW/2) n_i \sigma_r v_{th} N_t \exp(qV/2k_BT) \qquad (3.10)$$

where W is the width of the depletion layer, $\sigma_r = \sigma_n = \sigma_p$, σ_p, σ_n are the hole and electron capture cross sections, respectively, v_{th} is thermal velocity carriers, N_t the trap density. Here, it is also assumed that the energy level of the capture center lies at E_t.

Under the reverse bias, the generation current can be expressed by the following equation:

$$I_{dg-r} = qn_i W/\tau_{g-r} = qn_i W \sigma v_{th} N_t \qquad (3.11)$$

The generation-recombination current increases exponentially as the temperature increases or as the band-gap energy of the material decreases. The current depends on the defect density within the depletion layer. Hence, the defect density needs to be kept low during the crystal growth and fabrication processes. It is noted that the reverse current increases with the increase in the reverse bias, due to widening of the depletion layer. Figures 3.5, 3.7, 3.9, 3.11, 3.13, 3.15, 3.17 show the dark *I-V* characteristics for samples No. LS1A-a, LS1D-d, LS1D-i, LS35A-f, 84HSF65-L, LS1E-a respectively. The *n* factors for these samples are larger than 1.

Surface leakage current

The behavior of a p-n junction in the low-current range under reverse bias as well as forward bias is generally determined by the properties of the surface because there are more defects in this region than the inner region [3.2]. At the semiconductor surface, there are surface states. In addition, energy states are also formed at the interface between the semiconductor and a dielectric passivation film, when the surface is passivated. The density of the surface states and the interface states depend very much on device processing and the passivation method. The surface and interface states can easily trap carriers acting as generation-recombination centers. If the trap level is near the mid-gap, and electron and hole capture cross sections are nearly equal and the generation current will have the following additional surface leakage current:

$$I_{ds} = (qW_{sur}/2)n_i \sigma v_{th} N_{st} \quad (3.12)$$

where W_{sur} is the surface (interface) area of the p-n junction depletion layer, σ and N_{st} are the carrier capture cross section and the trap density at the surface (interface). Consequently, a surface leakage current will flow through a p-n junction formed on such a surface or interface and can affect the current-voltage characteristics of photodiodes under reverse bias. Therefore, the defect density at the surface (interface) needs to be kept low during the fabrication process in order to reduce the dark current. From figure 3.4-3.17, we can see that etching of indium in HCl has resulted in large reverse currents but has small influence in the forward currents. This implies that the etching has produced more surface states.

Tunneling current

Tunneling current [3.3] is due to quantum mechanical tunneling through the pn-junction. Because the energy and momentum are conserved during tunneling, this process occurs more readily in direct band-gap semiconductors. In indirect band-gap semiconductors, the tunneling probability is low because the transitions require a momentum change. The tunneling current is therefore more significant in photodiodes of direct band-gap semiconductors and operated under a large reverse bias. As our $CuInSe_2$ photodetectors were operated under low reverse bias voltage (-0.7 V), the tunneling current can be neglected.

From the above analysis, we can state that the diffusion current, generation-recombination current, and surface current are all present in our photodetectors.

3.4 Conclusions

The diffusion current appears both under forward and reverse bias. The diffusion current under reverse bias is called the saturation current. In our devices, the reverse current was not constant but increased gradually because of the additional current components. All these dark currents will give rise to noise. Therefore the reduction or current, especially surface leakage is important in order to obtain detectors with a high S/N ratio.

Table 3.1 I-V Properties for $CuInSe_2$ photodetectors.

Sample No.	Diffusion time (minutes)	Ideality factor, n	Leakage current at V=-0.5V (μA)	Washing with ammonia
LS1A-a	5	1.8	0.2408	Yes
LS1A-b	5	1.6	0.1077	Yes
LS1A-c	5	2.0	0.559	Yes
LS1A-d	5	2.3	0.7541	Yes
LS1A-e	5	1.9	0.3359	Yes

LS1D-a	5	3	0.6325	Yes
LS1D-d	5	2.4	0.2907	Yes
LS1D-e	5	3.2	0.7838	Yes
LS1D-f	5	2.9	0.5816	Yes
LS1D-g	5	3.4	1.412	Yes
LS1D-h	5	2.8	0.7728	Yes
LS1D-I	5	1.87	0.08025	Yes
LS1D-j	5	2.56	0.4835	Yes
LS1D-k	5	2.6	0.3207	Yes
LS1D-l	5	2.54	0.4854	Yes
LS1E-a	3	2.02	0.1741	No
LS1E-b	3	1.99	0.1625	No
LS1E-c	3	2.25	0.2947	No
LS1E-d	3	2.45	0.5377	No
LS1E-e	3	2.26	0.6573	No
LS35-f	1.5	2.47	0.4958	Yes
LS35-g	1.5	2.42	7.476	Yes
LS35-j	1.5	2.37	7.062	Yes
84HSF64-b	4	3.0	9.982	No
84HSF64-c	4	2.34	2.115	No
84HSF64-d	4	1.62	0.2045	No
84HSF64-e	4	2.6	1.74	No
84HSF64-f	4	2.2	2.095	No
84HSF64-g	4	1.8	0.07732	No
84HSF64-h	4	1.76	0.23	No
84HSF64-j	4	1.4	1.196	No
84HSF64-k	4	1.6	0.05982	No
84HSF64-l	4	1.63	0.1496	No
84HSF64-m	4	2.2	1.774	No

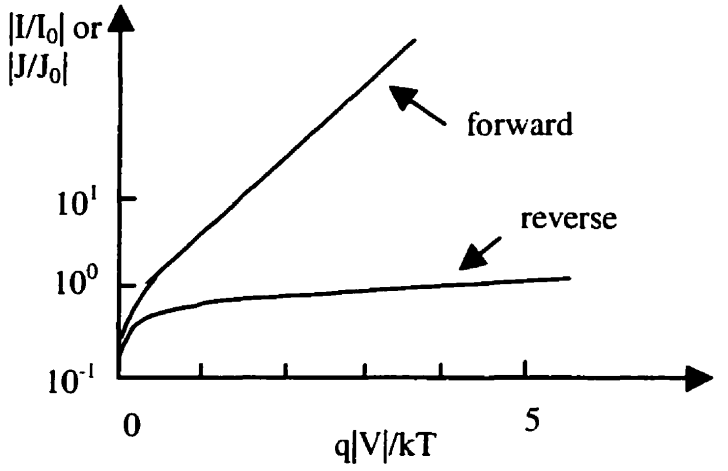

Fig. 3.1 Dark *I-V* characteristics of an ideal p-n junction.

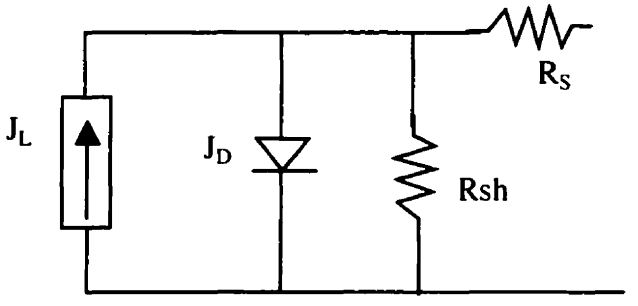

Figure 3.2. Simplified equivalent circuit for a photodetector, including a current generator, an ideal diode, a series resistor, and a shunt resistor.

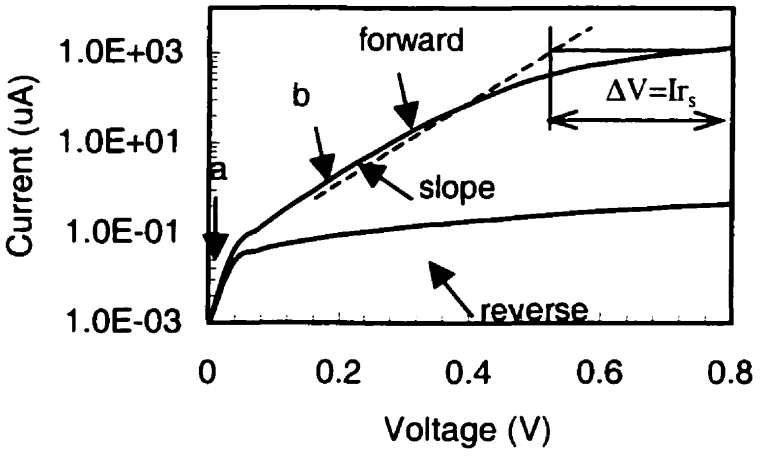

Figure 3.3 Log (I) versus V plots for a diode with series resisters. The upper dashed line is for r_s=0. (a) Generation-recombination current-dominated region. (b) diffusion current-dominated region.

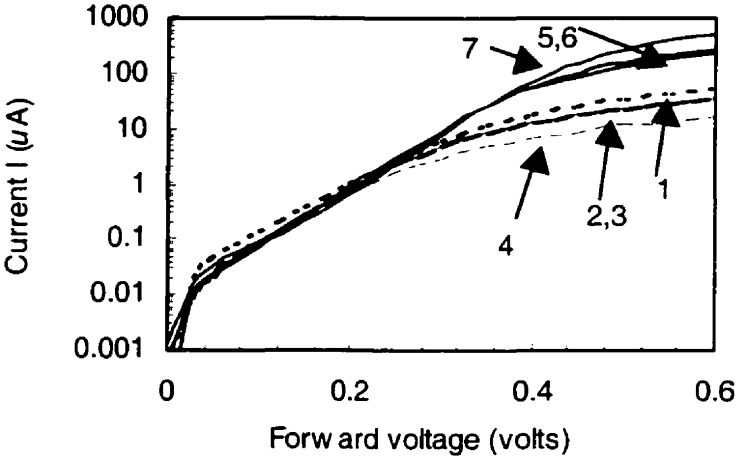

Figure 3.4. Forward I-V curves of sample LS1A-a. (1) After In diffusion, (2) after the first treatment (5 minutes), (3) after the second treatment (5 minutes), (4) after the third treatment (5 minutes), (5) after wire bonding, (6) after etching of the exposed In, (7) after rinsing with ammonia.

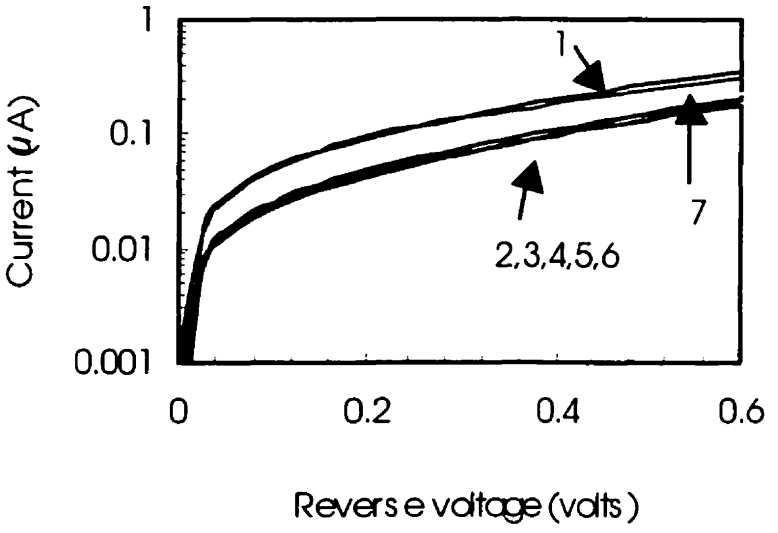

Figure 3.5. Reverse *I-V* curves of sample LS1A-a. (1) After In diffusion, (2) after the first treatment (5 minutes), (3) after the second treatment (5 minutes), (4) after the third treatment (5 minutes), (5) after wire bonding, (6) after etching of the exposed In, (7) after rinsing with ammonia.

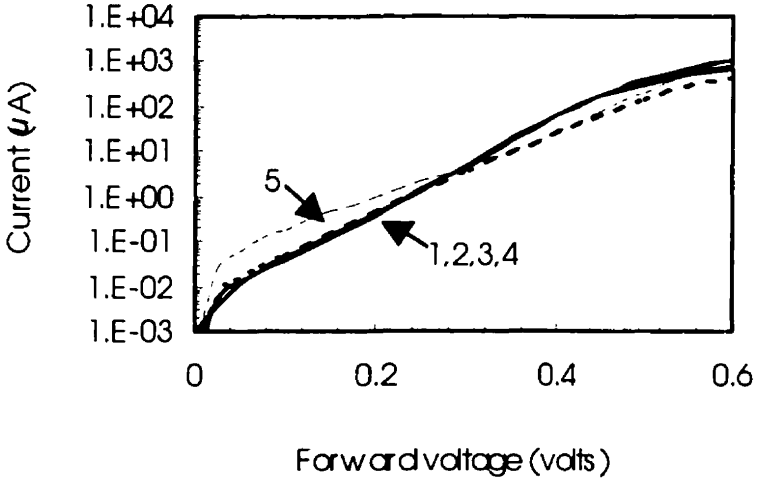

Figure 3.6. Forward *I-V* curves of sample LS1D-d. (1) After In diffusion for 3 minutes at 200 °C, (2) after treating for 10 minutes at 100 °C, (3) after wire bonding, (4) after etching of the exposed In, (5) after rinsing with ammonia.

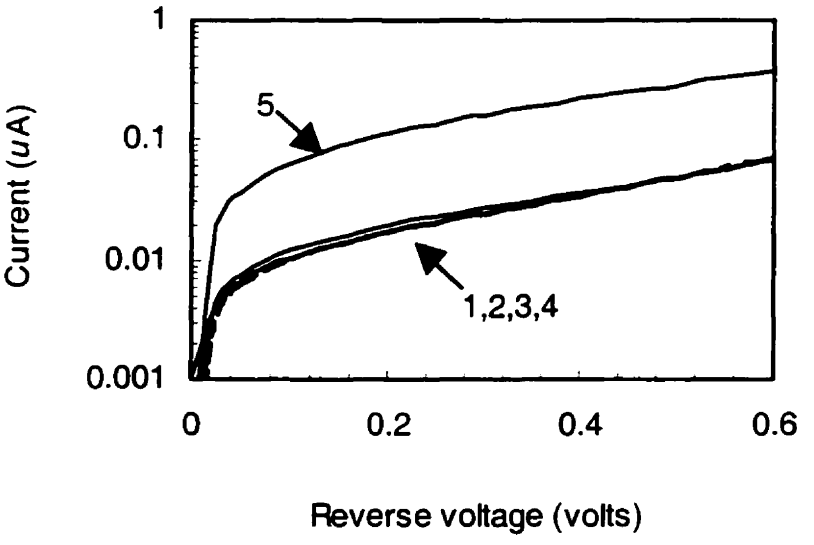

Figure 3.7. Reverse *I-V* curves of sample LS1D-d. (1) After In diffusion for 3 minutes at 200 °C, (2) after treating for 10 minutes at 100 °C, (3) after wire bonding, (4) after etching of the exposed In, (5) after rinsing with ammonia.

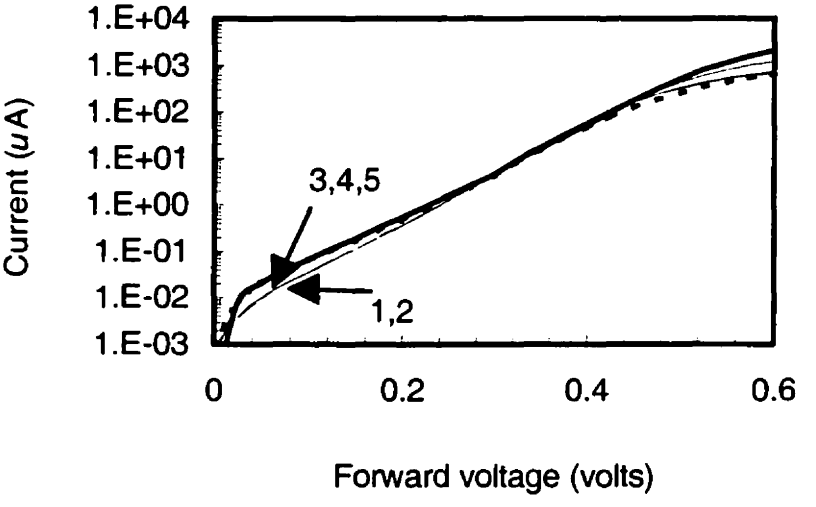

Figure 3.8. Forward *I-V* curves of sample LS1D-i. (1) After In diffusion for 3 minutes at 200 °C, (2) after treating for 10 minutes at 100 °C, (3) after wire bonding, (4) after etching the exposed In, (5) after rinsing with ammonia.

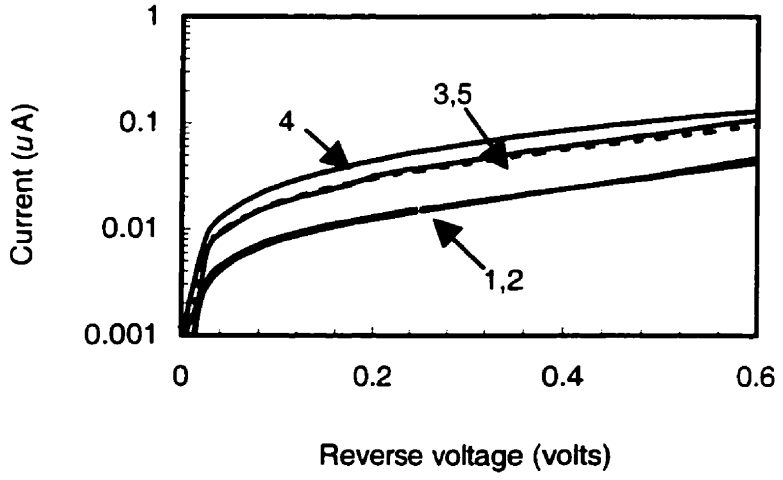

Figure 3.9. Reverse *I-V* curves of sample LS1D-i. (1) After In diffusion for 3 minutes at 200 °C, (2) after treating for 10 minutes at 100 °C, (3) after wire bonding, (4) after etching the exposed In, (5) after rinsing with ammonia.

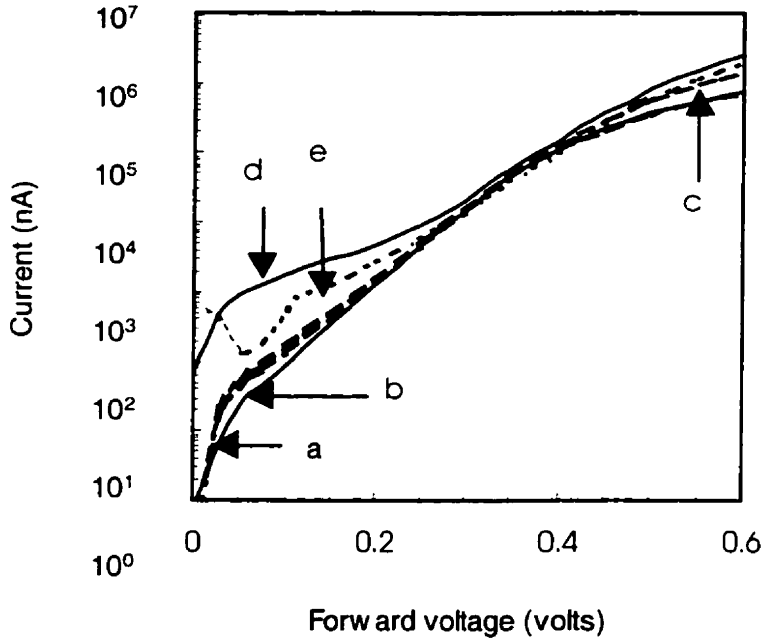

Figure 3.10. Forward *I-V* curves of sample LS35A-f. (a) After In evaporation, (b) after wire bonding, (c) after etching of In, (d) after second etching of In, (e) after rinsing with ammonia.

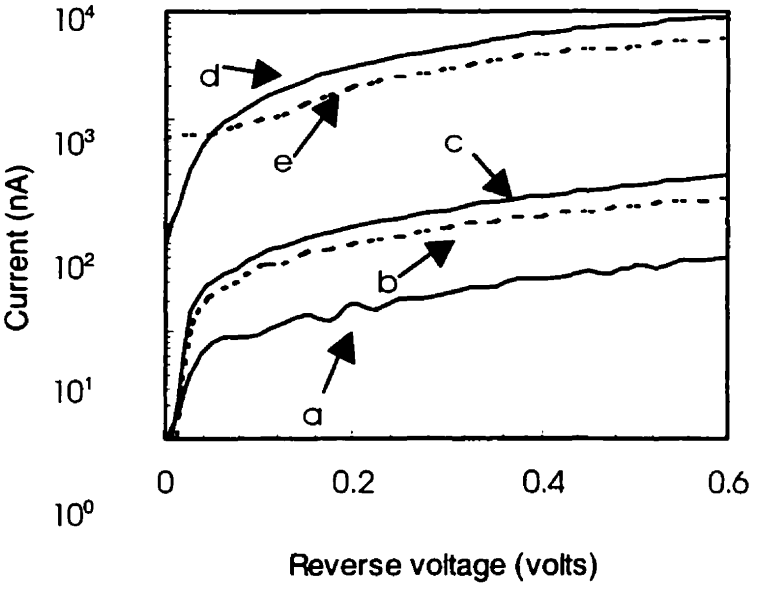

Figure 3.11. Reverse *I-V* curves of sample LS35A-f. (a) After In evaporation, (b) after wire bonding, (c) after etching of exposed In, (d) after second etching of In, (e) after rinsing with ammonia.

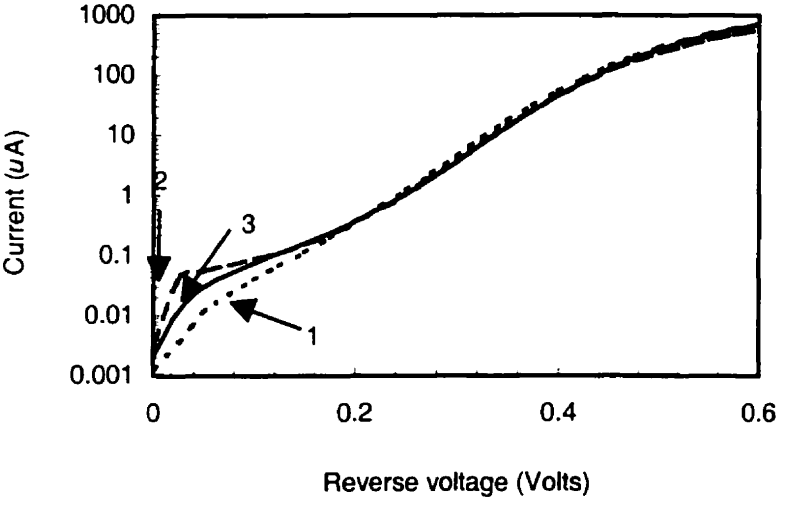

Figure 3.12. Forward *I-V* curves of sample 84HSF65-d. (1) After In diffusion for 4 minutes at 200 °C and treating for 10 minutes at 100 °C, (2) after wire bonding, (3) after etching of the exposed In.

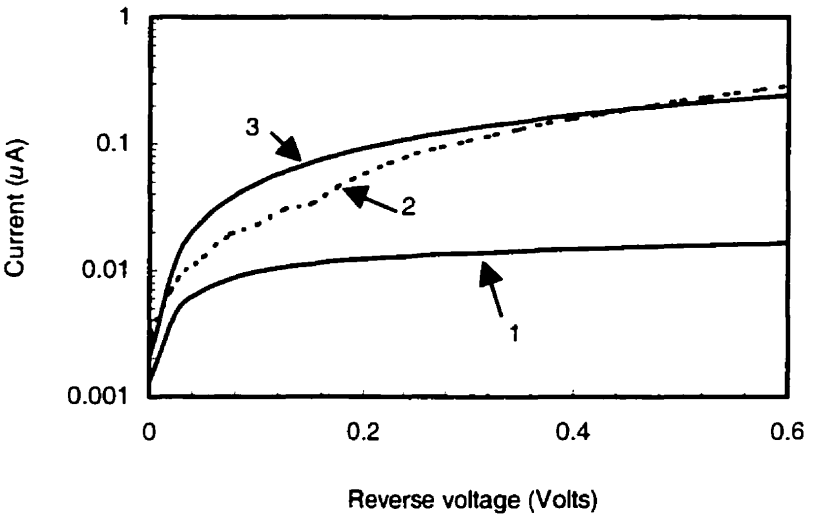

Figure 3.13. Reverse *I-V* curves of sample 84HSF65-d. (1) After In diffusion for 4 minutes at 200 °C and treating for 10 minutes at 100 °C, (2) after wire bonding, (3) after etching of the exposed In.

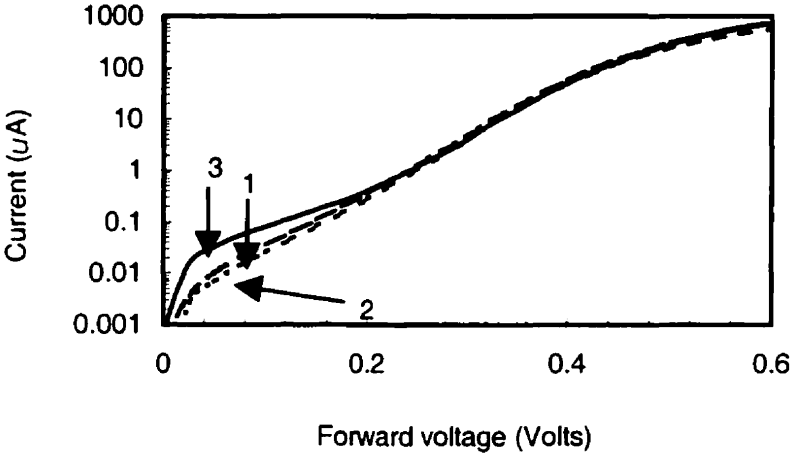

Figure 3.14. Forward *I-V* curves of sample 84HSF65-L. (1) After In diffusion for 4 minutes at 200 °C and treating for 10 minutes at 100 °C, (2) after wire bonding, (3) after etching of the exposed In.

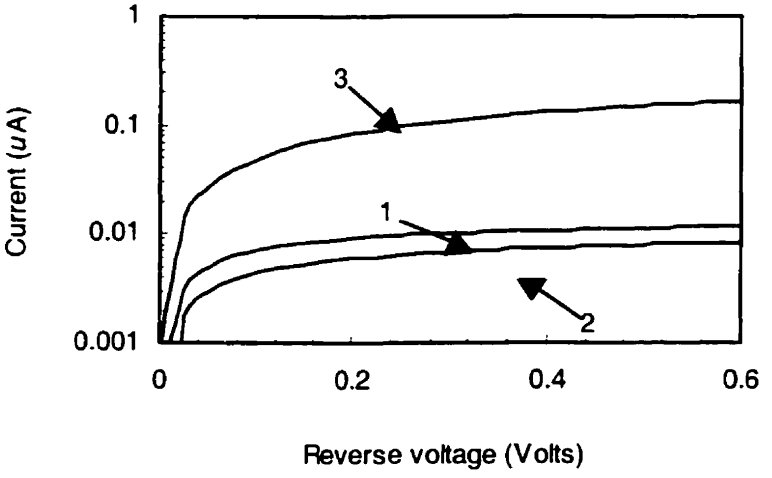

Figure 3.15. Reverse *I-V* curves of sample 84HSF65-L. (1) After In diffusion for 4 minutes at 200 °C and treating for 10 minutes at 100 °C, (2) after wire bonding, (3) after etching of the exposed In.

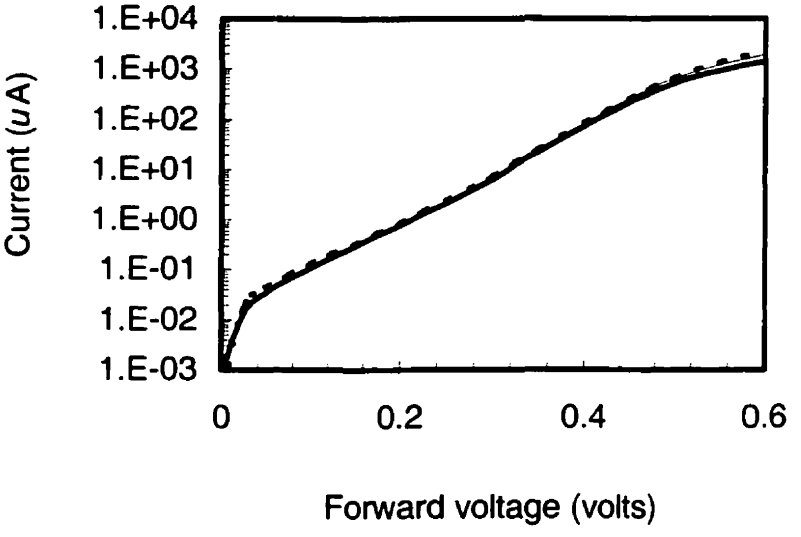

Figure 3.16. Forward *I-V* curves of sample LS1E-a. (1) After In diffusion for 1.5 minutes at 200 °C and treating for 10 minutes at 100 °C, (2) after wire bonding, (3) after etching of the exposed In.

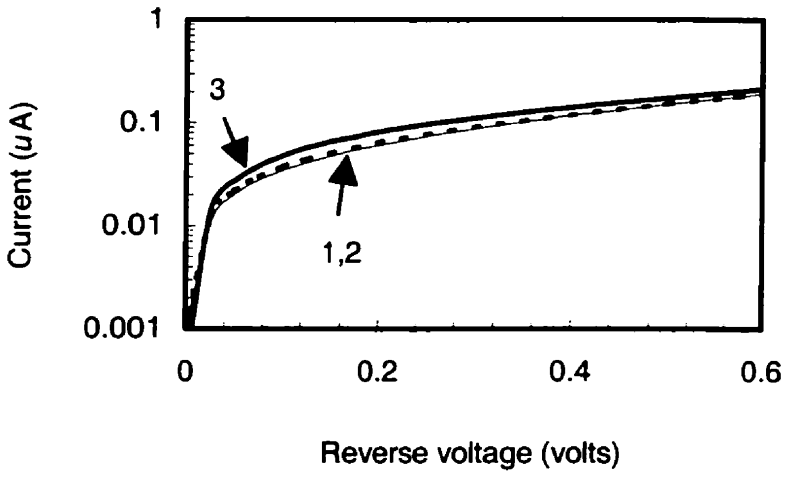

Figure 3.17. Reverse *I-V* curves of sample LS1E-a. (1) After In diffusion for 1.5 minutes at 200 °C and treating for 10 minutes at 100 °C, (2) after wire bonding, (3) after etching of the exposed In.

Chapter 4

C-V Characterization

The capacitance-voltage (*C-V*) characteristics of the indium diffused n^+-p $CuInSe_2$ homojunction detectors were measured and the results are presented in this chapter. From the *C-V* results, both the acceptor concentration distribution and the depletion region width of the detectors may be calculated. Through the capacitance-voltage measurements, influence of each fabrication step on the performance of the detectors may also be understood.

4.1 Capacitance of a n^+-p homojunction junction

The voltage dependence of the junction capacitance is commonly employed to study junction behavior and to determine junction-related parameters. Capacitance-voltage (*C-V*) measurements are often used to study junction properties such as the impurity concentration of the substrate, depletion width, the defect density and the barrier height. When a p-type semiconductor material is joined to an n-type material, a p-n junction is formed. Holes diffuse from p-type to n-type region due to a large concentration, electrons diffuse from n-type to p-type region. The diffusion of charge carriers results in a space charge region with an associated electric field which forces the electrons to drift back to the n-type region, and the holes back to the p-type region. If the diffusion action is comparable to the drift action, a thermal equilibrium state is reached and the net flow of carriers becomes zero. The charged region where the mobile carriers have been reduced is called the depletion region. When deep traps are ignored, the total charge density in the depletion region can be expressed as [4.1]

$$\rho(x) = q\left[p(x) - n(x) + N_D^+(x) - N_A^-(x)\right] \qquad (4.1)$$

where p(x) and n(x) are the hole and electron concentrations, respectively, $N_D^+(x)$ and $N_A^-(x)$ are the ionized impurity concentrations. For a one-sided abrupt n^+-p junction with

$N_D >> N_A$, assuming that the impurity atoms are totally ionized, Eq. (4.1) can be simplified as:

$$\rho(x) = -q[N_A(x) - p(x)] \qquad (4.2)$$

According to the Poisson's equation, the depletion width x is given by

$$x = \sqrt{\frac{2\varepsilon_r \varepsilon_0 (V_{bi} + V_R)}{qN_B}} \qquad (4.3)$$

where N_B is equal to N_A in the p-type semiconductor, V_{bi} is the built-in potential, V_R is the reverse voltage applied across the two terminals of the junction, ε_0 is the permittivity of free space (8.85×10^{-14} F/cm), and ε_r is the dielectric constant of the semiconductor (for $CuInSe_2$, $\varepsilon_r \approx 10$).

Since the charge stored in either side of the junction is directly proportional to the depletion-layer width, we have

$$Q = qAN_B x = A\sqrt{2q\varepsilon_r \varepsilon_0 (V_{bi} + V_R) N_B} \qquad (4.4)$$

where A is the area of the junction and x is the depletion width. The small signal capacitance of the space charge layer is defined by

$$C = \frac{dQ}{dV_R} \qquad (4.5)$$

Substituting Eq. (4.4) into Eq. (4.5) leads to

$$C = A\sqrt{\frac{q\varepsilon_r \varepsilon_0 N_B}{2(V_{bi} + V_R)}} \qquad (4.6)$$

C is called the transition or depletion layer capacitance.

According to Eq. (4.6), Eq. (4.3) can be rewritten as

$$x(V_R) = \frac{A\varepsilon_r \varepsilon_0}{C(V_R)} \qquad (4.7)$$

From Eq. (4.7) we can see that the depletion width can be obtained from C-V measurements.

In order to compare the measured diffusion lengths of different samples, the doping concentrations of the substrate need to be measured.

From Eq. (4.6), we have

$$\frac{1}{C^2} = \frac{2}{qA^2\varepsilon_r\varepsilon_0 N_B}(V_{bi} + V_R) \qquad (4.8)$$

then

$$\frac{d\left(\frac{1}{C^2}\right)}{dV} = \frac{2}{qA^2\varepsilon_r\varepsilon_0 N_B(x)} \qquad (4.9)$$

It is clear from the Eq. (4.8) that a plot of $1/C^2$ versus V_R should yield a straight line if the substrate is uniformly doped. The slope of the plot will give the impurity concentration of the substrate, N_B. Eq. (4.9) can be rewritten as

$$N_B = \frac{2}{q\varepsilon_r\varepsilon_0 A^2}\frac{1}{d(1/C^2)/dV_R} \qquad (4.10)$$

The width of the depletion layer, W, is given as

$$W = x_n + x_p = \left[\frac{2\varepsilon_r\varepsilon_0}{q}\left(\frac{1}{N_D} + \frac{1}{N_A}\right)|V_D|\right]^{1/2} \qquad (4.11)$$

When a negative bias, V, is applied to the junction, Eq. (4.11) can be rewritten as

$$W = \left[\frac{2\varepsilon_r\varepsilon_0}{q}\left(\frac{1}{N_D} + \frac{1}{N_A}\right)|V_D + V|\right]^{1/2} \qquad (4.12)$$

Hence, the width of the depletion layer in an abrupt junction changes in proportion to the square root of the potential difference, $(V_D + V)^{1/2}$.

In an abrupt pn-junction, positive space charge (+Q) in the n-type region and negative space charge (-Q) in the p-type region are adjacent to each other. The charge changes with the bias voltage, V. Consequently, an equivalent parallel plate capacitor is formed in the depletion region, and the capacitance per unit area (F/cm^2) is given by the first derivative of charge with respect to V:

$$C = \frac{dQ}{dV} = A\left[\frac{\varepsilon_r\varepsilon_0 qN_D N_A}{2(N_D + N_A)(V_D + V)}\right]^{1/2} \qquad (4.13)$$

By substituting Eq. (4.12) into Eq. (4.13),

$$C = \frac{A\varepsilon_r\varepsilon_0}{W} \qquad (4.14)$$

This equation gives the capacitance of the parallel plate capacitor having a unit area and a plate distance, W. The capacitance given by Eq. (4.14) is called the junction capacitance, the depletion layer capacitance, or the barrier capacitance. If $N_A >> N_D$, Eqs. (4.12) and (4.13) can be simplified as follows:

$$W = \left[\frac{2\varepsilon_r \varepsilon_0 (V_D + V)}{qN_D}\right]^{1/2} \quad (4.15)$$

$$C = A\left[\frac{\varepsilon_r \varepsilon_0 qN_D}{2(V_D + V)}\right]^{1/2} \quad (4.16)$$

From Eq. (4.16),

$$1/C^2 = \frac{2(V_D + V)}{A^2 q\varepsilon_r \varepsilon_0 N_D} \quad (4.17)$$

where A is the area of the p-n junction.

For a n^+-p abrupt junction, the concentration profile on the p-side, N_A, is given by:

$$N_A = \frac{2}{q\varepsilon_0 \varepsilon_r} \frac{1}{\dfrac{d\left[(A/C_p)^2\right]}{dV_R}} \quad (4.18)$$

where, ε_0 is the permittivity of free space, ε_r is the relative dielectric constant of the p-side, and q is the electronic charge. A is the junction area. Thus, by measuring the slope of the curve of $(A/C_p)^2$ against reverse voltage, an estimate of the carrier concentration can be obtained.

A grown junction is often abrupt, whereas a diffused junction which is formed by the impurity diffusion is often graded. The basic concepts for the analyses of the graded junction are similar to those for analyses of the abrupt junction. The behavior of the graded junction can be examined by solving the Poisson's equation for a given space-charge distribution. The space charge (or impurity) distribution can be expressed as $\rho(x) = qa_{grad}x$ for a linearly-graded junction, where a_{grad} (cm^{-4}) is the gradient of impurity concentration. The results obtained are as follows:

$$V_D = \frac{qa_{grad}W^3}{12\varepsilon_r \varepsilon_0} \quad (4.19)$$

$$W = \left[\frac{12\varepsilon_r\varepsilon_0(V_D + V)}{qa_{grad}}\right]^{1/3} \qquad (4.20)$$

and for a unit area of the p-n junction,

$$C = A\left[\frac{\varepsilon_r^2\varepsilon_0^2 qa_{grad}}{12(V_D + V)}\right]^{1/3} = \frac{A\varepsilon_r\varepsilon_0}{W} \qquad (4.21)$$

As indicated in Eqs. (4.19), (4.20), and (4.21), the built-in potential, the width of the depletion layer, and the junction capacitance are determined by the impurity concentration gradient. As the impurity concentration gradient decreases, the built-in potential and capacitance decrease and the depletion layer broadens. The width of the depletion layer is proportional to $(V_D + V)^{1/3}$ and the capacitance is inversely proportional to $(V_D + V)^{1/3}$.

4.2 Capacitance measurement considerations

The equivalent circuit of a p-n or Schottky diode consists of a junction capacitance C, a junction conductance G, and a series resistance r_s as shown in Fig. 4.1 (a) [4.2]. The conductance governs the junction leakage current and can be varied by processing conditions. The series resistance depends on the bulk wafer resistivity and on the contact resistances. Conventional capacitance meters (LCR) assume the device to be represented by either a parallel equivalent circuit in Fig. 4.1 (b) or a series equivalent circuit in Fig. 4.1 (c). Comparing the two circuits to the original circuit in Fig. 4.1 (a) allows C_p, G_p, C_s, and R_s to be written as

$$C_p = \frac{C}{(1 + r_s G)^2 + (\omega r_s C)^2}; \qquad G_p = \frac{G(1 + r_s G) + r_s(\omega C)^2}{(1 + r_s G)^2 + (\omega r_s C)^2}; \qquad (4.22)$$

$$Cs = C\left[1 + \left(\frac{G}{\omega C}\right)^2\right]; \qquad R_s = r_s + \frac{1}{G\left[1 + (\omega C/G)^2\right]}; \qquad (4.23)$$

where $\omega = 2\pi f$.

The series C_s is independent of the series resistance r_s, whereas C_p depends strongly on r_s. Both capacitances deviate from C at high G. Therefore, in order to

measure the true capacitance, $\omega C/G$ must be greater than 10. Otherwise, correction of series resistance effect must be made.

For proper interpretation of the capacitance measured by the LCR meter, considerations must be given to the complete circuit representation of the structure being tested. Capacitance meters assume the device represented by the parallel circuit of Fig. 4.1 (b) where C_p and G_p are the measured differential capacitance and conductance, respectively.

The complete small-signal circuit representation of a photodiode is more complicated. The most important parasitic circuit element is the series resistance, R_s, which depends on the bulk crystal resistivity and the back-contact resistance. The actual circuit representation of a photodiode is given in Fig. 4.1 (a) where C_p is the junction capacitance and G_p the junction conductance. This model can be extended to include the effects of back-contact capacitance, lead series inductance and stray capacitance of the probing station.

4.3 Capacitance-voltage measurements set-up

In this work, the *C-V* characteristics will be discussed qualitatively based on $1/C^2$ vs. *V* graphs obtained at different small signal frequencies. Ideally, if deep and interfacial states are not present, the *C-V* characteristics should not depend on the frequency of the small signal, which is superimposed onto the dc bias voltage (*V*). Thus, any frequency dependent *C-V* characteristics give strong evidence of deep and/or interfacial states. A schematic diagram of the *C-V* measurement system is shown in Fig. 4.2. The capacitance of the samples was measured by an HP 4274A multifrequency LCR meter. The voltage across the sample was determined by an HP 3478A multimeter. The LCR meter and the multimeter were connected to an IBM PC XT computer through an IEEE 488 bus. A computer program written in BASIC controlled the operation of the equipment and controlled the data acquisition as well as the data storage. The results of measurements were printed by a plotter or printer.

During the measurements, the LCR meter supplied a dc bias with values from 0.2 volt to −1 volt to the $CuInSe_2$ sample. A voltage increment of 0.02 volts was applied. The dc bias was then measured by the multimeter. The capacitance was measured in a parallel

mode, in which a capacitance was given in parallel to a conductance. A small ac voltage signal with amplitude of about 20 mV was superimposed on the dc bias and the frequency employed was from 1 kHz to 100 kHz. The resulting current was then measured to give the capacitance of the device at that particular dc bias. The capacitance and the dc bias for the specified voltage range were then recorded and stored on a floppy diskette. A low voltage sweep rate and a long waiting time were usually adopted to allow the device under test to stabilize before the measurements.

4.4 Experimental results

If traps or interface states exist in a sample, the depletion charge and junction capacitance will also be affected by the ionization of traps. The minority carrier diffusion length will be affected by the change of these ionized traps. Because the frequency of the small ac voltage has a strong effect on junction capacitance when deep levels exist in the depletion region, the capacitance measurements were carried out at different frequencies. In this manner, differences between the results could be seen.

The capacitance values were recorded as the reverse bias voltage was decreased from a maximum value towards a small forward bias at a constant sweep rate (mV/s). Figure 4.3 shows *C-V* curves obtained for the sample 84HSF65-g with different sweep rates. It is seen that the results are not sensitive to the sweep rate. Therefore, a high sweep rate may be used to measure the *C-V* curve.

In the present experiments, capacitance-voltage results of three n^+-p $CuInSe_2$ homojunctions have been obtained at a temperature of 300 K over a frequency range from 10^2 to 10^5 Hz. Figure 4.4 shows $1/C^2$-*V* curves at different frequencies where a dispersion is seen. One of the possible causes for the frequency dispersion of the capacitance is a large series resistance. However, the series resistance in our devices is no more than 300 ohms, so the series resistance should not have a significant effect on the capacitance dispersion. Another cause for frequency dispersion can be explained from the p-n junction model. The frequency dependence of the junction capacitance could be the result of finite time constants associated with the charging and discharging of the deep states close to the depletion edge. At low frequencies, the variation of small signal ac voltage is comparable to the time constants of the deep levels. Thus, the charging and

discharging of the deep states could follow the small signal variation. Such a phenomenon will contribute to the measured junction capacitance. Therefore, a higher junction capacitance is expected. At high frequencies, the charge variation on the deep states cannot follow the small signal voltage applied to the junction and hence cannot contribute to the junction capacitance. In this case, a lower capacitance value is anticipated. These could explain the frequency dispersion between the 1 kHz and 100 kHz of the present devices.

In order to determine whether this is due to surface states or deep levels, higher frequencies and larger reverse biases are needed. Higher frequencies were used because interface states and deep levels are not responsive to the small-signal voltage in *C-V* measurements. The use of larger reverse biases can allow one to probe deeper into the $CuInSe_2$ so that surface effect and bulk effect can be distinguished. As the breakdown voltage of our photodetector is only about -1 volt, so the large reverse voltage was not employed.

From Figure 4.5 to Figure 4.11 show *C-V* characteristics obtained from some of the photodetectors after different fabrication steps.

Figure 4.5 shows the influence of different treating times on *C-V* results for the photodetector LS1A-a. The duration of each treatment step was 5 minutes, at a temperature of 100°C. It should be noted that ammonia was also selected to rinse the etched photodetector. As described in Chapter 2 and Chapter 3, HCl was used to etch the exposed indium. Therefore, some chlorine ions would remain on n^+-p junction surfaces. The purpose of rinsing in ammonia was to reduce density of chlorine ions. Figures 4.5-4.7 show that ammonia rinsing is not always effective.

We can also see that the bonding or etching of indium sometimes induced a large carrier concentration change. Bonding a wire caused an increase a capacitance. Etching caused an increase in surface traps. Both these two factors can change $1/C^2$ versus V properties.

From the plots, the acceptor concentration was found to be in a range from 10^{16} to 10^{17} cm^{-3}. The depletion width varied from 0.3 μm to 0.8 μm (at -0.8 Volt).

4.5 Conclusions

Capacitance-Voltage (*C-V*) characteristics are important for studying junction properties such as the impurity concentration of the substrate, depletion width, the defect density and the barrier height. Through *C-V* curve measurements, the acceptor concentration distribution and the depletion region width of the photodetectors were obtained. Selected photodetectors with small capacitance values and with small series resistance, photodetector *RC* time constant can be optimized.

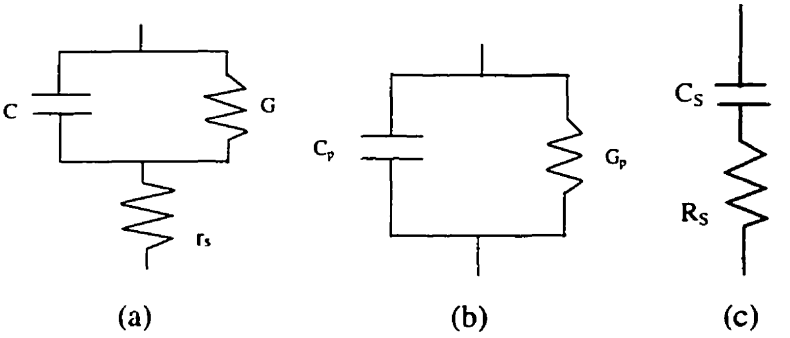

Figure 4.1. (a) Complete equivalent circuit, (b) parallel equivalent circuit, (c) series equivalent circuit for a p-n junction diode.

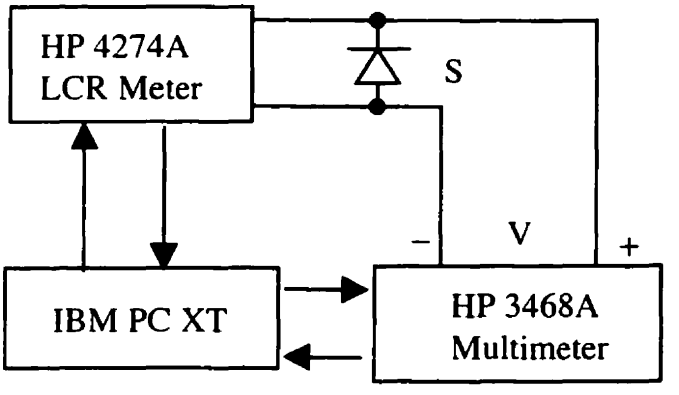

Figure 4.2 A circuit block diagram of the arrangement used for the capacitance-voltage measurements of the photodetectors.

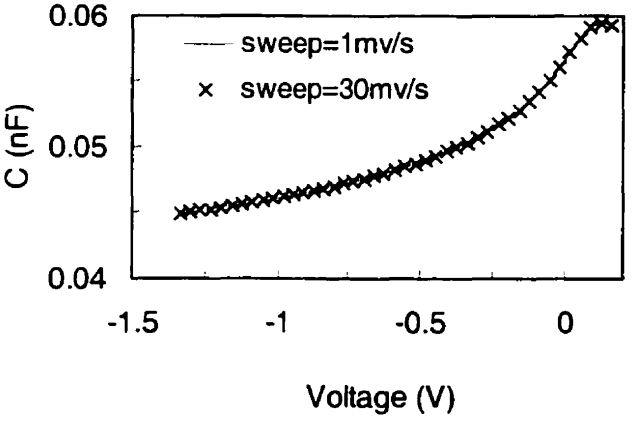

Figure 4.3 Effect of sweep rate on the capacitance versus voltage curve for photodetector 84HSF65-g.

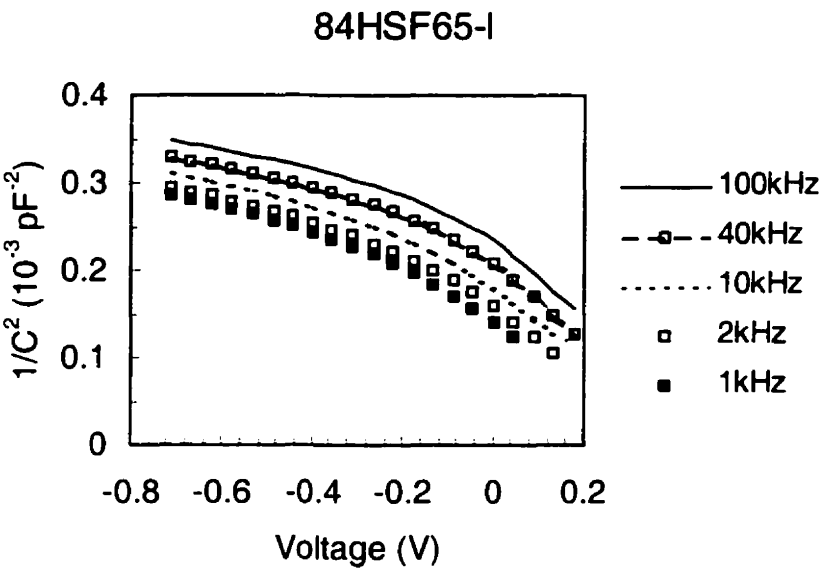

Figure 4.4. Results of *C-V* measurements on the photodetector 84HSF65-i at different frequencies and at room temperature.

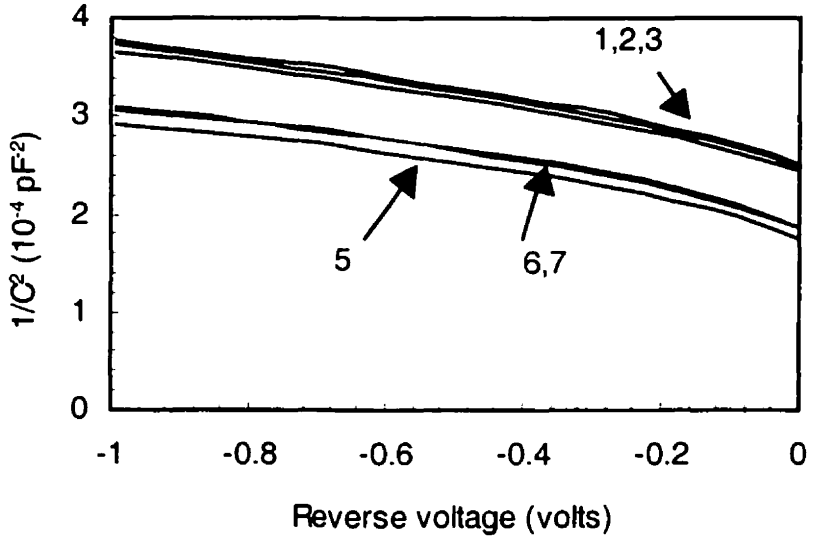

Figure 4.5 Results of *C-V* measurements for sample LS1A-a. (1) After In diffusion, (2) after the first treatment, (3) after the second treatment, (5) after wire bonding, (6) after etching of the exposed In, (7) after rinsing in ammonia. 100 kHz at room temperature.

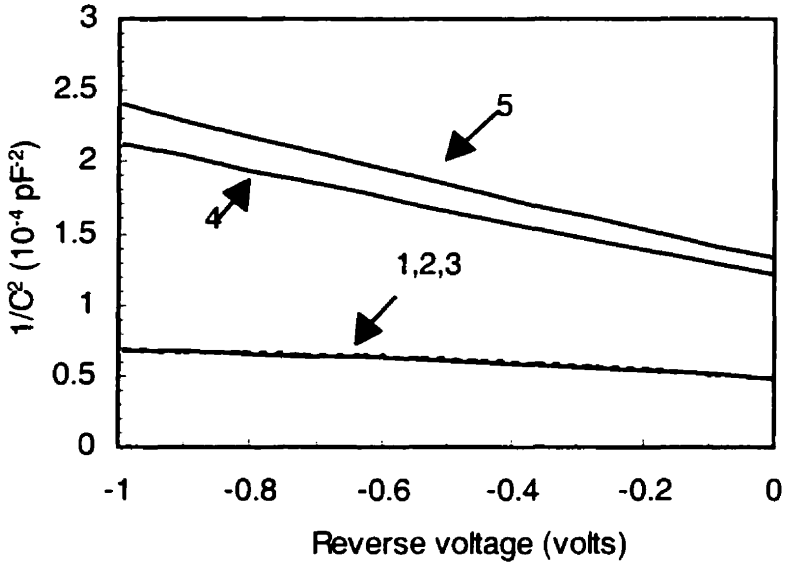

Figure 4.6. Results of *C-V* measurements on sample LS1D-e at 100 kHz at room temperature. (1) After In diffusion for 3 minutes at 200 °C, (2) after treating for 5 minutes at 100 °C, (3) after wire bonding, (4) after etching of the exposed In, (5) after rinsing with ammonia.

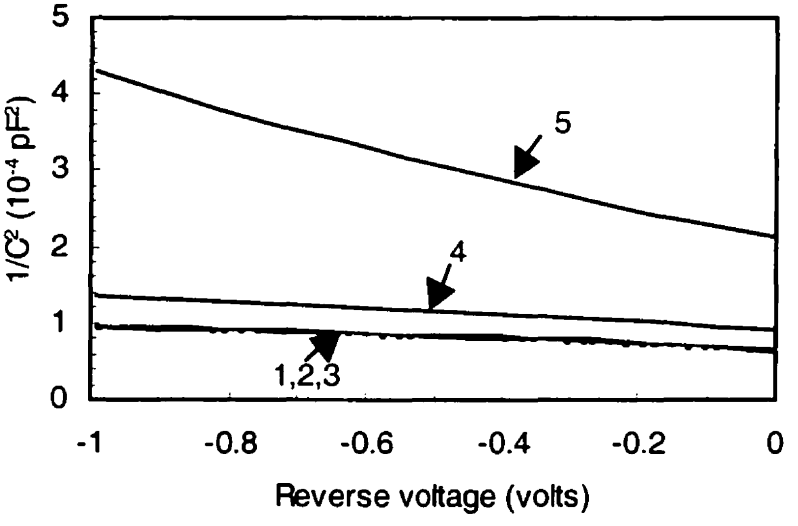

Figure 4.7. Results of *C-V* measurements of sample LS1D-L at 100 kHz at room temperature. (1) After In diffusion for 3 minutes at 200 °C, (2) after treating for 5 minutes at 100 °C, (3) after wire bonding, (4) after etching of the exposed In, (5) after rinsing with ammonia.

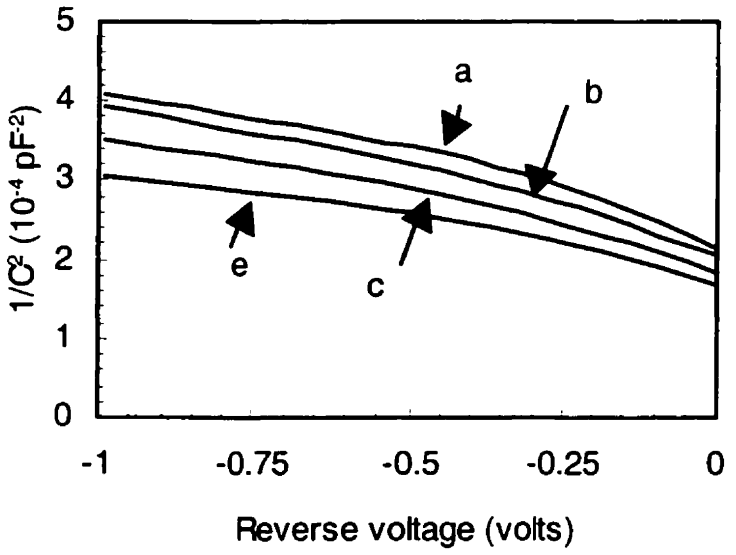

Figure 4.8. Results of *C-V* measurements on sample LS35A-j. (a) After In evaporation, (b) after wire bonding, (c) after etching of the exposed In, (e) after rinsing with ammonia. 100 kHz at room temperature.

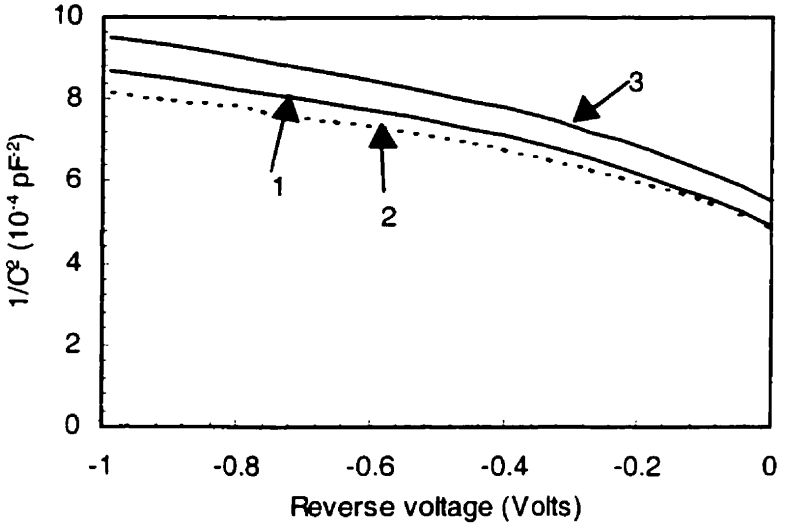

Figure 4.9. Results of *C-V* measurements on sample 84HSF65-d. (1) After In diffusion for 4 minutes at 200 °C and treating for 10 minutes at 100 °C, (2) after wire bonding, (3) after etching of the exposed In.

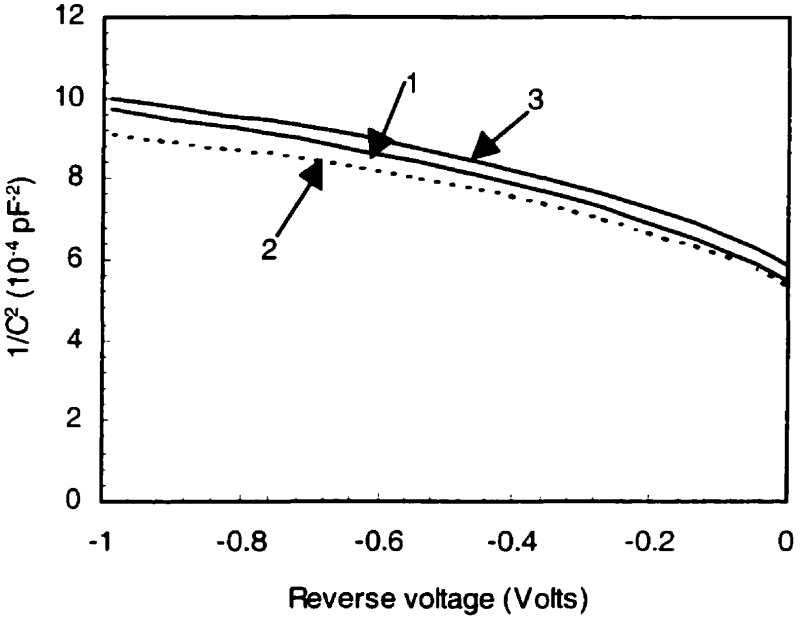

Figure 4.10. Results of *C-V* measurements on sample 84HSF65-L. (1) After In diffusion for 4 minutes at 200 °C and treating for 10 minutes at 100 °C, (2) after wire bonding, (3) after etching of the exposed In.

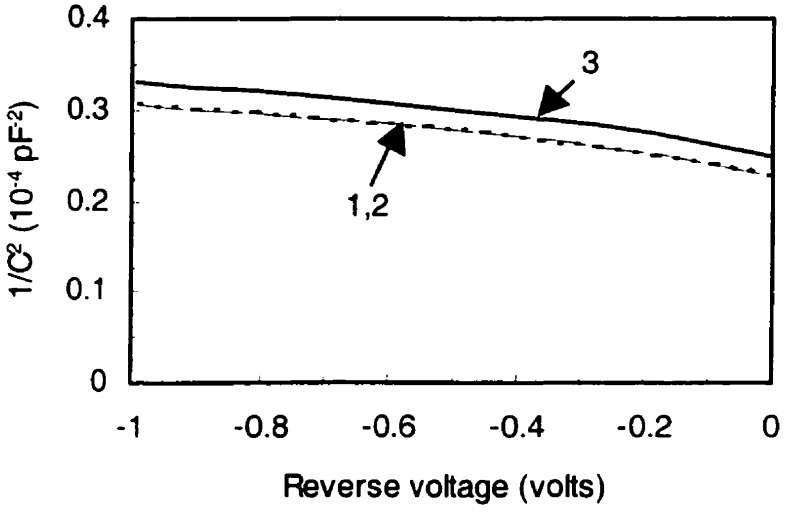

Figure 4.11. Results of *C-V* measurements on sample LS1E-a. (1) After In diffusion for 1.5 minutes at 200 °C and treating for 10 minutes at 100 °C, (2) after wire bonding, (3) after etching of the exposed In. 100 kHz at room temperature.

Chapter 5

Minority Carrier Diffusion Length Measurements

The studies of minority carrier diffusion length in $CuInSe_2$ is important because it could lead to further understanding and improvement of $CuInSe_2$ photodetectors. Furthermore, the knowledge of the diffusion length is required in determining the quantum efficiency of $CuInSe_2$ homojunctions. There are several methods for measuring minority carrier diffusion length in a semiconductor. Some of them involve the use of sophisticated equipment, such as electron beam systems, while others involve the optical and electrical measurements of heterojunctions or Schottky junctions.

The photocurrent-capacitance (PC) method is a method based on the variation of depletion capacitance and illuminated-to-dark current change with reverse bias. This method was originally described by Tyagai [5.1]. It has also been used by Smith and Abbot in GaP Schottky junction cells [5.2], by Young and Rowland in GaAs cells [5.3], by Qiu and Shih in polycrystalline thin film $CuInSe_2$ heterojunctions [5.4], Lastras-Martinez et al for CdTe [5.5], and by Champness, Shukri, and Chan in $CuInSe_2$/CdO heterojunction cells [5.6, 5,7]. Using a photocurrent-capacitance method on their $CuInSe_2$/CdO cells, Dr. Champness et al. found the diffusion length values are different between the devices made with cleaved $CuInSe_2$ surfaces and abrasively polished ones.
In the present work, the photocurrent-capacitance measurements were carried out on the homojunctions and the results obtained are described in this chapter.

5.1 Principle of photocurrent-capacitance method (PC)

The main physical mechanisms involved in junction photodetection are illustrated in Figure 5.1. At point A, an incoming photon is absorbed in the n^+ side to create an electron and a hole. If this takes place within a diffusion length (the distance in which excess minority carrier concentration is reduced to e^{-1} of its peak value, or in physical terms, the average distance a minority carrier traverses before recombining with a carrier

of the opposite type) of the depletion layer, the hole will, with high probability, reach the layer boundary and will drift under the field cross it. A hole traversing the junction contributes a charge e to the current flow in the external circuit. If the photon is absorbed near the p side of the depletion layer, as shown in C, the resulting electron will diffuse to the junction and then drift across it, giving rise to a flow of charge e in the external load. The photon may also be absorbed in the depletion layer at B, in which case both the hole and electron created drift (in opposite directions) under the field until they reach the p and n^+ sides, respectively. In this case, since each carrier traverses a distance that is less than the full junction width, the contribution of this process to charge flow in the external circuit is $2e$. In practice this last process is the most desirable for real use of photodetectors, since each absorption gives rise to a charge of $2e$, and the delay in current response caused by finite diffusion time is minimized.

It is clear from Figure 5.1 that a photodiode is capable of detecting only photons with energy $h\nu \geq E_g$, where E_g is the energy gap of the semiconductor. If $h\nu >> E_g$, the absorption, which increases strongly with frequency, will take place entirely near the surface of the junction (in the n^+ region of Figure 5.1) and the minority carriers generated by the absorbed photons will recombine with majority carriers before diffusing to the depletion layer. This event does not contribute to the current flow and, as far as the signal is concerned, is wasted.

Based on the above comments, the basis of the PC method is described as follows. Consider an n^+-p photodiode, where the thickness of the p-type layer is large compared with the electron diffusion length, L_n and the n^+ layer is sufficiently thin so that it is transparent to the optical beam used (See Figure 2.2). Suppose the photodiode is illuminated with a photon flux F at a wavelength λ for which the absorption coefficient in the semiconductor is α. Then, the photogenerated current I_{ph} is given by:

$$I_{ph} = qFT_r(1-R)A\int_0^{W+L_n} e^{-\alpha x}\alpha dx = qFT_r(1-R)A\left[1-e^{-\alpha(W+L_n)}\right] \qquad (5.1)$$

Where R is the reflectance of the surface of photodiode. T_r is its optical transmission coefficient, W is the width of the depletion layer, A is the area of the cell, and q is the electronic charge.

If λ is chosen near the bandgap, so that α is small to satisfy $\alpha(W+L_n) << 1$ and corresponds to light penetrating almost completely through the depletion layer, then Equation (5.1) becomes:

$$I_{ph} = qFT_r(1-R)A[1-1+\alpha(W+L_n)] = qFT_r(1-R)A\alpha(W+L_n) \qquad (5.2)$$

When a reverse voltage $V_R >> kT/q$ is applied to the photodiode terminals (where k is Boltzmann's constant and T is absolute temperature), the diode reverse dark current is equal to $I_R(e^{\frac{qV_R}{kT}} - 1) \approx -I_R$. Then the current I is given by: $I = I_{ph} + I_R$. Hence, the difference between I and I_R is $\Delta I = I - I_R = I_{ph}$, and the Equation (5.2) becomes:

$$\Delta I = qFT_r(1-R)A\alpha(L_n + W) = K(L_n + W) \qquad (5.3)$$

where

$$K = qFT_r(1-R)A\alpha$$

If we know the relationship between ΔI and W, then we can obtain the value of L_n. The depletion capacitance C of the junction is given by:

$$C = \frac{\varepsilon_0 \varepsilon_r A}{W} \qquad (5.4)$$

where ε_r is the relative dielectric constant of the semiconductor and ε_0 is the permittivity of vacuum. Substitution Eq. (5.4) into Eq. (5.3) yields:

$$\Delta I = K'\left(\frac{1}{C} + \frac{L_n}{\varepsilon_0 \varepsilon_r A}\right) \qquad (5.5)$$

where $K' = K\varepsilon_0\varepsilon_r A$.

According to Eq. (5.5), when the reverse bias is varied, a plot of I_{ph} against $1/C$ should yield a straight line, with an extrapolation intercepting on the $1/C$ axis at $-L_n/(\varepsilon_0 KA)$. From the intercept, the diffusion length L_n can be determined. Here, the constant K, involving α, is independent of the reverse voltage.

Linearity would not be expected at low reverse and forward bias because of the condition $V_R >> kT/q$ is not satisfied.

5.2 Experimental setup

For the diffusion-length measurements, the capacitance was measured at a frequency of 100 kHz using an Hewlett Packard model 4274A multi-frequency LCR meter. The experimental set-up is shown in Fig. 5.2. During the measurements, a tungsten filament lamp source and a monochromator (with the slit width kept at 0.6 mm) were used to illuminate the diode with the steady monochromatic light. The applied reverse voltage V_R from the LCR meter was varied from –0.01 to –0.9 volt. Reverse bias voltages with a magnitude greater than 1 volt were not applied due to junction break down. The illuminated-to-dark current difference ΔI was measured over the same bias range at the same wavelength by applying chopped light from the monochromator (see Figure 5.3). The current change ΔI was measured from the voltage change across a 220 Ω resistor connected in series with the sample. This voltage signal was measured with a Princeton Applied Research model 124A lock-in amplifier with a reference voltage obtained from the light chopper (Stanford Research Systems, Inc. model SR 540), whose chopping frequency was set at 163 s^{-1}. The voltage drop across the 220 Ω sensing resistor was about 10^{-3} V and thus was negligible compared with the bias voltage applied to the sample.

5.3 Experimental results

The diffusion length of the electrons in the $CuInSe_2$ junction on monocrystalline substrate was estimated from the photocurrent-capacitance method. The method basically consisted of two steps. First, the illuminated-to-dark change in the short circuit current (ΔI) of the cell was measured at different reverse bias voltages with the illumination of long wavelength light. Second, values of the junction parallel capacitance, C_p, at the same reverse bias voltages and illumination were measured.

Figures 5.4, 5.5, and 5.6 give experimental results for the sample No. LS1D-1, 84HSF65-1, and 84HSF65-3, respectively. Based on Equation (5.5), the electron diffusion lengths were obtained and are shown in Table 5.1.

An example of calculation of L_n is given as follows: Capacitance values were first obtained by *C-V* measurements. The illuminated-to-dark current change ΔI_{ph} was then

calculated by subtracting dark current I_D from illuminated current I_{ph}. Figure 5.5 shows a plot of the illuminated-to-dark current change ΔI_{ph} versus $1/C$ at different wavelengths with the capacitance measured at a frequency of 100 kHz for the sample No. 84HSF65-1. At a wavelength of 1.3 μm, the intercept on the $1/C$ axis is: $1/C = -0.0145$ (pF^{-1})

According to the Eq. (5.5), $\Delta I_{ph} = 0.1/C = -L_n/\varepsilon_r\varepsilon_0 A$. Therefore, $L_n = 0.0145\times\varepsilon_r\varepsilon_0 A$ $=0.0145$ (pF^{-1}) $\times 10\times 8.85\times 10^{-14}$ (F/cm) $\times 0.785$ (mm^2) $\approx$ 1.01 (μm). where ε_0 is the permittivity of free space, $\varepsilon_0 = 8.85\times 10^{-14}$ (F/cm). ε_r is the dielectric constant of $CuInSe_2$, ($\varepsilon_r \approx 10$). A is the junction area, $A \approx 0.785$ (mm^2).

5.4 Conclusions

In Table 5.1, diffusion lengths obtained at different wavelengths are shown. From Figures 5.4, 5.5, and 5.6, we can see that at wavelengths of 1.1 μm, 1.15 μm, and 1.2 μm, intercepts on $1/C$ axis are positive. Thus, the diffusion lengths can not be calculated. As described in section 5.2, $CuInSe_2$ has high absorption coefficients for short wavelength light (high photon energy). Thus, most of carriers induced are within the n^+ region and the depletion region. In the neutral p region, no carriers are generated. Hence, when the reverse bias is changed, no minority electrons produced by photon in the neutral p region can diffuse to the depletion layer and contribute to the photocurrent. Under such conditions, the photocurrent is not linear function of $1/C$. Thus, when we use linear relation to fit the data, intercepts on $1/C$ become positive. The calculation of L_n becomes negative and is incorrect.

Even at long wavelengths, the diffusion length measurements also show some tolerance. If we consider the absorption in the n^+ side, then it can be shown that $\Delta I_p = K(W + L_n + L_p)$. Using this equation, we can get the sum of the diffusion lengths of the minority carriers in the depletion regions of the junction.

As $CuInSe_2$ has large absorption coefficient α at short wavelengths, we can only apply long wavelength (photon energy is near or above the bandgap of $CuInSe_2$) to carry at the measurements.

Generally, the doping concentration can affect the diffusion length. It is noted that the diffusion length is given by the equation:

$$L_n = \sqrt{\mu_n \frac{kT}{q} \tau_n} \qquad (5.6)$$

Where μ_n is the minority carrier mobility, τ_n is the minority carrier lifetime, kT/q is the thermal voltage at a given temperature T. The mobility is a measure of the ease of carrier motion within a semiconductor crystal. The carrier mobility varies inversely with the amount of scattering which is taking place within the semiconductor. Scattering mechanisms include two components: lattice scattering and ionized impurity scattering.

According to the Eq. (5.6), the decrease of μ_n will cause a decrease of L_n. Therefore, an increase of the doping concentration will result in a decrease in the diffusion length. From Table 5.1 and Table 2.2, the doping concentration of sample No. LS1 is in the order of 1.1×10^{17} cm^{-3} and the mobility is 35 $cm^2/V\text{-}s$. While the doping concentration of sample No. 84HSF65 is $1.7\times 10^{17}cm^{-3}$. The mobility of sample No. 84HSF65 is 25 $cm^2/V\text{-}s$.

In conclusion, the diffusion length in p-type $CuInSe_2$ has been measured using the photocurrent-capacitance method. Some of the assumptions made in the calculation of the minority carrier diffusion length may have affected the calculated values. For instance, the thickness of the n^+ side of $CuInSe_2$ was not known and the absorption coefficient in the n^+-side was also not known. Because of this, a portion of the incident photons may have been collected in the n^+ side. Furthermore, the ideal diode assumption may have caused additional errors in the minority carrier diffusion length determination for the present $CuInSe_2$ homojunction photodiodes, where n-factors were greater than 1.

The other source of errors is the capacitance measurements. As the capacitance was taken under a small ac signal, while the photocurrent measurements were taken under the dc reverse bias with the sample being shunted by a monochromatic light. The measured ac capacitance and dc capacitance are different. So for the samples studied by the capacitance method, some tolerance is expected in the diffusion length values.

Table 5.1 Results from the photocurrent-capacitance measurements.

Wavelenth (μm)	LS1D-I (L_n μm)	84HSF65-d(L_n μm)	84HSF65-l (L_n μm)
1.1	Negative	Negative	Negative
1.15	Negative	Negative	Negative
1.2	Negative	0.53	Negative
1.25	0.41	0.72	0.68
1.3	0.62	1.01	0.96

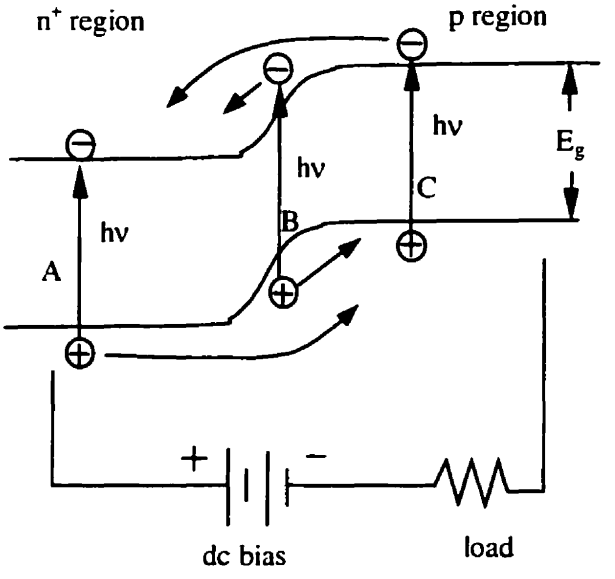

Figure 5.1 Three types of electron-hole pair generation by photons that contribute to the current flow in n^+-p photodiode.

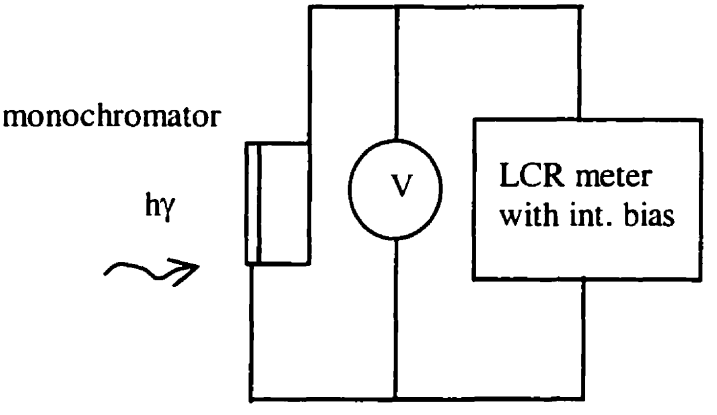

Figure 5.2 A schematic diagram of the experimental set-up for the measurements of capacitance in the photocurrent-capacitance method.

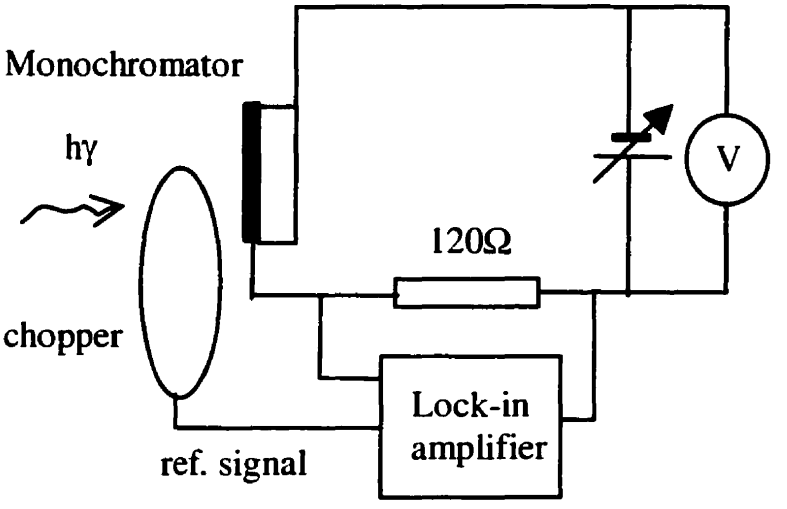

Figure 5.3 A schematic diagram of the experimental set-up for the measurements of the illuminated-to-dark current change, ΔI, in the photocurrent-capacitance method.

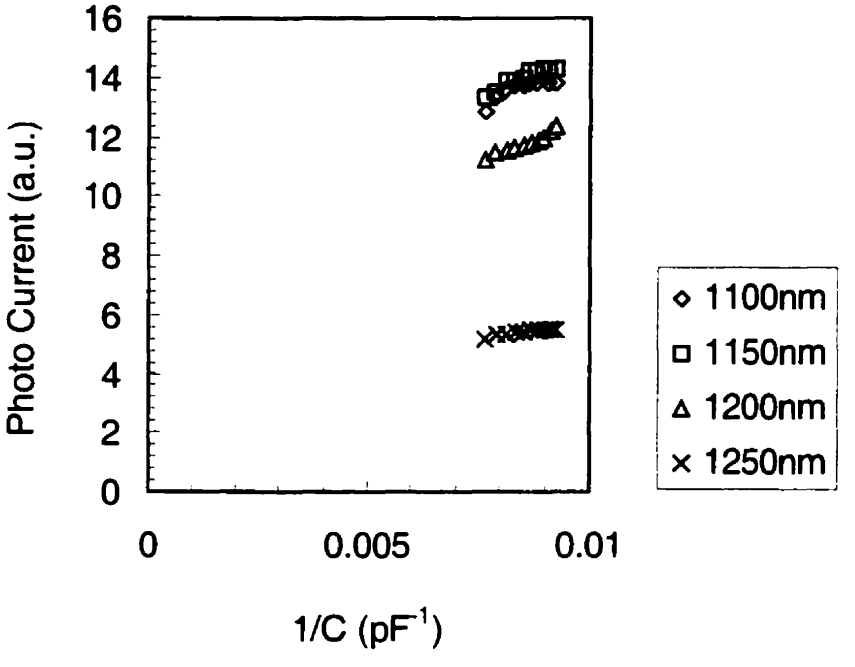

Figure 5.4. Plots of ΔI against $1/C$ for sample No. LS1d-i.

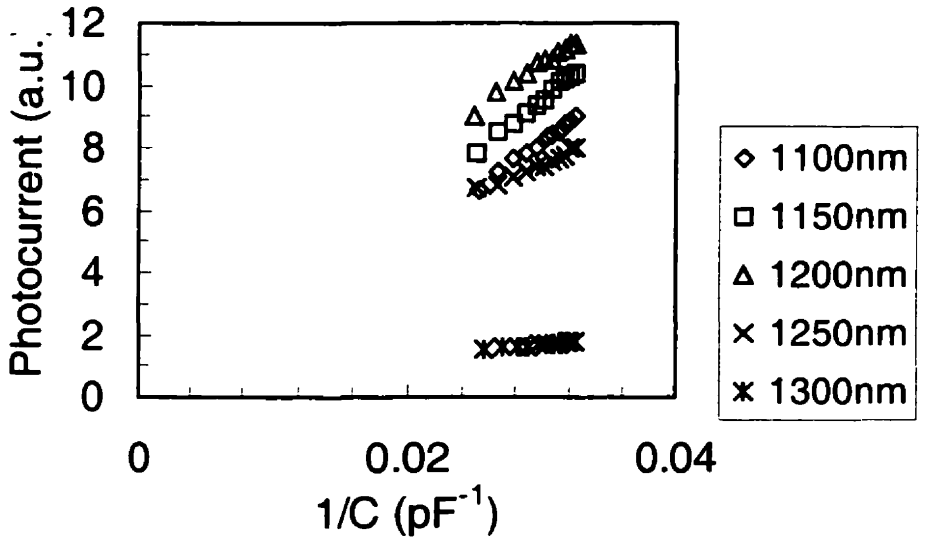

Figure 5.5. Plots of ΔI against $1/C$ for the sample No. 84HSF65-d.

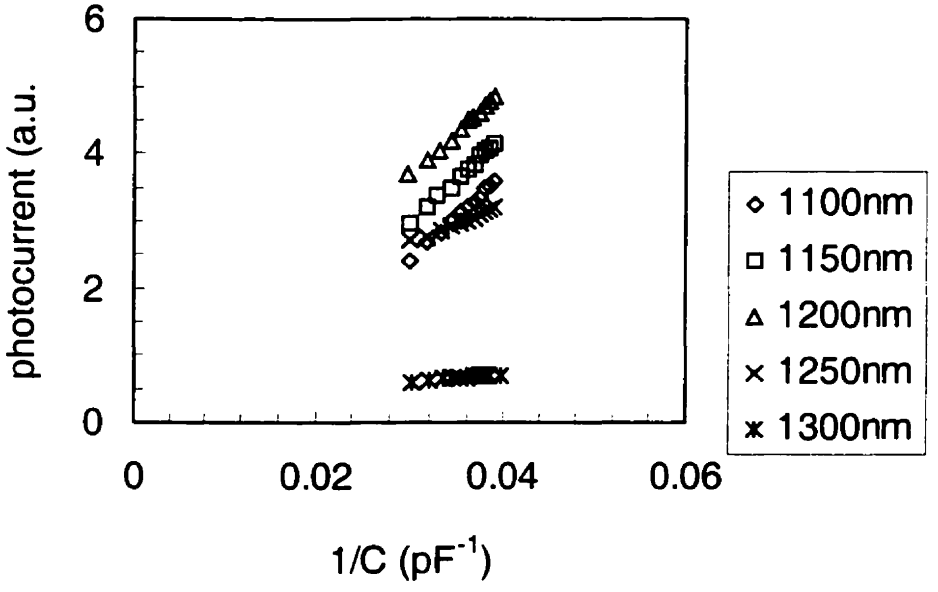

Figure 5.6. Plots of ΔI against $1/C$ for the sample No. 84HSF65-l.

Chapter 6

Quantum Efficiency and Photoresponse Measurements

6.1 Quantum efficiency measurements

The quantum efficiency, η, is the number of electron-hole pairs generated per incident photon and is given by:

$$\eta = \frac{I_p / q}{P_{opt} / h\nu}. \qquad (6.1)$$

Here, I_p is the current generated by the absorption of photons. P_{opt} is the optical power at a wavelength λ. $h\nu$ is the photon energy and q is the electronic charge (q=1.6×10^{-19} C). It is noted that the photon energy is given by

$$h\nu = \frac{hc}{\lambda} \qquad (6.2)$$

where h is Planck's constant (h=6.63×10^{-34} J/s), c is the speed of light in vacuum (c=3×10^{8} m/s) and λ is the wavelength.

A related figure of merit is the responsivity, R, which is the ratio of the photocurrent to the optical power:

$$R = \frac{I_p}{P_{opt}} = \frac{\eta\lambda(\mu m)}{hc}(A/W) \qquad (6.3)$$

To measure the value of quantum efficiency, a silicon (Si) detector with known responsity from 500 nm to 1100 nm and an InGaAs detector from 1100 to 1400 nm were firstly used to calibrate the light source. The Si (or InGaAs) detector was illuminated with monochromatic light supplied by a Beckman Model DU spectrophotometer where the exit slit was set at 0.6 mm. The incident light beam was chopped at a frequency of about 163 Hz using a light chopper (Standford Research Systems, Inc. model SR 540). The experimental setup is shown in Figure 6.1. The photogenerated current of Si (and InGaAs) detector was measured and the incident optical power P_{opt} for the different wavelengths was calculated using Eq. (6.3). The Si detector was the replaced by an n^{+}-p

In-diffusion $CuInSe_2$ photodetector and the photocurrent measurement repeated. The quantum efficiency of the $CuInSe_2$ photodetector was finally calculated using Eq. (6.1) and the incident optical power P_{opt} values obtained in the previous step.

Figure 6.2 shows the quantum efficiency of five samples with different indium diffusion times at 200°C. Table 6.1 gives the maximum quantum efficiency of these samples. For the sample with diffusion times from 4 to 5 minutes, the maximum quantum efficiency was obtained from the devices.

From Figure 6.2, we can see that the quantum efficiency decreases drastically beyond the maximum towards the long wavelength side. Conversely, it shows a gradual decrease towards shorter wavelengths. The quantum efficiency is a function of wavelength to the extent that the Fresnel reflectance and absorption coefficient are related to the wavelength of the radiation. The Fresnel reflectance, which varies because the index of refraction is a function of wavelength, usually affects short-wavelength response. At the same time, α is a strong function of the wavelength for a given semiconductor. Hence, the wavelength range in which appreciable photocurrents can be generated is limited. The short wavelength cutoff of the photoresponse appears because the values of α at short wavelengths are very large, and the photons are absorbed very near to the surface where the recombination time is short. The photocarriers thus can recombine before being collected in the p-n junction. The long-wavelength cutoff λ_c is determined by the energy gap of the semiconductor. At wavelengths longer than λ_c, most of the photons penetrate the detector material and are not absorbed.

6.2 Operation modes of p-n photodiode

A photodiode can be operated in different modes. Figure 6-3 (a) shows the family of *I-V* curves at different operation modes [6.1]. Each curve gives the current through the device as a function of the voltage, for a specific value of light intensity *P*. Quite a lot of information can be gained from studying such a set of curves.

When *V*, the voltage applied across the device, is positive, current flows in the "forward-biased" direction. It is difficult to distinguish the current levels different light illuminations. When a negative voltage is applied, the current is almost constant with the variation of voltage for a given light level until the breakdown voltage V_{br} is approached.

As the reverse voltage across the device approaches V_{br}, an avalanche process called impact ionization begins.

The curve without of light ($P = 0$) is the familiar semiconductor-diode curve in which the resistance in the forward bias is small and that in the reverse bias is large but not infinite. The small current that flows under the reverse-biased conditions, even for zero light level, is called the dark current I_{dk}, and represents a source of unwanted noise. The dark current is due to thermal generation of carriers. When the temperature is increased, more electrons are excited, leading to an increase in current and dark noise.

Conceivably, it would be possible to operate the photodiode in any one of the three quadrants covered by the curves. One can employ the photovoltaic mode by connecting the photodiode across the high-impedance input terminals of a voltage amplifier, so as to amplify V_{ph}, as shown in Figure 6-3 (b). The value of load resistor for this mode might be many megohms. Since the curves are very close together, it is clear that this is not a very effective way of using the photodiode.

Another possibility is to operate the photodiode in short-circuit mode and use a current amplifier, maintaining the voltage across the device near zero so that the current amplifier sees a light-dependent current. This mode is shown in Figure 6-3 (c). There are several problems with this mode. For one thing, since the depletion region is very shallow, the quantum efficiency will suffer, and for another, a strong potential difference across the depletion region is required in order to minimize the response time of the device by accelerating the carriers.

Therefore, photodiodes for fiber optic communication use neither of these modes, but instead use the lower left quadrant, i.e., reverse biasing, as shown in Figure 6.3 (d), and (e). Figure 6.3 (d) represents the PN or PIN diode operated with a voltage amplifier, and Fig. 6-3 (e) shows the operation of an APD.

6.3 Frequency response measurements

6.3.1 Pulse response theory

Let us consider the pulse response theory for an optical detector [6.2]. At the input end of some optical system we have a signal where the optical power is modulated at a frequency f. This is $P_{in} = P_0^i[1-\cos(2\pi ft)]$. If we express the optical power output of the

system as $P_{out} = P_0^o[1-\cos(2\pi ft+\phi)]$, the ratio of P_0^o to P_0^i gives the system response, which is denoted by *H(f)*. We define the optical bandwidth of the system as the frequency range Δf_{opt} over which $|H(f)|$ exceeds one half of its maximum value. If we allow the optical output signal to fall onto a "perfect" photodetector, then the current output, i_d, would follow the variations in *H(f)*. Electrical power from the detector, being proportional to i_d^2, will follow $|H(f)|^2$. In an electrical system, the electrical bandwidth is defined as the frequency range over which the electrical power exceeds one half of its maximum value. We can therefore define an electrical bandwidth for our optical system, Δf_{el}, as the frequency range over which $|H(f)|$ exceeds $\sqrt{\frac{1}{2}}$ of its maximum value. Similar arguments apply when a voltage output is obtained.

We turn now to pulse broadening. Suppose we launch an optical pulse which, as far as the system response is concerned, is infinitesimally narrow. When the pulse emerges from the system, it will have broadened into a definite shape. This shape may be described by the normallized impulse response *h(t)*. The function *h(t)* is normallized so that:

$$\int_{-\infty}^{+\infty} h(t)dt = 1 \quad (6.3)$$

The functions *h(t)* and *H(f)* are in fact related by a Fourier transform,

$$H(f) = \int_{-\infty}^{+\infty} h(t)\exp(-i2\pi ft)dt \quad (6.4)$$

A useful parameter for characterizing the spread of a pulse is the r.m.s. pulse width. This is given by σ where:

$$\sigma^2 = \int_{-\infty}^{+\infty} t^2 h(t)dt - \int_{-\infty}^{+\infty} th(t)dt \quad (6.5)$$

If the response of the photodetector is that of exponential function of time (Figure 6.4), we have

$$h(t) = \frac{1}{\tau}\exp\left(-\frac{t}{\tau}\right), \qquad t>0 \qquad (6.6a)$$

$$h(t) = 0, \qquad t<0 \qquad (6.6b)$$

where τ is the Full-Width-at-Half-Maximum (FWHM). Thus

$$H(f) = \frac{1}{\tau}\int_{-\infty}^{+\infty} \exp\left(-\frac{t}{\tau}\right)\exp(-i2\pi ft)dt = \frac{1}{\tau}\int_{-\infty}^{+\infty} \exp\left[-t\left(\frac{1}{\tau} + i2\pi f\right)\right]dt = \frac{1}{1+i2\pi f\tau} \qquad (6.7)$$

hence

$$|H(f)| = \frac{1}{(1+4\pi^2 f^2\tau^2)^{1/2}} \qquad (6.8)$$

and

$$\Delta f_{opt} = 0.276/\tau \qquad (6.9)$$

$$\Delta f_{el} = 0.159/\tau \qquad (6.10)$$

6.3.2 Photodiode bandwidth measurements

In this section, we shall discuss the possible electrical circuits and use pulse response theory described in the above section to estimate the photodetector bandwidth [6.3]. In order to increase the photodiode response speed, the photodiode is operated at reverse bias. Three types of circuits may be used to measure the photodiode bandwidth.

Resistor terminated

Many of the earliest photodiodes used a simple resistor terminated design [6.4] shown in Fig. 6.5. In this case, the bandwidth is determined by the *RC* time constant of the input, where *R* is the biasing resistance and *C* is the photodetector. Thus, for small values of *R*, the bandwidth can be quite large, but at the expense of signal magnitude. Further, the small biasing resistor dominates the input noise, leading to poor receiver sensitivity. This configuration only requires a resistor and has been demonstrated to operate at low gigahertz frequencies. In our resistor terminated circuit, as shown in Figure 6.5, a resistor with $R = 220\ \Omega$ is used.

For those low output photodetectors with low quantum efficiency, a high frequency transistor amplifier and monolithic IC amplifier must be used.

High frequency transistor amplifier [6.5]

Utilizing an RF small signal silicon bipolar transistor MPS918 (bandwidth 600 MHz), a one-stage common-emitter circuit was designed. Based on the transistor input and output characteristics (measured with HP model 4145A semiconductor analyzer), we select suitable resistors and capacitors. The circuit constructed is shown in Figure 6.7. Figure 6.6 shows the measured detector output waveform with an HP model 54502A 400 MHz digitizing oscilloscope. Except for the circuit using the transistors, a high speed integrated amplifier described in the next section is also needed to measure the photodetector bandwidth.

High speed integrated amplifier

A high speed bipolar model AD844 monolithic operational amplifier was selected. The AD844 IC combines high bandwidth and very fast large signal response with excellent dc performance.

The AD844 IC can be used in place of traditional operational amps, but its current feedback architecture results in much better ac performance, high linearity and an exceptionally clean pulse response. The circuit is shown in Figure 6.8.

To carry out optical measurements on the $CuInSe_2$ photodiodes, a spark source was employed as the light input. The signal generator generates a 5 volts TTL trigger signal to the spark source. The spark light is allowed to pass through one focus lens to increase the light intensity and shine on the photodetector. The normal pulse width of the spark source is 15 ns. Results from a typical $CuInSe_2$ detector response are shown in Figure 6.6. From the Figure 6.6, we can see that the response rise time is short, but response decay time is long. Hence, the decay time is the main limit for the present detector bandwidth. The rise time arises from the drift time of photo induced carriers across the depletion region. The decay time arises from the un-equilibrium carriers diffusion time. So the rise time is much shorter than the decay time. All of the $CuInSe_2$ detector decay response times were found to be about 15 μs to 20 μs. So that the input optical source can be taken as a δ source. Based on the pulse response theory described in section 6.3.1, we measured the Full-Width-at-Half-Maximum (FWHM) τ. The results

obtained are shown in Table 6.2. By substituting the values in Table 6.2 into equation (6.10), the bandwidth of the photodetectors obtained was from 8 kHz to 10 kHz.

6.4 Detectors noise

We have seen in the chapter 2, section 2.1.4, that when light falls on a photodetector, electron-hole pairs are generated, giving to an electrical current. The conversion process from light to electrical current is accompanied by a noise. The two most important noise mechanisms in a photodetector circuit are the quantum noise (or shot noise) and thermal noise.

Based on the Equation (2.21), the mean square shot noise current is given by

$$\overline{i_{NS}^2} = 2q(I + I_d)\Delta f \qquad (6.11)$$

Where q is the electron charge, I is the photo current. I_d is the dark current and Δf is the bandwidth over which the noise is being considered. Since I itself depends on the incident optical power, the shot noise increases with an increase in incident optical power.

Another noise is thermal noise (also referred to as Johnson noise or Nyquist noise) from the load resistor of the photodiode circuit due to random thermal motion of electrons. This thermal noise superimpose on the signal current generated by the photodetector. The mean square thermal noise current in a load resistor R_{eq} is given by

$$\overline{i_{NS}^2} = \frac{4k_B T\Delta f}{R_{eq}} \qquad (6.12)$$

where $k_B = 1.38 \times 10^{-23}$ J/K is the Boltzmann constant, T is the absolute temperature, and Δf is the bandwidth of detection.

Note that the thermal noise is independent of the incident optical power. Furthermore, values of R_{eq} cannot be increased indefinitely since the detector bandwidth is determined by R_{eq}.

Using the data in Table 3.1 and Table 3.2, we can obtain the values of dark current I_d of the detectors at reverse voltage 0.5 volts, the series resistance and parallel resistance. Using the experimental setup shown in Figure 5.3, we can get the detector

photocurrent I. Note that the photodetector load resistance is 120 ohms and the bandwidth has been measured in the last section (see Table 6.2). Based on equations (6.11) and (6.12), we can calculate the quantum noise and thermal noise of the detectors. The rms quantum noise current and the rms thermal noise current are shown in Table 6.3.

Comparing the thermal noise with quantum noise, we find that former is dominated in the present devices.

6.5 Conclusions

By selecting a suitable diffusion time for In, we can get an appropriate junction depth in $CuInSe_2$, which can be optimized for the detector to obtain high quantum efficiency. The gradual decrease of quantum efficiency towards shorter wavelengths is partly due to the increase in optical absorption within the illuminated surface and the active region and partly to the increased carrier loss caused by the surface (or the interface recombination). The rapid decrease with the increase of the wavelength is due to the band-gap energy of the active region.

As described in Chapter 2, there are three main mechanisms which limit the frequency response in photodiodes:

1. The finite diffusion time of carriers produced in the p and n regions.
2. The shunting effect of the signal current by the junction capacitance C_d. This places an upper limit of

$$\omega_m \propto \frac{1}{R_e C_d}$$

on the intensity modulation frequency where R_e is the equivalent resistance in parallel with the capacitance C_d.

3. The finite transit time of the carriers drifting across the depletion layer.

The response bandwidths obtained using the above procedure for our photodetectors were about 8 kHz to 10 kHz. The series resistances of the detectors were less than two hundreds ohms and the load resistance was 220 ohms. Hence, the total resistance was less than 500 ohms. The capacitance of the detector was from 50 pF to 100 pF (under reverse bias). Therefore, the RC time constant is about $\sim 10^{-7}$second, which is not the main factor limiting for the operation of the present photodiodes.

We often consider the transient time of the carrier across the depletion layer. Based on Equation (4.7), the depletion layer width is from 0.3 μm to 0.8 μm. For a 15 μs to 20 μs transient time, the carrier drift velocity under a reverse bias of 0.5 volt is only about 1 cm/sec. This is unlikely to be a reasonable result. So we believe that the carrier diffusion time in the p and n region limits our photodetector response. Since a decrease in the lifetime of the carriers can increase the photodetectors response time, the carrier lifetime can be substantially reduced by introducing impurities with deep levels in the forbidden gap.

Table 6.1 Maximum quantum efficiency vs. diffusion time for five $CuInSe_2$ photodiodes.

Sample No.	LS35A-j	LS1A-c	LS1D-l	LS1E-e	84HSF65-g
Diffusion time (minutes)	7	5	3	1.5	4
Maximum quantum efficiency (%)	16	42	40	8.2	61

Table 6.2 Results of bandwidth of $CuInSe_2$ photodetectors.

Sample No.	Response time (FWHM) (μs)	Bandwidth (kHz)
LS1A-a	19.3	8.24
LS1A-b	19.7	8.07
LS1A-c	16.7	9.52
LS1A-d	17.3	9.19
LS1A-e	18.4	8.64
LS1D-d	18.3	8.69
LS1D-e	19.5	8.15
LS1D-f	20.7	7.68
LS1D-h	14.5	10.9
LS1D-l	16.7	9.52
84HSF64-c	14.8	9.46
84HSF64-d	17.8	8.03
84HSF64-e	16.8	10.2
84HSF64-f	19.8	9.7
84HSF64-g	15.6	10.2
84HSF64-h	16.4	9.7
84HSF64-k	17.4	9.14
84HSF64-l	18.6	8.55

Table 6.3 Quantum noise and thermal noise in the $CuInSe_2$ photodetectors.

Sample No.	Quantum noise (10^{-12}A)	Thermal Noise (10^{-10}A)
LS1A-a	1.43	6.82
LS1A-b	2.27	7.01
LS1A-c	3.58	7.17
LS1A-d	3.58	6.99
LS1A-e	3.63	6.98
LS1D-d	2.61	6.4
LS1D-e	2.84	5.91
LS1D-f	2.78	5.94
LS1D-h	2.97	7.26
LS1D-l	2.57	6.84
84HSF64-c	3.81	7.03
84HSF64-d	3.34	6.91
84HSF64-e	3.82	6.78
84HSF64-f	4.48	6.97
84HSF64-g	5.21	7.72
84HSF64-h	5.65	7.56
84HSF64-k	3.43	7.43
84HSF64-l	3.69	7.23

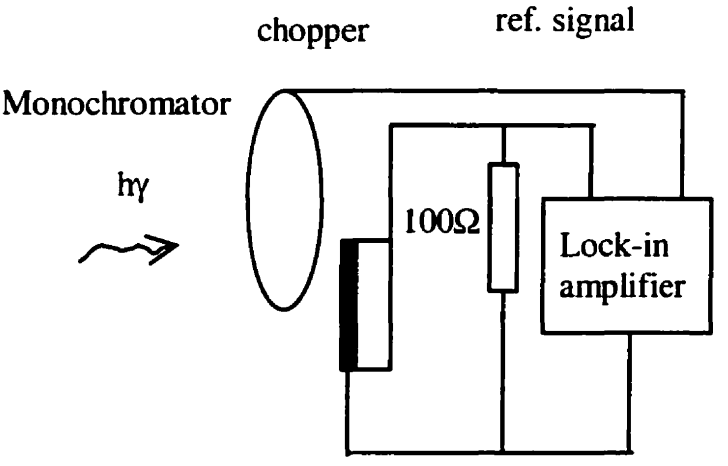

Figure 6.1 A schematic diagram of the experimental set-up used for the quantum efficiency measurements of the photodetectors.

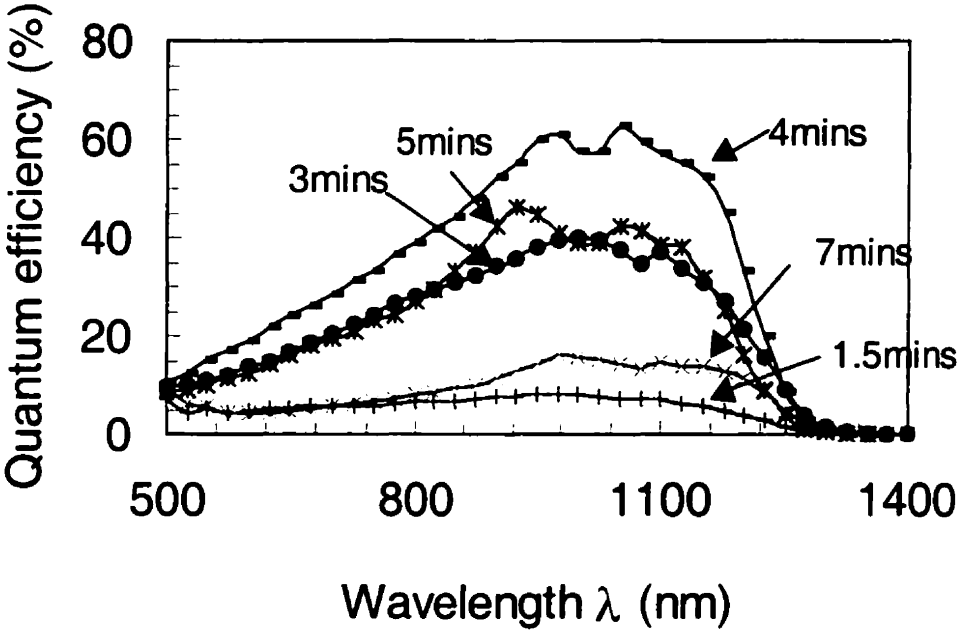

Figure 6.2 Plots of quantum efficiency against wavelength for the five n^+p $CuInSe_2$ photodiodes: LS35A-j (7 minutes), LS1A-c (5 minuts), LSD-j (3 miutes), LS1E-e (1.5 minutes), and 84HSF65-g (4 minutes).

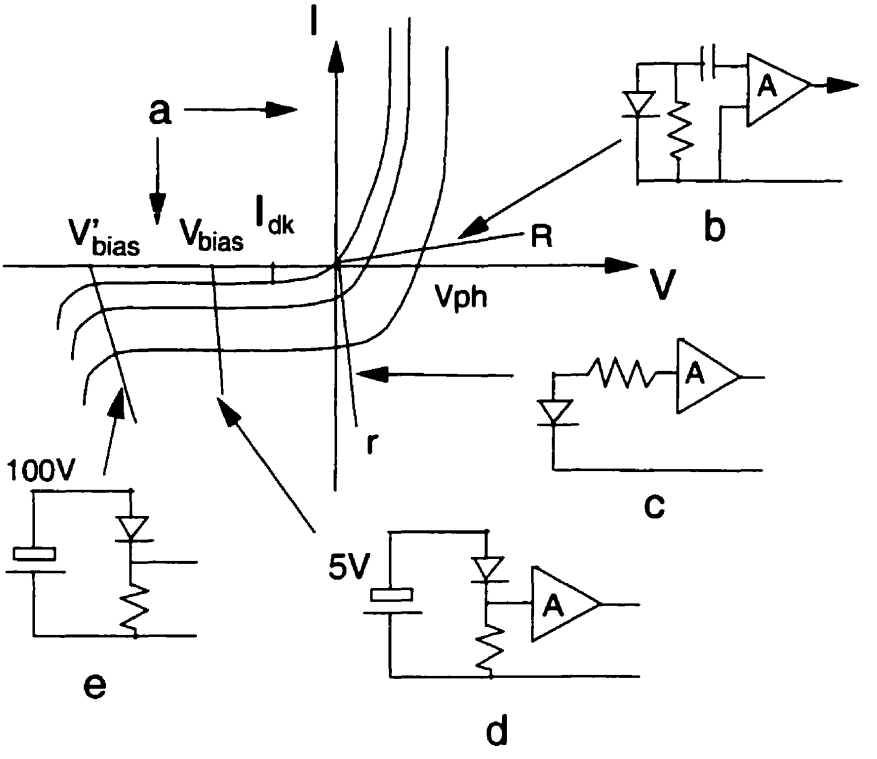

Figure 6.3. Current-voltage curves of a typical photodiode, and the corresponding detector biasing modes. (a) Forward bias is to the right and reverse bias to the left. (b) Operation in open-circuit (photovoltaic) mode. (c) Operation in short-circuit mode. (d) Operation in reverse-bias mode into a voltage amplifier. (e) Operation as an avalanche photodiode.

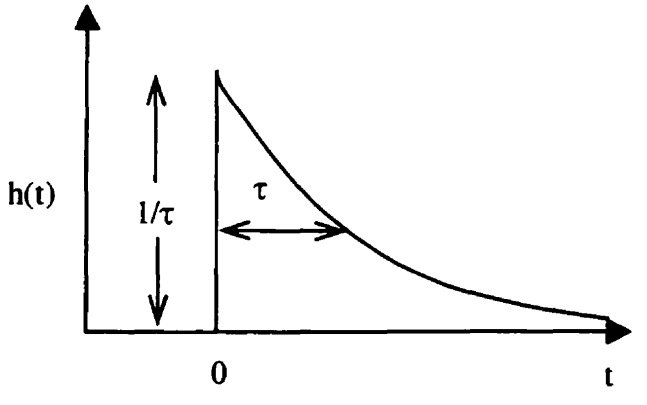

Figure 6.4 The system response function with an exponential decay.

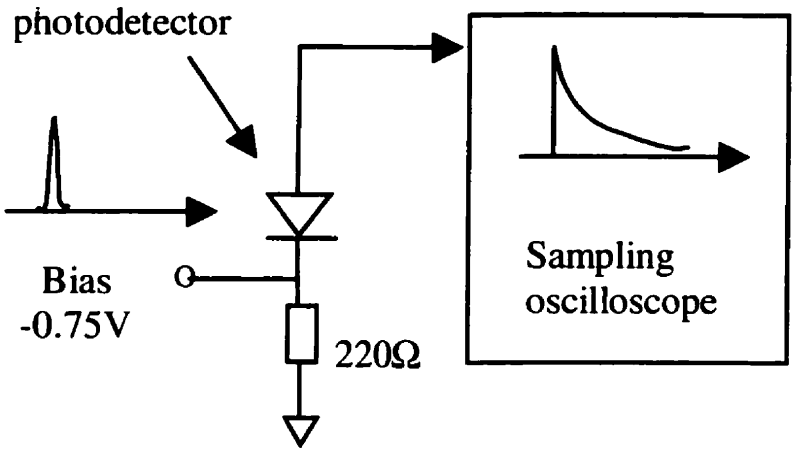

Figure 6.5 $CuInSe_2$ photodetector with a resistive load.

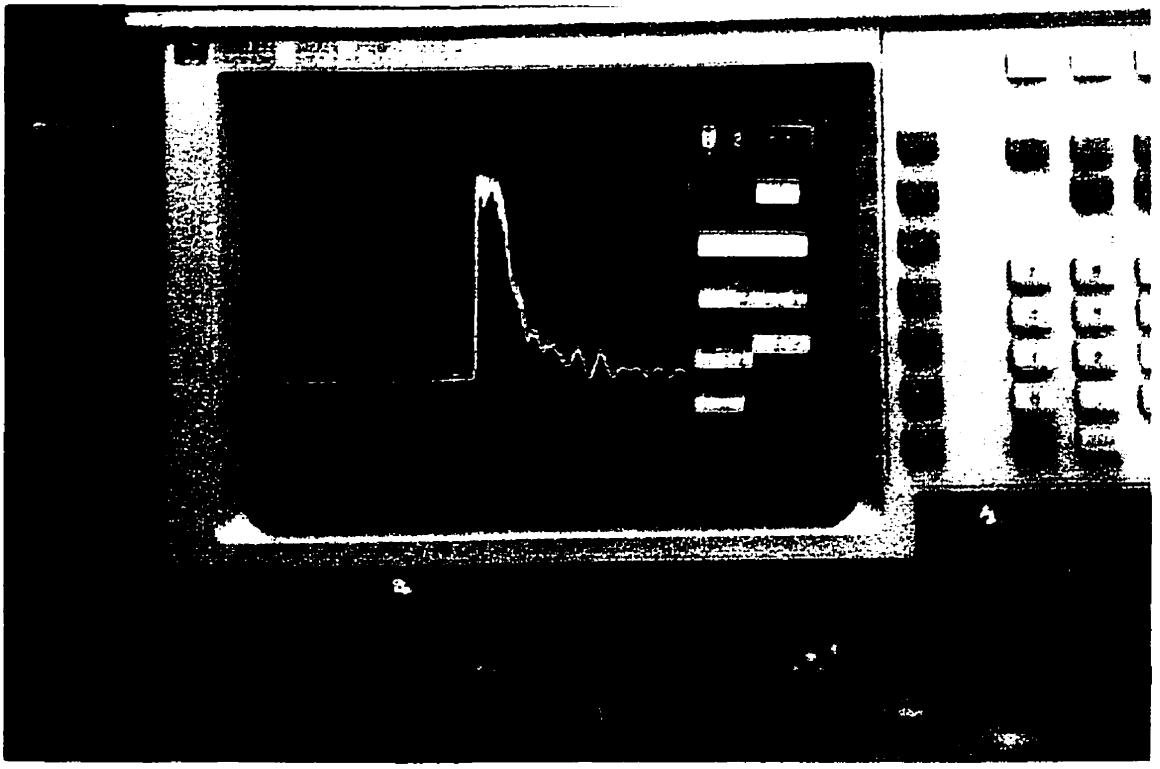

Figure 6.6 The detector output waveform measured with the HP model 54502A 400MHz digitizing oscilloscope

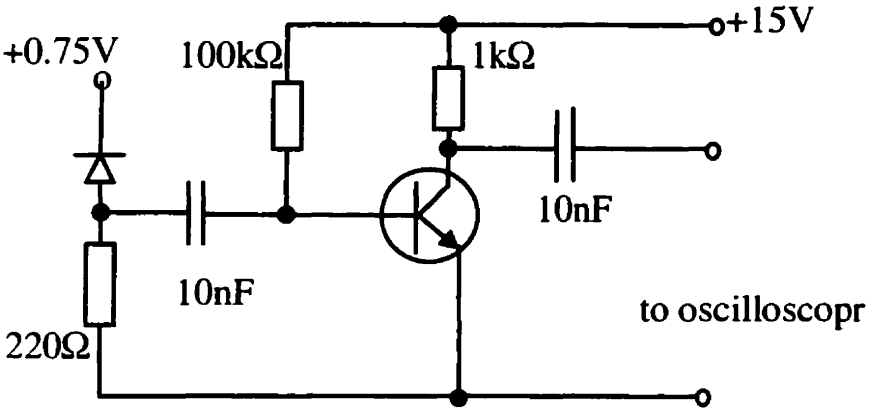

Figure 6.7 Single stage transistor amplifier circuit

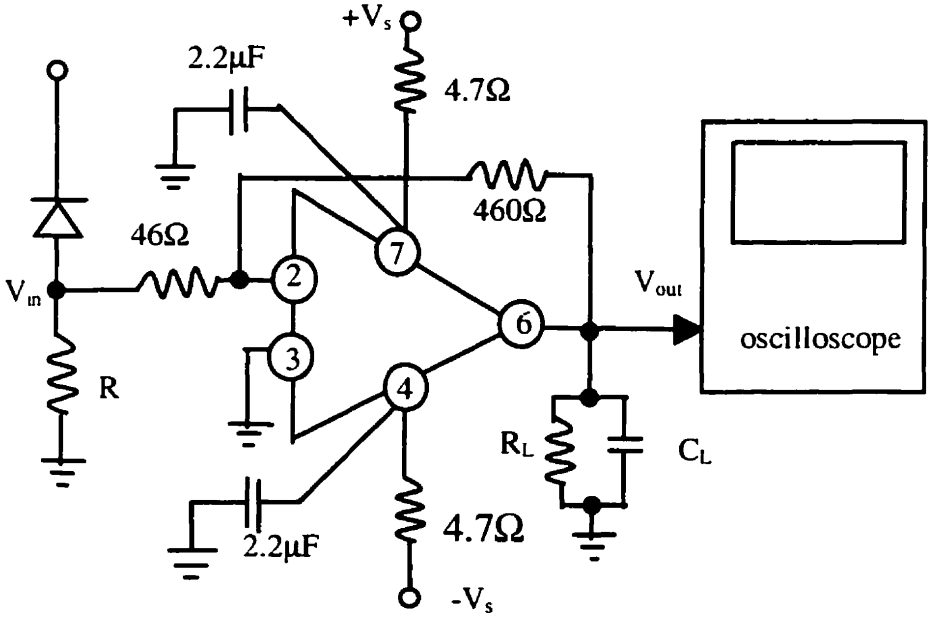

Figure 6.8. Inverting gain of 10 AC AD844 amplifier circuit

Chapter 7

Conclusions

The main objective of this work is to study effects of indium diffusion on monocrystalline samples of $CuInSe_2$. To carry out this study, devices in a homojunction form were employed. The fabrication procedure included polishing surface, evaporation and diffusion indium, bonding conductive wire, and etching the exposed indium. It was found that the surface preparation of $CuInSe_2$ samples is the key to obtaining photodiodes with a high quantum efficiency. Both diffusion time and temperature during the junction formation, treating time and temperature after the junction formation were optimized. It was found that diffusion for a period of time from 4 to 5 minutes at 200°C and post-treating for a period of time of 10 minutes at 100°C gave the best results. The quantum efficiencies of the photodiodes were as high as 60%.

Room temperature current-voltage measurements were carried out after each fabrication step for the photodetectors. The relationship between quantum efficiency, junction depth, surface recombination velocity, and minority carrier diffusion length were analyzed. From the present samples, it is believed that the quantum efficiency of $CuInSe_2$ photodiode can be improved by optimizing the junction depth.

The dark current-voltage characteristics of the $CuInSe_2$ photodiodes were also measured. It was confirmed that the diffusion current and recombination current or surface leakage current are comparable to that due to the dark current transport for the homojunctions in monocrystalline $CuInSe_2$. It was further noted that rinsing with ammonia was not always beneficial to photodiode performance.

In addition, capacitance, voltage and frequency response measurements were performed. It was found that at a given biasing voltage, the capacitance value decreased when the measuring frequency was increased. This result indicated that deep defects exist in the material.

A photocurrent and capacitance method was used to determine the diffusion length of minority carriers. The method is simple and does not require accurate values of

the optical absorption coefficient. The choice of optimum wavelength for the experiments appears to be determined by the band-gap value. In these experiments, monochromatic light source was used. The value of electron diffusion length obtained for the present photodiodes was less than 1 μm. This value can serve as a reference for the future junction depth design for the $CuInSe_2$ photodiodes.

The quantum efficiencies of the photodetectors were also measured. The conditions for fabrication of photodetectors of large quantum efficiency were determined.

Finally using a spark source, the bandwidth of photodetectors was measured and analyzed. It is believed that the frequency response of the $CuInSe_2$ homojunction photodetectors is limited by its carriers diffusion time.

To summarize the thesis, some possible further work is suggested here. Firstly, the preparation of surfaces of $CuInSe_2$ must be improved and an improved bonding methods must be developed. Secondly, impurity concentration in $CuInSe_2$ crystal should be increased further in order to reduce carrier diffusion time and increase photodetector response speed. Finally, an anti-reflection layer should be applied in order to improve the quantum efficiency.

References

[1.1] P. Migliorate, B. Tell, J. L. Shay, and H. M. Kasper. Appl. Physics. Lett. **24**, 227 (1974).

[1.2] S. N. Qiu, W.W. Lam, C. X. Qiu, I. Shih. Applied surface science 113/114 (1997) 764-767.

[1.3] J. Piekoszewski, L. Castaner, j. J. Loferski, J. Beall, and W. Giriat, J. Appl. Phys. 51 (1980) 5375.

[1.4] W. E. Devaney, R. A. Mickelsen, and W. S. Chen, Conf. Record, 18th IEEE Photovoltaic Specialists Conf. (1985) 1733.

[1.5] B. Tell and P. M. bridenbaugh. J. Appl. Phys. 48, 2477 (1977).

[1.6] P. Yu, Y. S. Park, S. P. Faile and J. E. Ehret. Appl. Phys. Lett. 26, 717 (1975).

[1.7] L. Y. Sun, L. L. Kazmerski, A. H. Clark, P. J. Ireland, and D. W. Morton, J. Vac. Sci. Technol. 15, pp265 (1978).

[1.8] H.S. Ullal, K. Zweibel, B. v. Roedern: In Proc. 26th IEEE Photovolt. Spec. Conf. (IEEE, New York 1997) p.301

[1.9] K. W. Mitchell, C. Eberspacher, J. H. Ermer, K. L. Pauls, and D. N. Pier, IEEE Trans. Electron Devices 37, 410 (1990)

[1.10] D. E. Carlson, in The physics of Hydrogeated Amorphous Silicon I, Structure, Preparation, and Devices, edited by J. D. Joannopoulos and J. Lucovsky (Springer, Berlin, 1984), pp. 203-241.

[1.11] J. L. Shay, B. Tell, h. M. Kasper, and L. M. Schiavone, Phys. Rev. B 7, 4485(1973).

[1.12] C. H. Champness. Journal of Materials Science: Materials in Electronics. 10, pp. 605-622 (1999).

[1.13] J. L. Shay, S. Wagner and H. M. Kasper, Appl. Phys. Lett., 27, (1975) 89.

[1.14] S. Wagner, J. L. Shay, P. Migliorato and H. M. Kasper, Appl. Phys. Lett., 25, (1974) 434.

[1.15] S. P. Grindle, A. H. Clark, S. Rezaie-Serej, E. Falconer, J. McNeily and L. L. Kazmerski, *J. Appl. Phys.* **51**, 5464 (1980)

[1.16] J. Hedstrom, H. Ohlsen, M. Bodegrad, A. Kylner, L. Stolt, D. Hariskos, M. Ruckh, and H. Schock, Proc. 23th IEEE Photovoltaic Spec. Conf. 364 (1993)

[1.17] J. R. Tuttle, J. S. Ward, T. A. Berens, M.A. Contreras, K. R. Ramanathan, A. L. Tennant, J. Keane, E. D. Cole, K. Emery, R. Noufi: Mater. Res. Soc. Symp. Proc. 426, 143 (1996).

[1.18] M. A. Contreras, J. Tuttle, A. Gabor, A. Tennant, K. Ramanathan, S. Asher, A. Franz, J. Keane, L. Wang, J. Scofield and R. Noufi, *Proc. 24th IEEE Photovoltaic Spec. Conf. (1994 IEEE 1st World Conf. on Photovoltaic Energy Conv)*, 68 (1994).

[1.19] F. Karg, H. Aulich, W. Riedl: In Proc. 14th Europ. Photovolt. Solar Energy Conf., ed. By H. A. Ossenbrink, P. Helm, H. Ehmann (Stenphens, Bedford 1977) p. 2012.

[1.20] B. Dimmler, E. Gross, D. Hariskos, F. Kessler, E. Lotter, M. Powalla, J. Springer, U. Stein, G. Voorwinden, M. Gaeng, S. Schleicher: In Proc. 2nd World Conf. on Photovolt. Energy Conv., ed. By J. Schmid, H. A. Ossenbrink, P. Helm, H. Ehmann, E. D. Dunlop (E. C. Joint Res. Centre, luxembourg 1998) p. 419.

[1.21] M. Yamaguchi: J. Appl. Phys. 78, 1476 (1995)

[1.22] H. W. Schock, K. Bogus: In Proc. 2nd World Conf. On Photovolt. Energy Conv., ed. By J. Schmid, H. A. Ossenbrink, P. Helm, H. Ehmann, E. D. Dunlop (E. C. Joint Res. Centre, Luxembourg 1998) p. 3586

[1.23] P. W. Yu, S. P. Faile and Y. S. Park, *Appl. Phys. Lett.* **26**, 384 (1975).

[1.24] P. W. Yu, Y. S. Park, S. P. Faile and J. E. Ehret, *Appl. Phys. Lett.* **26**, 717 (1975).

[1.25] B. Tell and M. Bridenbaugh, *J. Appl. Phys.* **48**, 2477 (1977).

[1.26] J. L. Shay and J. H. Wernick, Ternary chalcopyrite semiconductors: growth, electronic properties and applications, Pergamon Press, New York 1975.

[1.27] S. M. Sze, Physics of semiconductor devices, 2nd ed., J. Wiley, New York 1981.

[1.28] T. J. Coutts and J. D. Meakin (Ed.), Current Topic in Photovoltaic, Academic Press, London 1985 (Chap. 2)

[1.29] J. Gonzalez, C. Rincon, A. Redondo, and P. Negrete, Jpn. J. App. Phys. **19,** 29 (1980).

[2.1] J. R. Meyer-Arendt, Introduction to Classical and Modern Optics. Prentice-Hall, Inc. New Jersey (1995)

[2.2] T. S. Moss, G. J. Burell, and B. Ellis, Semiconductor Opto-Electronics, Butterworths and Co. Ltd., London. 1973.

[2.3] A. M. Hermann, L. Fabick, K. Zweibel, and R. Hardy, Proc. 16th IEEE Photovoltaic Spec. Conf., 840 (1982)

[2.4] E. L. Dereniak and G. D. Boreman, Infrared Detectors and Systems. John Wiley & Sons, Inc. (1996)

[2.5] H. J. Hovel, Semiconductors and Semimetals Vol.11, Academic Press, New York, 1975.

[2.6] L. K. Anderson and B. J. McMurtry, Proceedings of the IEEE, 54, 1335, (1966)

[2.7] H. Levinstein, Phys. Today, November, 23 (1977).

[2.8] G. Lucovsky and R. B. Emmons, Appl. Opt. 4, 697 (1965).

[2.9] K. M. Johnson, Microwave J. July, 71 (1963).

[2.10] R. P. Riesz, Rev. Sci. Inst. 33, 994 (1962).

[2.11] L. S. Yip and I. Shih, Proc. 24th IEEE Photovoltaic Specialists Conf. (First world Conf. on Photovoltaic Energy Conversion), 210 (1994).

[2.12] L. S. Yip, Development of high efficiency solar cells on $CuInSe_2$ single crystals, Ph. D. thesis, McGill University (1996).

[2.13] W. W. M. Lam, investigation of photovoltaic cells on Bridgman grown $CuGa_xIn_{1-x}Se_2$ crystals, Ph. D. thesis, McGill University (1998).

[2.14] C. X. Qiu, Characteristics of ZnO/$CuInSe_2$ heterojunctions and $CuInSe_2$ Homojunctions, Master thesis, McGill University (1985).

[3.1] S. M. Sze, Physics of Semiconductor Devices, 2nd Edition, John Wiley & Sons (New York), 1981.

[3.2] A. S. Grove, Physics and Technology of Semiconductor Devices, John Wiley & Sons, New York, 1967.

[3.3] S. R. Forrest, R. F. Leheny, R. Nahory, and M. A. Pollack, Appl. Phys. Lett., 37, 322, (1980).

[3.4] D. S. Chan and J. C. H. Phang, IEEE Trans. Electron Dev. ED-31, 381 (1984).

[4.1] S. M. Sze, Physics of Semiconductor Devices, 2nd Edition, John Wiley & Sons (New York), 1981.

[4.2] C. T. Sah and V. G. K. Reddi, IEEE Trans. Electron Dev., ED-11, 345 (1964).

[5.1] V. A. Tyagai. Soviet Phys. Solid State, 6, 1260 (1964).

[5.2] K. L. Smith and M. Abbot, Solid State Electron. 15, 361 (1972).

[5.3] M. L. Young and M. C. Rowland. Phys. Status Solidi A, 16, 603 (1973).

[5.4] S. N. Qiu, C. X. Qiu, and I. Shih, Applied Surface Science, 92, 306, (1996).

[5.5] J. Dorantes-Davila, A. Lastras-Martinez, and P. M. Rachah, App. Phys. Lett. 38, 442 (1981).

[5.6] Z. A. Shukri and C. H. Champness, NREL/SNL Photovoltaics Program Review (AIP Press, New York, 1997) p.603.

[5.7] A. A. Al-Quraini and C. H. Champness, Proc. 26th IEEE Photovoltaic Specialists Conf. 415 (1997).

[6.1] R. J. Hoss, Fiber Optic Communications Design Handbook, Prentice Hall, 1990.

[6.2] J. C. Palais, Fiber Optic Communications, Prentice Hall, 1988.

[6.3] Y. Chen, S. Williamson, and T. Brock, Appl. Phys. Lett., 59, 1985 (1991).

[6.4] C. A. Burrus, J. E. Bowers, R. S. Tucker, Electron. Lett. 21, 262 (1985).

[6.5] A. Chappell, Optoelectronics Theory and Practice, McGraw-Hill Book Company, 1978